ABSTRACT

Title of Dissertation:	ADDITIVE MANUFACTURING FOR RECAPITULATING BIOLOGY IN VITRO AND ESTABLISHING CELLULAR & MOLECULAR COMMUNICATION
	Chen-Yu Chen
	Doctor of Philosophy in Bioengineering, 2023
Dissertation directed by:	Dr. William E. Bentley
	Robert E. Fischell Distinguished Professor of Engineering, founding Director of the Fischell Institute for Biomedical Devices, and Director of the Maryland Technology Enterprise Institute, Fischell Department of Bioengineering

Recapitulating biological systems within laboratory devices, particularly those with analytical instrumentation, has enhanced our ability to understand biology. Especially useful are systems that provide data at the length and time scales characteristic of the assembled biological systems. In this dissertation, we have employed two advanced technologies — additive manufacturing and electrobiofabrication to create systems that both recapitulate biology and provide ready access to molecular data.

First, we utilized two-photon direct laser writing (DLW) and digital light processing (DLP) 3D printing to reconstruct morphologies of human gut villi. Our constructs enable small molecule

diffusion through pores and enable epithelial cell growth and differentiation, as in the gastrointestinal (GI) tract. We also developed a cell/particle alignment methodology that applies a vacuum on the underside of a device to rapidly facilitate attachment to 3D printed scaffolds. These simple demonstrations of additive manufacturing show how one can better tailor geometric features of organ-on-a-chip and other in vitro models.

We then added electrobiofabrication as a means create functionalized surfaces that rapidly assemble biological components, noted for their labile nature, onto devices with just an applied voltage. In one example, we show how a thiolated polyethylene glycol (PEG) can be electroassembled as a sensor interface that includes antibody binding proteins for both titer and glycan analysis. Rapid assessment of titer and glycan structure is important for biopharmaceuticals development and manufacture. While the interface and sensing methodology was performed using standard laboratory instrumentation, we show that the methodology can be streamlined and operated in parallel by incorporating into a microfluidic sensor platform. Additionally, we show how the combination of optical and electrochemical (redox) based measurements can be combined in a simplified insert that "fits" nearly any microplate reader or other fairly standardized laboratory spectrophotometric unit. We believe that by adapting transformative electrochemical analytical methods so they can augment more traditional optical techniques, we might ultimately generate devices that provide a far more comprehensive picture of the target, promoting better investigation. Specifically, we show how three important biological and chemical systems can be interrogated using both optical measurements and electrochemistry: the oxidation state of proteins including monoclonal antibodies, redox status of hydrogel materials, and electrobiofabrication and electrogenetic induction.

Lastly, we demonstrate how electrobiofabrication can be used to create designer communities of bacteria — artificial biofilms — the study of which is important for understanding phenomena from infectious disease to food contamination. That is, we discovered that by varying the applied voltage, surface area, and composition of the to-be-assembled hydrogel solution, we can precisely control the intercellular environment among bacterial populations.

In sum, this dissertation integrates advances in assembly, through additive manufacturing, electrobiofabrication, with advances in electrochemical analysis to bring to the fore an electronic understanding of complex biological phenomena. We believe that the capability of translating biological information into a processible digital language opens tremendous opportunities for advancing our understanding of nature's amazing systems, potentially enabling electronic means to control her subsystems.

ADDITIVE MANUFACTURING FOR RECAPITULATING BIOLOGY IN VITRO AND ESTABLISHING CELLULAR & MOLECULAR COMMUNICATION

by

Chen-Yu Chen

Dissertation submitted to the Faculty of the Graduate School of the
University of Maryland, College Park, in partial fulfillment
of the requirements for the degree of
Doctor of Philosophy
2023

Advisory Committee:
Dr. William E. Bentley, Chair
Dr. Michael L. Shuler
Dr. Gregory F. Payne
Dr. Gregg Duncan
Dr. Ryan D. Sochol, Dean's Representative

Dedication

This dissertation is dedicated to my parents and my beloved family

for their endless love and support.

Cattleya labiata is an orchid species, discovered in Brazil in 1818.

In memory of my grandfather Tân, Tsìn-Kuì who cultivated hundreds of orchids in his garden.

The illustration was created by Henry Frederick Conrad Sander, an orchidologist and nurseryman (1847-1920)

Acknowledgements

First and foremost, I would like to express my sincere appreciation to my advisor Dr. William Bentley who always tries to offer his best to the students. During my Ph.D. studies, I genuinely experienced his inclusiveness and consideration for his students and their interests. I am very grateful that I had such an advisor who offered all the freedom and resources that I could grow and explore all the opportunities to my heart's content. His patience, coupled with his clever encouragement, was a privilege beyond anything I could have hoped for.

I would like to thank my committee members – To Dr. Ryan Sochol, thank you for providing precious support and knowledge for my 3D printing research. Without you, I wouldn't be able to explore the most advanced manufacturing. To Dr. Gregg Duncan, thank you for always being so kind and offering useful advice. It was a wonderful experience to be your biofluidic TA. To Dr. Gregory Payne, thank you so much for always being that energetic and enthusiastic and promoting the partnership between our labs. I always had a lot of fun at your parties. To Dr. Michael Shuler, I felt honored and lucky to be part of your research group in Cornell. Your insight and warm support have deeply influenced my life.

To Dr. Eunkyoung Kim – Thank you for always being so kind and helpful. Your prompt and generous support has significantly facilitated my research and truly helped me overcome the difficulties during my frustrating period.

To Dr. Eric VanArsdale – You were the first person who approached me when I joined the lab. Thank you for being my cherished friend, an attentive listener, and people who teased out my crazy ideas for the past 5 years. Without you, life wouldn't be that much fun and joyful.

To Dr. Sally Wang –You dedicated yourself to challenging yet impactful research, and I am proud to have been able to offer my humble contribution to assist you with it. It was a very joyful time that I enjoyed a lot during my Ph.D. Thank you.

To Dr. Dana Motabor – Thank you for trusting me and letting me join your AMBIC and NIIMBL projects. I really enjoyed the time we spent improving the system. I am very thankful that the effort we made together has deeply facilitated my research.

Next, I want to say thank you so much to my many lab mates and colleagues – Dr. Chen-Yu Tsao, Dr. David Quan, Dr. Wu Shang, Dr. Narendrenath Bhokisham, Dr. Kristina Stephens, Dr. So Hyun Ahn, Rahma Zakira, Kayla Chun, Monica Chu, Futoon Aljirafi, Nick Pirolli, Ben Wu, Briahnna Streeter, An Bowman, Dr. David Hörmstrum, Dr. Zhiling Zhao, Dr. Si Wu, Rita Argenziano, Dr. Yi Liu, Dr. Andrew Lamont, Dr. Abdullah Alsharhan, Michael Restaino, Pannie Xu, Jack Wen, Olivia Young, Adira Colton, Dr. John Rzasa, Kevin Aroom, and Quinn Burke. Without all your advice, encouragement, and understanding, I wouldn't have been able to create that many interesting designs and had fun during my Ph.D. It was such a privilege for me to work with you. The good memories and laughter I had with you are the most valuable gift I will always cherish.

Lastly, I would like to express my deepest gratitude to my parents and family for their endless care and love. Your kindness, integrity, and hardworking have profoundly influenced me and I wish to carry this spirit and continue my life adventure. I also want to acknowledge all the happiness, sorrow, frustration, struggle, routine, craziness, and enthusiasm during this journey. The beauty and misery that sublimated in those adventures eventually made me who I am today. I am very glad that I didn't give up during this journey and also will not in the future.

My Life's Motto Poem

雨ニモマケズ　　宮澤賢治

雨ニモマケズ
風ニモマケズ
雪ニモ夏ノ暑サニモマケヌ
丈夫ナカラダヲモチ

慾ハナク
決シテ瞋ラズ
イツモシヅカニワラッテヰル
一日ニ玄米四合ト
味噌ト少シノ野菜ヲタベ

アラユルコトヲ
ジブンヲカンジョウニ入レズニ
ヨクミキキシワカリ
ソシテワスレズ

野原ノ松ノ林ノ蔭ノ
小サナ萱ブキノ小屋ニヰテ

東ニ病気ノコドモアレバ
行ッテ看病シテヤリ

西ニツカレタ母アレバ
行ッテソノ稲ノ束ヲ負ヒ

南ニ死ニサウナ人アレバ
行ッテコハガラナクテモイヽトイヒ

北ニケンクヮヤソショウガアレバ
ツマラナイカラヤメロトイヒ

ヒデリノトキハナミダヲナガシ
サムサノナツハオロオロアルキ

ミンナニデクノボ一トヨバレ
ホメラレモセズ
クニモサレズ

サウイフモノニ
ワタシハナリタイ

不畏風雨　　宮澤賢治

不輸給雨
不輸給風
不畏雪天酷寒及夏日炎熱
保持健康的體魄

別無所求
絕不動怒
永保恬靜的微笑
一日吃四合的糙米
一點味噌和青菜

不論遇到什麼事
凡事保持客觀
仔細去觀察，聆聽，理解
然後銘記在心

在原野松林的樹蔭中
有我棲身的小小茅草屋

東邊若有生病的孩子
就去照顧他

西邊若有疲憊的母親
就去幫她扛稻穗

南邊若有將死之人
就去安慰他不用害怕

北邊若有爭吵、興訟
就去告訴他們別做這種蠢事

遭遇乾旱時，為世人傷心流淚
遭遇冷夏時，為世人著急奔波

大家都說我是個傻子
不需別人的稱頌表揚
也無需他人為我擔憂

這就是
我希望成為的人

Ame ni mo makezu (Be not Defeated by the Rain)
Kenji Miyazawa

Unbeaten by the rain
Unbeaten by the wind
Bested by neither snow nor summer heat
Strong of body

Free of desire
Never angry
Always smiling quietly
Dining daily on four cups of brown rice
Some miso and a few vegetables

Observing all things with dispassion
But remembering well

In the meadow beneath a canopy of pines,
living in a small, thatched-roof house

Going east to nurse the sick child

Going west to bear sheaves of rice for the weary mother

Going south to tell the dying man there is no cause for fear

Going north to tell those who fight to put aside their trifles

Shedding tears in time of drought
Wandering at a loss during the cold summer

Called useless by all
Neither praised
Nor a bother

Such is the person
I wish to be

Table of Contents

List of Tables

List of Figures

List of Schemes

List of Abbreviations

CV: Cyclic Voltammetry

Cys: Cysteine

DTT: Dithiothreitol

DLP: Digital light processing

DLW: Direct laser writing

E. coli: Escherichia coli

EIS: Electrochemical Impedance Spectroscopy

Fc: 1,1'-Ferrocenedimethanol

FITC: Fluorescein isothiocyanate

GFP: Green fluorescent protein

HRP: Horseradish peroxidase

IgG: Immunoglobulin G

ITO: Indium tin oxide electrode

PEG-SH: Thiolated Poly(ethylene glycol)

Chapter 1 Introduction

1.1 Aim and scope of dissertation

The aim of this dissertation is to exploit the capability of additive manufacturing to create functional interfaces at multiple length scales and provide meaningful multidirectional communications via digital-molecular-biological trajectories. This research focuses on the development of three interfaces: (i) three dimensional (3D) scaffolds that mimic human villi geometrical features and biofluidic functions to support mammalian cell attachment and proliferation, (ii) multi-functional interfaces providing simultaneous electrochemical and optical access, (iii) artificial biofilm model development via electrobiofabrication of engineered cells.

In Chapter 2, we demonstrate the reconstruction of three-dimensional (3D) geometries and functions of human villi by combining two 3D printing techniques: Digital Light Processing (DLP) and two-photon direct laser writing (DLW). These techniques employ resin-based supporting materials to achieve the desired structures. Additionally, we will introduce a novel method for rapid cell aligning towards the vertical surface on 3D porous scaffolds which can potentially become a practical solution for tissue engineering. In Chapter 3, we will use DLP printers to fabricate custom microfluidic devices to provide precise fluidic control for rapid protein analysis. Meanwhile, we will show how 3D printed microfluidic devices can be quickly functionalized via the combination with an electrochemical interface which realizes the bidirectional chemical reaction actuation and molecular information digitalization.

Specifically, we will show how to use this system to electrofabricate a PEG-based sensor interface that enables the detection of antibody galactosylation and titer. In Chapter 4, we will focus on the exploration of the information integration capability enabled by the joint interface from 3D printing and electrochemistry. Here, three individual but burgeoning applications (reduce protein interrogation, electrofluorochromic material characterization, and cellular electrogenetic induction) within the field of electrochemistry will be demonstrated to highlight the ability of this interface to provide digitized optical and electrochemical details. Furthermore, we demonstrate how the modular design and customizability stemming from additive manufacturing can benefit *in situ* and *operando* information acquisition and integration by granting access to existing analytical techniques. Lastly, in Chapter 5, we present the generation of a functional interface based on engineered bacterial cells through the digital-optical-electrochemical interface. We employ electrodeposition to fabricate a PEG-based artificial biofilm containing functional cells. Analogous to additive manufacturing, we first demonstrate that the electrofabrication of artificial biofilms can be precisely controlled through practical factors such as potential, charge, and mediator contents in a layer-by-layer fashion. Representative figures or images to demonstrate the conclusion or results in this dissertation are illustrated in **Figure 1.1**.

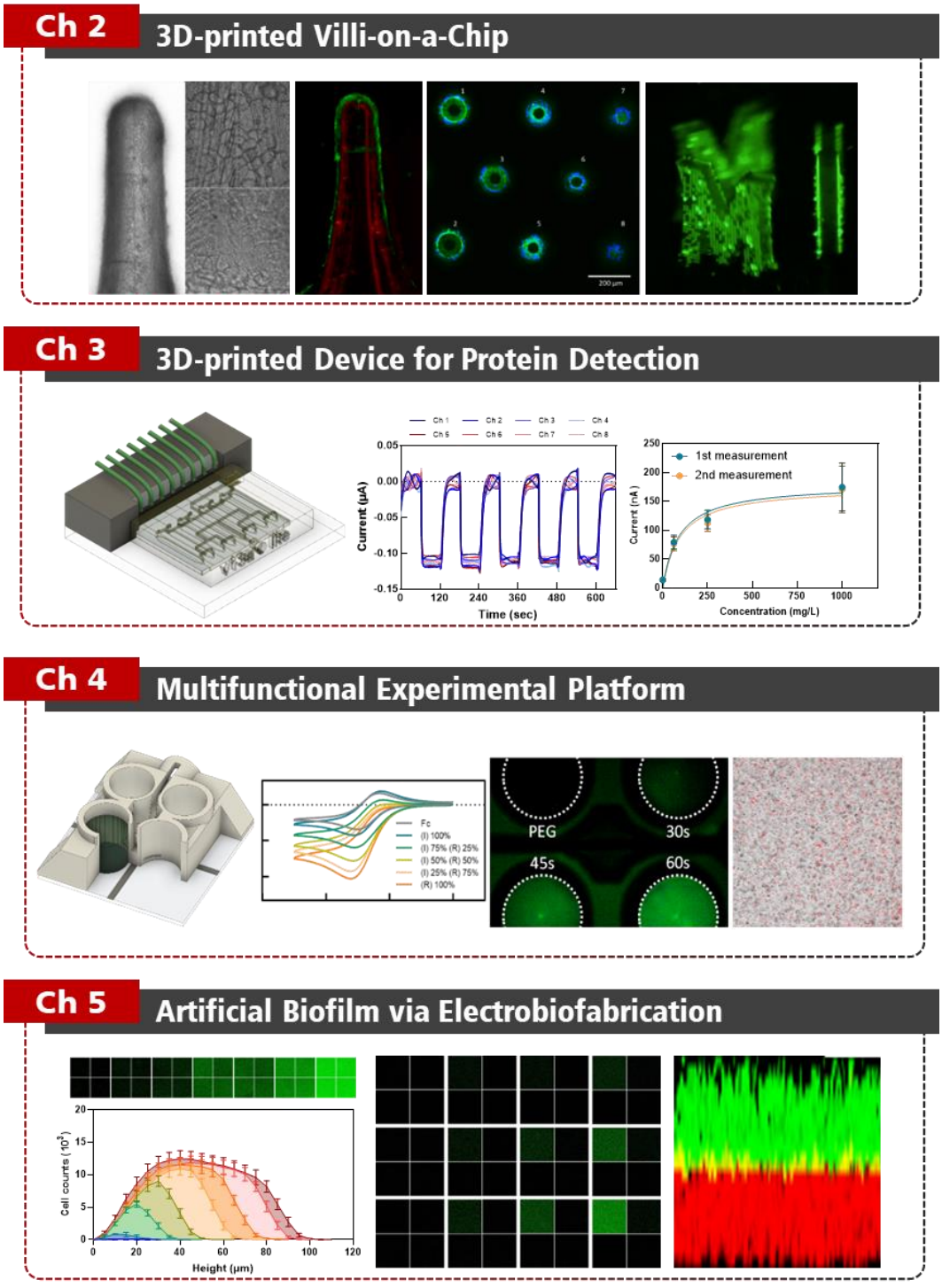

Figure 1.1 Representative materials discussed, and images generated in this dissertation. (Figures and images are adapted from the figures in Chapter 2 to 5. Details and discussion will be provided in the following chapters.)

1.2 Additive manufacturing (3D printing)

First described by Hideo Kodama of Nagoya Municipal Industrial Research Institute in 1981[1], additive manufacturing, also widely recognized as three-dimensional (3D) printing, has been revolutionizing the world of manufacturing and design due to its unique nature of creating 3D objects via laying down desired deposits of materials using point-by-point and/or layer-by-layer processes. With roots in the aerospace[2], automotive[3], and construction industries[4], this technology allows for the creation of complex and intricate objects by layering materials, such as polymers, metal, and cement-based mixtures. Nowadays, 3D printing has expanded its applications to an extensive array of biomedical-related fields, including food science[5], medicine[6], and tissue engineering[7–9], utilizing ceramics, biocompatible polymers, hydrogels, and even cells.

At present, three main approaches dominate the field of biomedical applications: (1) extrusion-based 3D printing (fused deposition modelling and direct ink writing), (2) stereolithography, and (3) multijet (or polyjet) modelling.[10] Here, we will primarily introduce the extrusion-based 3D printing and stereolithography.

Drawing inspiration from the extrusion of thermoplastic materials using a hot glue gun, extrusion-based 3D printing technology was initially patented as "fused deposition modeling (FDM)" and quickly became the most prevalent additive manufacturing method across academic, industrial, and commercial sectors[11]. In this process, 3D objects are fabricated by sequentially dispensing thermoplastic materials from a heated nozzle onto a substrate through a point-to-point, layer-by-layer approach. A later

variant of this fabrication strategy, known as "direct ink writing (DIW)," replaced thermoplastic materials with "inks" and primarily utilized pressurized chambers or syringes for the feeding mechanism (**Figure 1.2**). Bypassing the need for thermal processing steps (i.e., heating or cooling), DIW has demonstrated its potential for fabricating both miniature organ-on-a-chip systems[12] and 1:1 scale (actual size) biomedical scaffolds for cell distribution[13,14].

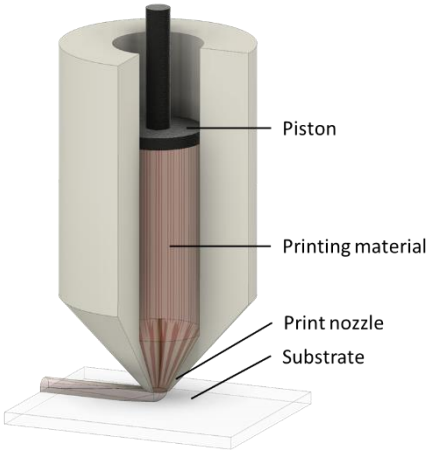

Figure 1.2 Direct ink writing (DIW) 3D printing

Stereolithography was first introduced by Hideo Kodama in 1981, demonstrating the creation of 3D objects through the stacking of crosslinked monomers using a controlled dose of ultraviolet (UV) light on liquid-phase photo-hardening materials. In 1984, the development of the "stereolithography apparatus (SLA)" significantly enhanced this method by employing a focused light to selectively solidify photo-sensitive material in desired locations. Specifically, the process begins with the preparation of a liquid-phase photoreactive material (e.g., resin, photoresist) in a bath. A focused light source, typically a laser, then photocrosslinks (i.e., photocures) the material at designated

locations in a point-by-point, layer-by-layer manner. By successively connecting the cured patterns, SLA 3D printing can create the desired product according to a digital 3D model generated using computer-aided design (CAD) tools. This point-to-point fabrication method has considerably expanded the usability of this technology, as users can precisely describe objects through combinations of coordinates in a 3D reference system. Meanwhile, digital light processing (DLP) 3D printing technology has emerged as a promising additive manufacturing method due to its rapid printing capabilities and exceptional scalability[15]. Unlike the point-to-point-based approach of creating rounded lines to form the final structure, DLP employs a digital micromirror device (DMD) to project layers of square-shaped voxels, constructing an entire layer simultaneously[16]. Although rapid fabrication is its most significant advantage, the resolution of DLP is constrained by the minimum pixel size of the projector screen. The resolution (size of the smallest solidifying unit) of SLA primarily depends on the minimal laser spot size, while that of DLP is determined by the minimum pixel size on the DMD.

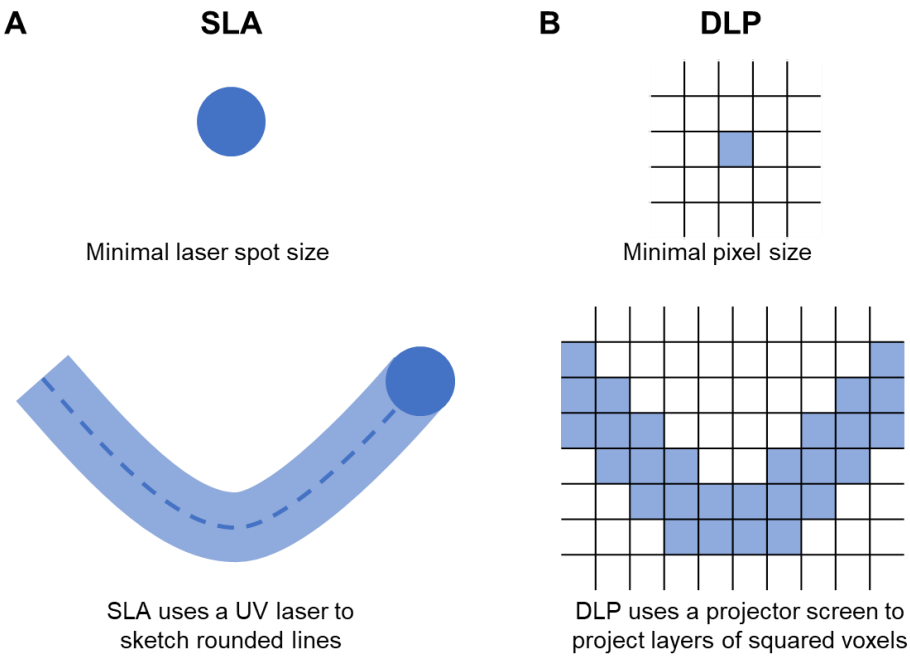

Figure 1.3 Stereolithography apparatus (SLA) and digital light processing (DLP) (A) SLA solidifies monomers based on the laser spot and sketch rounded lines. (B) DLP uses digital micromirror device to simultaneously construct an entire layer.

As illustrated in **Figure 1.3**, in SLA, the laser spot is controlled by a pair of XY motors, enabling smooth and continuous sketches. Conversely, DLP relies on the digital micromirror to reflect a comprehensive pattern onto an entire plane of resin, ultimately printing objects. This approach, however, limits the smoothness of products fabricated using DLP-based printers. In comparison with the continuous writing of SLA, aliasing in DLP results in jagged edges on the prints.

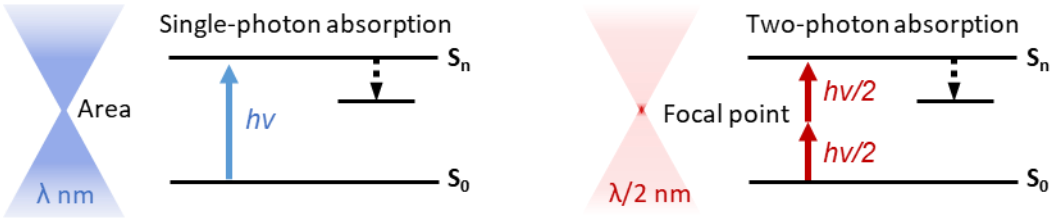

Figure 1.4 Single-photon absorption and two-photon absorption
Single-photon absorption excites all molecules on the light pathway, while two-photon absorption only excites molecules at the focal point.

When narrowing down to the micro/nanoscale 3D printing methodologies, a later elaboration of SLA known as "Direct Laser Writing (DLW)" utilizes two-photon absorption (TPA) phenomena to accurately initiate the photopolymerization at a single spot in a 3D reference system[17]. TPA can be described as the process where one molecule simultaneously absorbs two photons of identical or different energy levels which triggers the excitement from a lower energy state to a higher one. The energies from the two photons combined are equal to the energy difference between two states (**Figure 1.4**). This molecular excitation will further initiate the polymerization between the neighboring monomers. This approach has notably improved resolution to the sub-100 nm level, enabling precise spatial control for the fabrication of microscale 3D objects[18]. Prior research has demonstrated that DLW can be employed to create microscale and even nanoscale features for applications in diverse fields, including microfluidics, biomedical implants, and 3D scaffolding for tissue engineering.

In this study, we primarily employ two resin-based 3D printers, the Nanoscribe Photonic Professional GT2 and the CADWorks3D MiiCraft Ultra 50, which utilize two

principal variants of stereolithography: DLW and DLP, respectively. The technical specifications of the two 3D printers are listed in **Table 1.1** and **Table 1.2**.

Table 1.1 Photonic Professional GT2 specifications[19]

Printing technology	Layer-by-layer Two-Photon Polymerization
Minimum XY feature size	160 nm typical; 200 nm specified*
Finest XY resolution	400 nm typical; 500 nm specified*
Finest vertical resolution	1,000 nm typical; 1,500 nm specified*
Layer distance	variable, 0.1 – 5.0 µm*
Maximum object height	8 mm*
Build volume	100 × 100 × 8 mm^3 *
Minimum surface roughness R_a	≤ 20 nm*
Max. scan speed	from 100 to 625 mm/s*

* Values may vary depending on the Solution Set, objective or photoresin in use

Table 1.2 CADWorks3D MiiCraft Ultra 50 specifications[20]

Projector	1080 × 1920 HD
Native pixels	2 million unique pixels
Build area	57 × 32 × 120 mm^3
XY resolution	30 µm
Z-Layer resolution	5 µm to 500 µm
Wavelength (LED)	365/385/405 nm

1.3 Organ-on-a-chip

Widely acknowledged as the founder of Organ-on-a-Chip industry, Dr. Michael Shuler, a renowned bioengineer at Cornell University, first coined the term “Animal-on-a-Chip” which later evolved into "Body-on-a-Chip" back in 1990. According to Dr.

Shuler, “I will define an ‘Organ-on-a-Chip’ as a physical microscale model (typically an order of 10^{-6} to 10^{-4} of actual size) of a particular human organ.”[21]

The first Body-on-a-Chip model, comprising gut, liver, and fat cells, was integrated onto a silicon wafer substrate featuring etched minute compartments connected by microfluidic channels. At the time, Dr. Shuler identified this innovative experimental system as a “microscale cell culture analog (μCCA)” [22,23]. By mimicking blood distribution between multiple cell types representing different organs, μCCA for PK-based drug toxicity testing demonstrated its potential to capture meaningful physiological information as well as mathematical models[24]. In the late 2000s, advanced models focused on mimicking the functions of a single human organ, such as the lung-on-a-chip, liver-on-a-chip, and gut-on-a-chip, were capable of recapitulating essential features of human organ functions. The lung-on-a-chip, developed by Donald Ingber's research team at the Wyss Institute for Biologically Inspired Engineering at Harvard University, was one of the earliest and most successful organ-on-a-chip models. The reported microfluidic lung-on-a-chip model was demonstrated to recreate the essential features of a human lung, including alveolar-capillary interface and mechanical forces that mimic breathing[25].

The field truly gained momentum when the academia, pharmaceutical industry, and the government realized that the current preclinical models such as animal trials and cell-based assays are not effective in the drug screening process. Discouragingly, less than 10% of animal trials were truly predictive of human response during the preclinical studies for drug development, resulting an overall low successful rate of drug

candidates selected for human clinical trials.[21] To lower the cost of drug development and improve successful rate in human clinical trials, the National Institutes of Health (NIH) in the United States, for example, launched the Tissue Chip for Drug Screening program in 2012 to support the development and validation of human organ-on-a-chip models.

Advanced manufacturing techniques derived from the micro-electromechanical systems (MEMS) field have significantly impacted the fabrication of organ-on-a-chip models. By employing multiple building materials, such as cured photoresists, polymer-based filters, and polydimethylsiloxane (PDMS) gaskets or housings, small compartments can be created for cell proliferation. These models provide a straightforward approach to studying selective and regulated molecular interactions within microscale organs. However, due to the nature of this construction methodology, the two-dimensional plane restricts the potential for cell development in three-dimensional space. Consequently, this limitation may introduce bias to some extent, as cell morphologies can differ depending on the environment.

To provide more options for creating these surrogate systems, in Chapter 2 of this research, we will demonstrate how additive manufacturing can facilitate the reconstruction of human gut 3D geometries in a villi-on-a-chip model and enables the molecular transport within and on printed scaffolds.

1.4 Electrobiofabrication and mediated electrochemical probing

Biofabrication is a rapidly evolving field that utilizes advanced manufacturing processes to recapitulate complex contexts in biology using living cells, biomolecules,

or biomaterials. Tissue engineering, and the previously mentioned 3D bioprinting and organ-on-chip are typical examples of biofabrication. Electrobiofabrication is an electrically based biofabrication methodology. That is, by employing electrical signals, it has the ability to controllably manipulate the assembly and functionalization of macromolecules (e.g., chitosan[26–31], alginate[32], collagen[33], silk[34], and polyethylene glycol[35–37]). As a result, leveled material structures can be generated. Mediated electrobiofabrication, meanwhile, specifically means those electrically based biofabrication methods facilitated or promoted by redox mediators[30,31,36,38,39].

As previously demonstrated in the articles[35–37,40], polyethylene glycol (PEG) is a material widely used to serve as the cell supporting structure or function interfaces. To form the crosslinked network via mediated electroassembly, the thiolated PEG monomers has to be added into a solution containing redox mediators. By applying an electrochemically oxidative potential to the solution, the redox mediator serves a shuttle that gets oxidized at the electrode and then carries this oxidative power to the thiolated PEG monomers triggering polymerization (**Figure 1.5**). Several mediators have been reported for effective PEG electrobiofabrication such as pyocyanin (PYO)[40], catechol (CAT)[35,40], 1,1'-ferrocenedimethanol (Fc)[36], potassium hexachloroiridate (Ir)[36], and acetosyringone (AS)[35,36]. The functionalization of mediated crosslinked PEG structure was reported. For example, Li et. al. used thiolated PEG (coupled with thiolated polysaccharide hyaluronic acid) as a mimic of the cysteine-rich mucin protein and entrapped MDA-MB-231 breast adenocarcinoma cells[36]. The high cell viability verified the exceptional biocompatibility of this material.

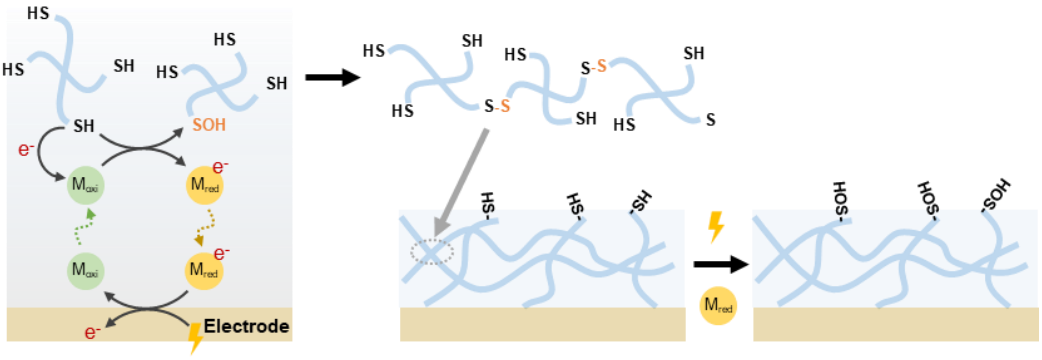

Figure 1.5 Mediated crosslinking process of thiolated PEG

As a sensitive analytical strategy, mediated electrochemical probing employs an adjustable, electrode-generated signal to investigate local environments for redox-based information. Here, mediators serve as messengers that facilitate electron transfer between target molecules and the electrode, leading to current amplification in the electrochemical detection process[41]. That is, biological information can be coded through switching redox mediators' redox state and this electronic format that can later be decoded using advanced information processing methods. Combining mediated electrobiofabrication and electrochemical probing, Motabar et. al. utilized Fc and thiolated PEG to electroassemble sensor interfaces for rapid interrogation of antibody titer and glycosylation[42]. First, the Fc facilitated oxidation process was not only used for PEG polymerization (interface construction) but also initiated the conjugation of recognition elements such as cysteinylated protein G and thiolated Galβ-RCA120 to PEG network (functionalization). Furthermore, Fc serves as a messenger harvesting electrons from the chemical reaction between hydrogen peroxide and reporter HRP (coding), and then delivers this electrical signal back to the hub (decoding).

In this dissertation, we will primarily employ Fc and thiolated PEG to demonstrate the electrochemical assessments that can be used to promote the digitization of biological information.

Chapter 2

High-resolution 3D printed Human Villi-on-a-Chip with Capillary to Enable Transepithelial Molecular Communications

2.1 Introduction

The small intestine, one of the most intricate organs in the gastrointestinal system, functions as a dynamic nexus for food breakdown, nutrient absorption, signaling molecule synthesis, and interkingdom communication. It interacts with various physiological systems, including the cardiovascular, lymphatic, peripheral, and central nervous systems [43]. Its complex functions arise from spatiotemporally diverse microenvironments that host and are regulated by thousands of microbial species. Circular folds, intestinal villi, and microvilli (**Scheme 2.1A**) extend from the epithelial lining, significantly enhancing the surface area and absorption/transport efficiency. These structures allow for substantial fluctuations in molecular signaling molecule concentrations and biophysical indicators, such as pH and oxygen tension, facilitating distributed cell functions, longitudinal cell differentiation from villus crypts to the tip, and spatially localized transport.

In recent years, synthetic *in vitro* models such as organ-on-a-chip (OoC) have gained prominence for their ability to accurately control target microenvironments and mimic human organs[44,45]. With the emerging capacity to engineer gut microbiota [46–50], there is a tremendous opportunity to develop a molecular-scale understanding of

gastrointestinal signaling using human small intestine in vitro models. Over the past decade, numerous *in vitro* models have been designed to elucidate gut epithelium formation, molecular transport, and cellular responses to specific environmental stimuli. For instance, 2D models like the widely used filter-based inserts facilitate epithelial monolayer reconstruction and offer a straightforward approach to study selective and regulated molecular flux from apical to basolateral surfaces. Benefiting from its elasticity, polydimethylsiloxane (PDMS)-based models have enabled research into cell behavior under physical stretching. Additionally, 2D microfluidic models have shown that shear stress can impact cell differentiation.

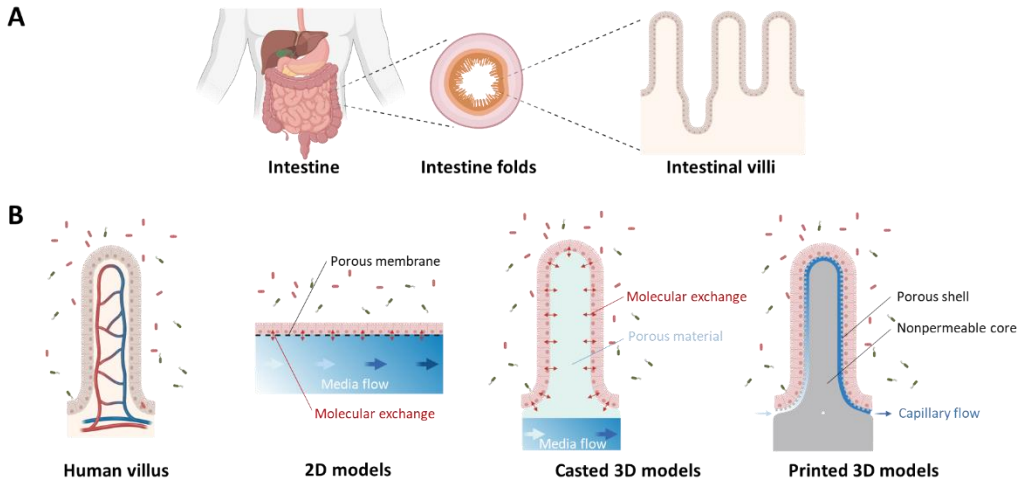

Scheme 2.1 Human intestine and *in vitro* models.

Conventional 2D models have advanced our understanding of how cell adherence, mechanical stimulation, signal delivery, and biomolecules can influence cell behavior[51,52]. However, these models fall short in capturing the biological context in the vertical direction or as a function of villus height, as the microenvironment transitions from an oxidizing to reducing environment where predominant microbial

populations may in fact shift based on flow, oxygenation, or other molecular signaling events[53,54]. *In vitro* models that rely on cell self-assembly struggle to fully reconstruct critical features of intestinal villi, such as their 3D protruding structures and their intrinsic and embedded transport systems.

In the human gut, physical stimulations at the villus tip region differ from those in the crypt. Parameters such as pH[55], oxygen tension[56], and redox environment[57] vary considerably from the crypts to the villus tips, significantly influencing molecular transport and cell metabolism[58–60]. Unfortunately, 2D membrane-based models often lack the capacity to replicate the full shape or size of target organ structures crucial for the formation of the aforementioned microenvironments. Consequently, essential features, especially gut villi and its embedded capillary systems, remain poorly reconstructed, mainly due to the absence of a supporting foundation on flat membranes.

Nevertheless, several researchers have developed 3D scaffolds that mimic the physical features of human villi[53,54,61,62]. In **Scheme 2.1B**, we compare the general differences between the models. 2D models are primarily based on the assembly of a permeable membrane within the outer housing, with basolateral flow passing through all cultured cells, supplying nutrients, and collecting waste and samples. In contrast, casted 3D models rely on a casting process, typically involving a master mold and several secondary molds for the entire procedure. The development of 3D systems has enabled the interrogation of shear stress effects on cell physiology, the therapeutic potential of probiotics, and even their suitability as implants. Interestingly, cell responses (e.g., tight junction formation and protein expression) to flow are entirely reversed when measured

in 3D versus 2D systems[53]. However, casting scaffolds still face challenges in providing information on molecule distribution and mass diffusion due to the absence of embedded microstructures, particularly capillaries.

The advent of 3D printing has significantly enhanced our ability to construct scaffolds with diverse geometries. In this study, we demonstrated two 3D printing techniques to create villi-on-a-chip models for different purposes: (i) Digital Light Processing (DLP)-based resin 3D printer for rapid villi sheet fabricated, and (ii) two-photon direct laser writing 3D printer for reconstructing critical molecular and fluidic transport features on villus.

First, compared to conventional casting methods that take hours or days to fabricate 3D geometries, we demonstrated how DLP-based additive manufacturing can enable researchers to rapidly prepare scaffolds with desired 3D geometries in just one hour. Instead of employing a laser to draw rounded lines and gradually form the final structure, DLP utilizes a projector screen to project layers of square voxels, constructing entire layers simultaneously. Notably, without special coating, we were able to establish an epithelial monolayer on the supporting materials with a similar time frame as reported previously [54,61]. That is, the 3D-printed villus structures supported Caco-2 cell proliferation vertically up a 1 mm scaffold within two weeks of growth and ultimately expressed desired tight junction formation after 21 days of culture.

Next, we developed a 3D-printed human villus-on-a-chip model featuring an internal capillary system that facilitates molecular transport from the capillary through the villus and into the luminal regions. The capillary extends from beneath the native-like crypt

region up to the villus tip. Additionally, the high-resolution two-photon direct laser writing (DLW) (< 1 μm) used for fabrication enables the inclusion of intricate geometries that provide unique biological niche microenvironments, such as pores along the vertical walls of a villus. Owing to the 3D printing system[10,63,64], critical factors such as surface porosity, curvature, surface roughness, and channel size can be precisely adjusted to support native-like cell growth and molecular transport.

Furthermore, we have incorporated translucent printing materials that allow optical monitoring of intestinal epithelial cells. Notably, without staining, we were able to periodically track cell proliferation and cell-cell boundaries throughout the entire duration of an experiment. The 3D-printed villus structures supported Caco-2 cell proliferation vertically up a 1 mm scaffold within two weeks of growth, particularly when coated with collagen and Matrigel. Utilizing Z-stacked confocal microscopy images, we determined epithelial barrier thickness and cell closure at the villus tips. To demonstrate the functioning capillary, we employed engineered red fluorescing bacteria to visualize and analyze the capillary flow embedded within the villus structure. By fluidically connecting our previously published modular cell cytotoxicity sensor[29], which can be attached without disturbing cell environments, we observed minimal cell cytotoxicity throughout the experiment. Additionally, we established and characterized molecular transport through capillary walls, villus walls, and into the luminal regions of the in vitro system. Depending on the selected printing parameters (e.g., supporting structures, slices, number of segments), printing the 3D villi took approximately 20 minutes to an hour, and the entire scaffold assembly was completed in less than four hours. As the geometries can be printed with micron-scale resolution,

we believe these scaffolds can provide new insights into the molecular interactions between luminal bacteria and the apical lymphatic or circulatory systems.

Finally, we demonstrated a straightforward and easily controllable method that facilitates rapid cell assembly onto the vertical surfaces of 3D-printed scaffolds. This method relies on the pressure gradient applied to the internal channel of the scaffold, which in turn generates suction on the surface of the porous scaffold. This suction has been verified to swiftly attract target elements, covering three-quarters of the available surface on the scaffold within 30 seconds. Overall, this method successfully showcased its potential to significantly reduce the time required to establish epithelium along the vertical direction or on scaffolds with unique geometries, from weeks to seconds.

A critical unmet need is understanding molecular signaling along the vertical axis of a villus. Since the assembly is rapid and provides access to molecular and morphological cues, coupling with modular analytical measurements may reveal more fundamental phenomena at the cellular and biological levels. Moreover, our villus-on-a-chip model could be incorporated into larger system structures, such as those aiming to characterize signaling within the gut-brain axis[65], which is a crucial requirement for reproducing first-pass metabolism in humans.

2.2 Materials and Methods

Fabrication of villi sheet scaffolds

The 3D printed villi sheet scaffold was designed based on size of the well of 24 well plate. The model included 800 supporting structures (one single villus was 200 μm in diameter and 1000 μm in height) with an average 230 μm wall-to-wall distance

between villi. To make the 3D printed device housing, designs were created using Autodesk® Fusion 360 and Autodesk® Inventor (Autodesk, Inc, US). M50 DLP-based 3D printer (Toronto, Canada) was used to fabricate the housing. When the printing process was completed, the substrate was placed in a bath of methanol with gentle shaking by hand for 1 minute and then dried with nitrogen. This step was repeated three times to thoroughly remove any uncured residues. The prints were then further cured under a 20-Watt UV lamp for 10 seconds followed by a 30-second rest at room temperature. This step was repeated three times to achieve full strength. Before cell platting, the scaffolds were placed in 75% ethanol and sonicated for 10 minutes. The scaffolds are then transferred to a glass petri dish containing 75% ethanol for one hour for sterilization followed by three times of DI water rinse.

Cell Culture and seeding on M50 printed scaffolds

The Caco-2 cell line was obtained from the American Type Culture Collection (ATCC) (Manassas, VA). These cells were maintained in tissue culture medium (DMEM) (Gibco, Grand Island NY) with 10% fetal bovine serum (FBS), 1× Penicillin – Streptomycin (Gibco)) in T75 flasks at 37°C and 5% CO_2 in a humidified incubator with regular passage 2 times a week. The cell cultures were washed with Dulbecco's phosphate buffered saline (DPBS, Sigma), removed from culture flasks using 0.25% trypsin–0.53 mM ethylenediaminetetraacetic acid (EDTA) solution (Trypsin-EDTA; Sigma, St. Louis, MO), subcultured in culture flasks and seeded on the printed scaffolds at a concentration of 5×10^6 cells/mL and then grown for 7, 14, 21, and 28 days. Medium was replaced twice a week. Scaffolds were checked optically using microscope every day and the viability of each culture was assayed and visualized at

the designed time point with a LIVE-DEAD viability/cytotoxicity kit (Thermo Fisher Scientific, Waltham, MA). The common circulating medium used for static and device experiments was DMEM plus 10% FBS and is referred to as “culture medium”.

Fabrication of porous villi scaffolds

The system is comprised of two principal elements that were fabricated separately: (i) the device/fluidic housing and (ii) the 3D villus scaffolds. To make the housing, designs were created using Autodesk® Fusion 360 and Autodesk® Inventor (Autodesk, Inc, US). The CAD files were then converted to writing-path using the CAM software DeScribe (Nanoscribe GmbH, Germany). Pre-cut silicon substrates (25 mm × 25 mm) were thoroughly rinsed with acetone followed by isopropyl alcohol (IPA), dried with inert nitrogen, and then baked at 110°C for 10 minutes. The negative-tone photoresist, IP-S (Nanoscribe), was dropped onto the silicon substrate and a vacuum chamber was used to remove any bubbles when necessary. The substrate was then loaded into the Nanoscribe Photonic Professional GT DLW system (Nanoscribe). The two-photon excitation was performed using the 780 nm frequency-doubled output from a 1580 nm Er-fiber laser which was eventually focused on the photoresist. The Nanoscribe was used with a 25 × objective lens in DiLL mode to print the primary molds. The channel molds were fabricated with layer heights of 1 μm and hatching distances of 500 nm For the printing process, the laser power and scan speed were respectively set to 45 mW and 100 mm/s. Due to the size of the mold structures (approximately 6 mm × 4 mm), a stitching-based print methodology was utilized by which the master mold was divided into several 250 μm × 250 μm areas that connect together. When the printing process was completed, the substrate was placed in a bath of propylene glycol monomethyl

ether acetate (PGMEA) for 20 minutes and then in IPA for 2 minutes to remove any residual uncured photoresist. The primary mold was further cured under a 20-Watt UV lamp for 1 hours. PDMS (Sylgard 184, Dow Corning, Corning, NY) was then poured over the primary molds and cured in a 60 °C oven for 3 hours. Cured PDMS housing was then released from the molds followed by punching inlets and outlets. The PDMS was rinsed with IPA, and then oxygen plasma bonded to 30 mm circular borosilicate glass substrates (#1.0, Bioptechs Inc., Butler, PA)

Surface Coating on printed scaffolds

The scaffolds were sterilized with 70% (v/v) ethanol and 30 minutes of UV light exposure before cell introduction. Sterilized scaffolds were coated with the mixture of 50 µg/mL type I collagen and 300 µg/mL Matrigel matrix (Corning, Corning, NY) at 37 ºC for 2 hours[29]. At this point, the scaffold was ready for receiving cells. If not used immediately, the coated scaffold can be put in the sterilized culture dish, covered, and stored in the refrigerator at 37°C for 24 hours.

Cell Culture and seeding on porous villi scaffolds

The Caco-2 cell line was obtained from the American Type Culture Collection (ATCC) (Manassas, VA). These cells were maintained in tissue culture medium (DMEM) (Gibco, Grand Island NY) with 10% fetal bovine serum (FBS), 1× Penicillin – Streptomycin (Gibco)) in T75 flasks at 37°C and 5% CO_2 in a humidified incubator with regular passage 2 times a week. The cell cultures were washed with Dulbecco's phosphate buffered saline (DPBS, Sigma), removed from culture flasks using 0.25% trypsin–0.53 mM ethylenediaminetetraacetic acid (EDTA) solution (Trypsin-EDTA;

Sigma, St. Louis, MO), subcultured in culture flasks and seeded on the printed scaffolds at a concentration of 5×10^6 cells/mL and then grown for 7, 14, and 21 days. When seeding on the scaffolds printed on the silicon substrate, cells were gently dropped onto the surface using 20 µL micropipette. These scaffolds were then filled with growth medium for 1 hour in order to promote cell attachment. After all cells settling down at the bottom of the scaffolds, the scaffolds were submerged to the culture plates filled with culture media and placed back in the incubator. Medium was replaced twice a week. When seeding the scaffolds in the chamber of the assembly, cells were gently transferred using 1 mL syringes and sealed the inlets and the outlets for 1 hour. Then, culture media was perfused through the channel at a constant flow rate of 5 µl/hr to continually replenish nutrients. Scaffolds were checked optically using microscope every 3 days and the viability of each culture was assayed and visualized at the designed time point with a LIVE-DEAD viability/cytotoxicity kit (Thermo Fisher Scientific, Waltham, MA). The common circulating medium used for static and device experiments was DMEM plus 10% FBS and is referred to as "culture medium".

Morphological studies and immunofluorescence microscopy

Cell images were recorded during culture using a Moticam 2500 camera (Motic China Group Co., Ltd.) with imaging software (Motic images plus 2.0; Motic China Group Co., Ltd.) on a Zeiss Axiovert 40CFL phase contrast microscope. To visualize epithelial tight junctions and nuclei, immunofluorescence staining was performed. This was typically done at the end of any given experiment. Caco-2 cells on the scaffold were fixed in 4% (v/v) 4% Paraformaldehyde (PFA) that was freshly prepared for 30 mins at room temperature followed by permeabilization in 0.25% (v/v) Triton-X-100

(Sigma, St. Louis, MO) for 5 minutes. The sample was stained using 1% BSA for 1 hour at room temperature, anti-occludin antibodies (mouse monoclonal antibody-Alexa Fluor 594; Molecular Probe, Eugene, OR) for overnight at 4°C, 2° Ig in dark for 1 hour at room temperature, 6- diamidino-2-phenylindole, dihydrochloride (DAPI; Molecular Probe, Eugene, OR), respectively. The scaffold was then rinsed 3 minutes with PBS for 3 times between each step. Following fluorescence staining, samples were visualized on a Zeiss Axio Observer Z1 epi- fluorescence microscope equipped with a photomultiplier tube and coupled to a 405 nm laser and a white light laser (489–670 nm). (CoolSNAP HQ2, 1392 6 1040 resolution; Photometrics, Tucson, AZ); computerized image analysis of recorded images was carried out using MetaMorph image software (Molecular Devices).

Statistical analysis

All assays were performed in triplicate. Results were expressed as mean ± standard error. One-way ANOVA was used to determine significant differences between groups. The level of significance was set at $\alpha = 0.05$. The Pearson product-moment correlation coefficient was applied to measure the strength of linear correlation between groups. The level of significant correlation was set at $r = 0.95$.

2.3 Results and discussion

2.3.1. 3D printing for rapid gut-on-a-chip fabrication

2.3.1.1 Fabrication of 3D villi model using DLP-based printers.

As discussed in the previous section, 3D morphology significantly influences cell differentiation and response. It is evident that cell density can vary considerably

between 2D and 3D environments. For instance, depending on the density and height of the vertical villus-like supports, the available surface area between a 2D plane and a 3D surface can differ by 5 to 7 times and greatly impact the capacity for cell proliferation (**Figure 2.1A**). However, replicating the 3D geometries of human villi can be a time-consuming and labor-intensive process.

In this study, we investigated the potential of 3D printing for rapidly generating the general shape of intestinal gut villi. Specifically, we utilized a digital light processing (DLP) 3D printer to enable rapid material stacking and established a one-step process for full-size scaffold fabrication. As depicted in Figure 2.1B, we initially designed a 3D model of a villi sheet using CAD software (Autodesk Fusion 360 and Autodesk Inventor) and employed a DLP 3D printer to fabricate the villi sheets. Thoroughly cleaning the solidified scaffold is essential, as uncured resin that remains can alter the geometry of the printed structure during the subsequent post-curing process. Moreover, residual material can be irritating and potentially induce cell death. By exposing the scaffolds to a 20-Watt UV source for 30 seconds, the structure attained its full mechanical strength. Notably, we observed that immersing the scaffolds in deionized water during the post-curing process significantly reduced the chance of annealing between vertical structures. The cured prints were then sonicated in a 70% ethanol bath for 30 minutes and air-dried in a biosafety cabinet to ensure thorough sterilization, eliminating pathogens and any remaining resin residues that could be detrimental to cells. Compared to methods such as casting, DLP 3D printing can reduce the fabrication time from a day to mere hours, depending on printing parameters such as resolution, exposure time, and stage moving speed. In our study, we were able to produce up to 12

scaffolds within an hour. This fabrication process can be easily scaled up by selecting a printer with a larger printing area.

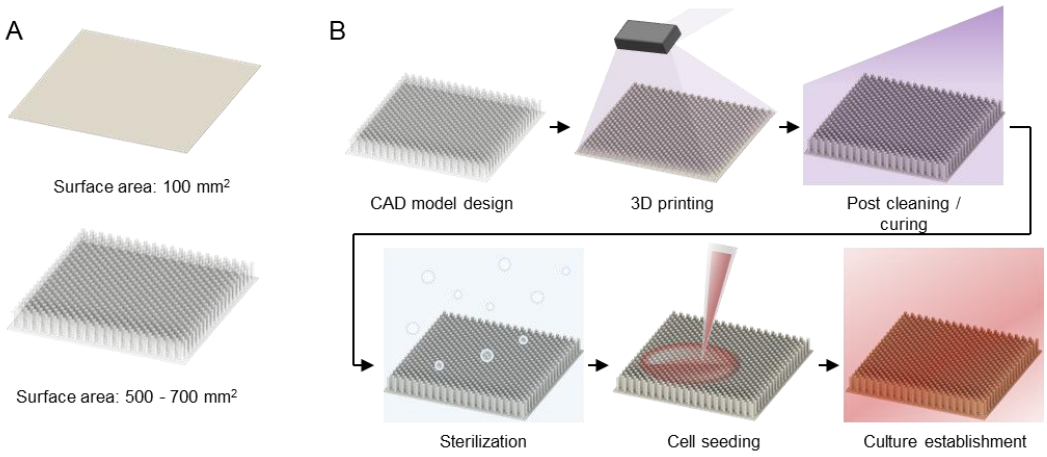

Figure 2.1 Villi sheet fabrication via DLP 3D printing.
(A) The available surface area between a 2D plane and a 3D surface can vary from 5 to 7 times depending on the design. (B) The establishment of a functional villi sheet model generally includes 6 steps: (i) model design, (ii) 3D printing, (iii) post cleaning and curing, (iv) sterilization, (v) cell seeding, and (vi) cell proliferation.

2.3.1.2 Scaffold coating and cell viability

In our initial studies, we first tested the capability of the 3D printed scaffold for hosting gut epithelial cells and the ability to generate favorable surface along the vertical direction forming a continuous epithelial monolayer. We used a 3D printed scaffold fabricated previously containing 800 3D supporting structures with an average 230 μm wall-to-wall distance between villi (one single villus was 200 μm in diameter and 1000 μm in height) on a 100 mm^2 flat surface which provided an equivalent 585 mm^2 surface for cell attachment. As illustrated in **Figure 2.2A**, upon live/dead staining with calcein-

AM and ethidium homodimer-1, respectively, we confirmed Caco-2 cell growth and viability on the 3D printed scaffold after 14 days.

As shown in **Figure 2.2B**, the image focused on the base of the scaffold clearly demonstrated the boundaries between cells and the self-constructed monolayer. Meanwhile, when focused on the vertical region of the scaffolds, we monitored the structure surrounded by the cells (**Figure 2.2C**). Similar to the epithelial cells moving from the crypts to the tips of the villi in human intestine, the cells were capable of proliferating and migrating up from the bottom of the scaffold to the top in a directional movement. This, in general, reconstructed the 3D microgeometry in human intestine. However, when closely focused on the top of the supporting structures, we recorded that the pixelated printed scaffold tips were partially covered by cells, suggesting that it may take more than two weeks to fully cover the scaffold (**Figure 2.2D**). Costello et. al. had reported the intestinal cell growth on porous PLGA scaffolds with the cells completely cover the 500 μm tall scaffolds after 7 days of culture[61]. Generally, the proliferation rate of Caco-2 cells on both scaffolds are identical suggesting that the cells maintained a similar migration progress in the region between 500 μm to 1000 μm along the vertical direction.

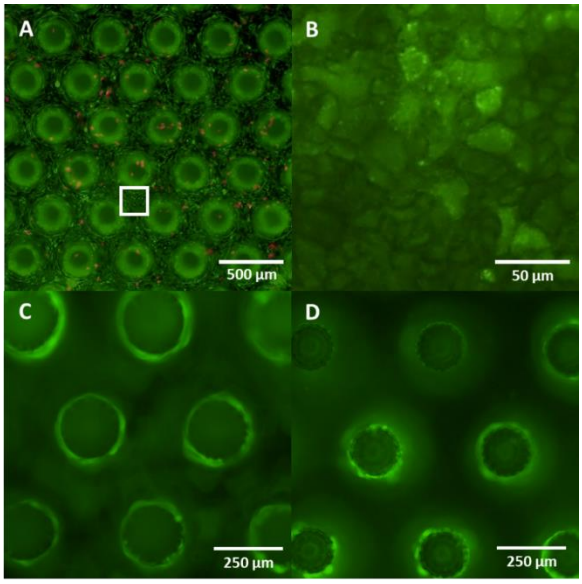

Figure 2.2 The top view of the 3D scaffold 2 weeks after the cell plating.
By applying Calcein AM and ethidium homodimer-1 on the cells, the green indicated the live cells while the red indicated the dead cells. (A) The surface of the printed scaffold was significantly covered by Caco-2 cells which, in general, reconstructed the 3D microgeometry in human intestine with the overall cell viability exceeding 95%. (B) A zoom-in picture of the bottom region of the printed scaffold showed that the surface was tightly covered by the cells with cell boundaries could be clearly seem. (C) The focal plane aimed at the 1/3 from the bottom of the printed villi scaffold. The surface of the scaffolds was covered by epithelial monolayer. (D) The focal plane aimed at the tip region of the printed villi scaffolds. The pixelated scaffold tip could be seen with part of the surface covered with cells.

Next, we assessed the impact of commonly used coating materials on the 3D printed scaffolds. Specifically, we utilized an ozone plasma cleaner to activate the scaffold surface for 30 seconds, removing absorbed organic contaminants and promoting the binding of surface coatings. Subsequently, the entire surface was immersed with 100 µL of (i) Matrigel and (ii) Type-1 rat collagen for 24 hours in a 37ºC CO_2 incubator to maximize conjugation. After removing the coating solutions, Caco-2 cells were seeded

onto the scaffolds at a concentration of 1×10^6 cells/mL. We stained the cells 14 days post-seeding using Calcein AM and examined cell morphology with fluorescence microscopy. As shown in **Figure 2.3A**, cell growth in all tested groups (bare scaffold, Matrigel coating, and Type-1 rat collagen coating) was found to be identical, indicating that the printing material is inert and biocompatible. Bare printed scaffolds were chosen for subsequent experiments.

A notable advantage of using a 3D scaffold to host epithelial cells is the increase in surface area. Specifically, the current scaffold (800 3D supporting structures on a 100 mm^2 area) provided 5.85-fold more surface area compared to a 2D environment. To determine the correlation between surface area and cell number on a 3D scaffold, we trypsinized the cells attached to 3D scaffolds at designated time points (0, 7, 14, 21, and 28 days) and evaluated cell density by dividing the cell numbers by their theoretical surface area. As illustrated in **Figure 2.3B**, with cell viabilities ranging from 90% to 98%, cells reached full confluency on the 2D surface within 4 days, while cell numbers on the 3D scaffold plateaued after 14 days. The cell ratio between the two tested conditions steadily increased for the first 14 days and reached 5.26, which is generally consistent with the surface area ratio between the two groups. Notably, we observed the formation of 3D structures, such as folds, in cells growing on 2D surfaces, resulting in cell confluency exceeding 100% at this stage. Overall, we demonstrated that the growth curve of Caco-2 cells on the 3D printed scaffold is proportional to the increase in surface area and verified that the total cell number on the scaffold correlates with the surface area expansion.

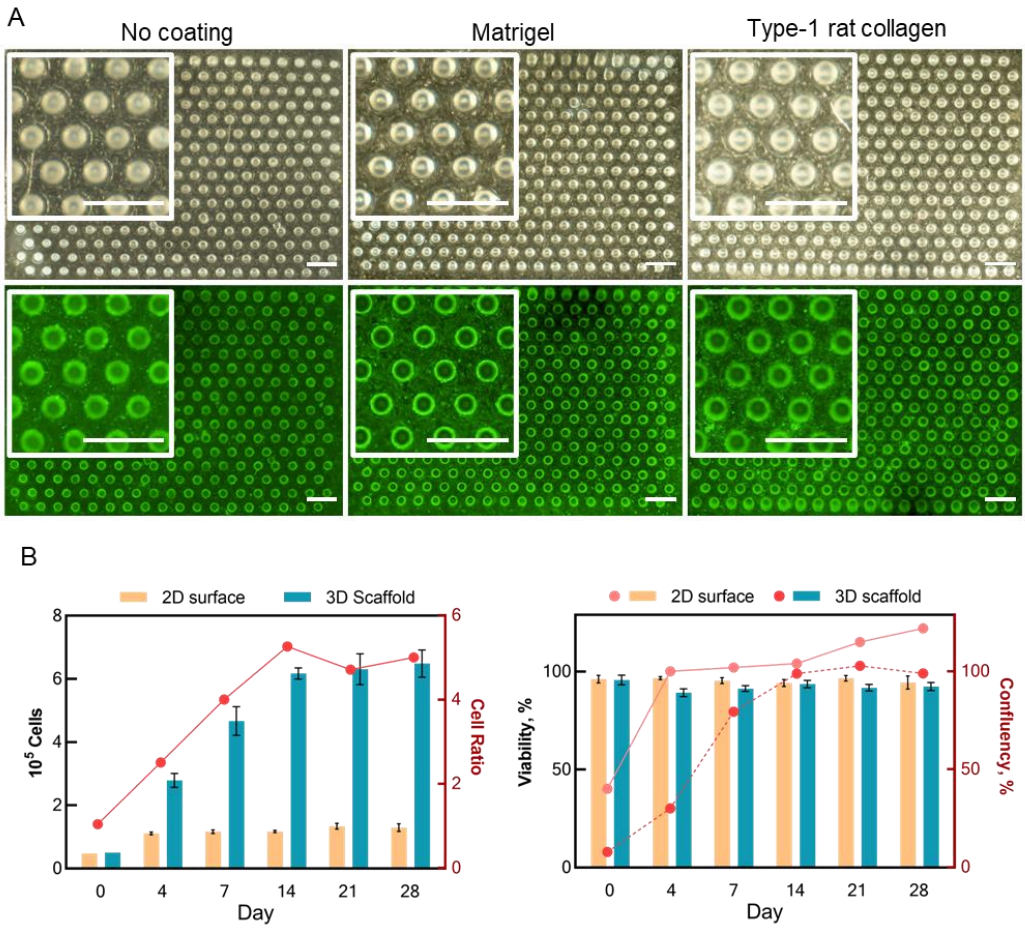

Figure 2.3 Cell growth and density.

(A) The images demonstrated that cells were able to proliferate under all tested conditions, which included bare 3D printed surfaces, Matrigel-coated surfaces, and collagen-coated surfaces. (B) The 2D flat surface group was seeded with 40% confluency, adhering to established protocols. However, since the bottom flat area represented only 10% of the total surface area, the 3D scaffold group was initiated with 8% confluency to avoid cell stacking. At each predetermined time point, cells on the 2D surface and 3D scaffolds were trypsinized and counted. Cell viability and confluency were monitored and documented at designated time points. Both groups exhibited cell viabilities ranging from 90% to 98%. After 21 days, we observed the emergence of 3D structures, such as folds, suggesting that cell confluency surpassed 100% on 2D surfaces at this stage. *(n = 3)

Tight junctions between cells are among the most critical features of intestinal epithelium, as they provide a physical barrier that restricts molecular transport across cells. Evaluating tight junction formation is essential for understanding whether cells differentiate and express the desired characteristics within the cultured microenvironment. To evaluate tight junction formation in Caco-2 cells in both 2D environments and 3D scaffolds, we prepared two experimental models: (i) the 3D-printed model described earlier, and (ii) a 2D sheet generated by removing all 3D features from the original 3D model. Both models were printed using the same resin and 3D printer as previously mentioned, ensuring that cells were exposed to identical material and physical conditions. Cells were cultured for 21 days in DMEM containing 10% FBS in a 37°C incubator with 5% CO_2. To visualize and assess cell differentiation and tight junction formation, we then performed immunofluorescence staining using anti-occludin antibodies that target tight junction proteins. As depicted in **Figure 2.4A**, cells cultured on flat surfaces underwent a self-assembly process, resulting in "folds" after 21 days. This observation is consistent with results reported by other research groups, indicating that cells cultured on microfluidic resins for 3D printing can generate morphologies similar to those observed on 2D PDMS surfaces. Furthermore, the cells successfully expressed the desired tight junction protein, ZO-1 (labeled in green).

We next investigated tight junction expression in cells on the 3D scaffold. Following the same staining protocol, we utilized confocal microscopy to evaluate tight junction formation at various focal planes. Both AF488-labeled anti-ZO-1 protein and AF594-labeled anti-ZO-1 protein were employed to detect ZO-1 proteins secreted at tight junctions. The bottom left scheme indicates the focal plane of Figure 5B, 5C, and 5D.

As shown in **Figure 2.4B-D**, the images captured at the bottom, middle, and tip regions of the villi scaffold, respectively, reveal green or red fluorescence staining of ZO-1 proteins across all cells attached to the 3D scaffold. This finding suggests that Caco-2 cells indiscriminately established tight junctions in the 3D environments, similar to the 2D setups. Enlarged images focusing on cells at the tip region and middle cross-sectional area further confirmed that cells attached to the scaffolds formed a monolayer, as opposed to adopting a folding geometry as they do on the 2D environment **Figure 2.4E-F**. We hypothesize that this reduction in the self-folding process is due to the cells on the 3D scaffold receiving adequate support from the printed material.

In summary, we have shown that intestinal 3D cellular morphologies and critical physiological features, such as tight junctions, can be reconstructed on a 3D printed scaffold using DLP-based additive manufacturing. This rapid fabrication method eliminates the labor-intensive assembly process associated with conventional models and demonstrates its potential to customize structural geometries for research aimed at investigating cell migration and differentiation in 3D environments.

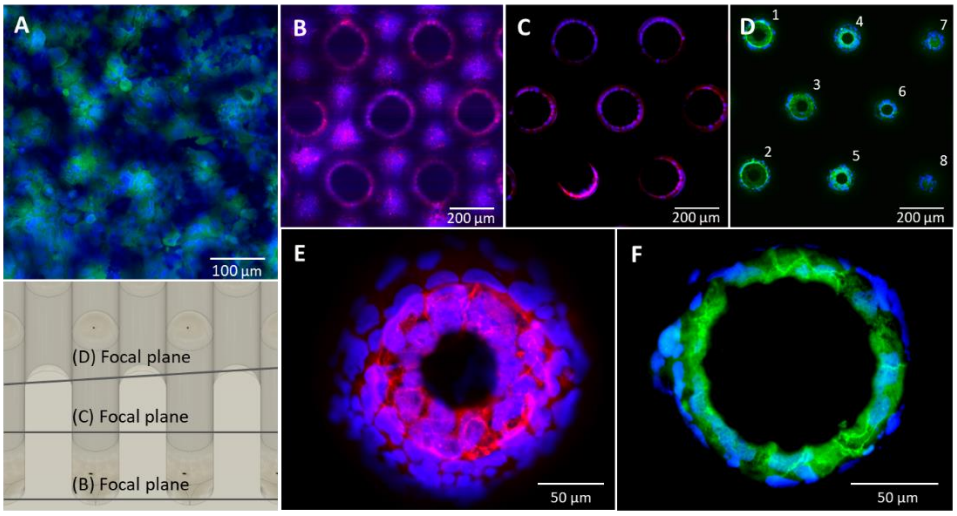

Figure 2.4 Immunostaining of the cells.

(A) Three weeks after the cells being seeded on a flat surface printed with the same resin used for the 3D scaffolds. The cells self assembled into "folds" after 21 days which matches the results reported by other research groups. (B) The cells at the bottom of the scaffold. (C) The cells at the middle of the scaffold formed a monolayer covering the surface. (D) The tilted focal plane at the tip region showed the clear cells boundaries and the tight junction formation. (E) A zoom-in picture of the cells at the tip region. (F) A zoom-in picture of the cell at the middle cross-section area. Blue: Nuclei (DAPI), Green: ZO-1 protein (AF488), Red: ZO-1 protein (AF594).

2.3.2 High Resolution 3D printed Human Villi-on-a-Chip with Capillary to Enable Transepithelial Molecular Communication

2.3.2.1 The design and fabrication of the biomimetic human villi-on-a-chip

As discussed in the previous session, the 3D microenvironment is crucial for recapitulating native biological function in an *in vitro* system. Here, we explored the potential of utilizing 3D printing to create delicate features embedded in the intestinal gut villi. Specifically, for the first time, we applied a high-resolution (< 1 µm) two-

photon 3D printing strategy for the piecewise construction of a full-size villus architecture which combines many attributes of previous gut-on-a-chip models, such as flow access, optical transparency for fluorescence staining, and permeability for molecular exchange. The printed scaffold has more realistic biomechanical properties, including size, shape, curvature, and an embedded fluid transport system, which were absent in earlier models due to a lack of suitable 3D fabrication methodologies.

As illustrated in **Figure 2.5A**, the villus-on-a-chip comprises two major compartments: (i) the 3D printed villus scaffold, and (ii) the PDMS housing that enables fluidic transport. Together, the two compartments establish an easy-to-operate microfluidic system. To fabricate the PDMS housing, we 3D printed the master mold and used PDMS to cast the outer housing with microfluidic channels designed to match the connecting channel on the printed villus scaffold. Meanwhile, the villus scaffold was initially printed on an ITO glass substrate, where two-photon beams were focused within a drop of IP-S negative-tone photoresist and crosslinked the resin monomers into desired features. As one of the most critical features in organ-on-a-chip models, molecular transport is usually realized via the assembly or integration of porous membranes common in 2D sandwich-type systems[51,66]. However, the porosity is printed into the scaffold in this model through 3D printing which significantly eliminates the effort for manual assembly. After removing photoresist residue and completing the final curing process, the scaffold and the PDMS housing were precisely aligned and joined under a microscope, forming a closed system that mimics human villus morphology and its surrounding environment. As illustrated in **Figure 2.5B-C**, we could clearly identify printing details and surface topology under the microscope.

The lines represent the slicing of the print on the z-stack, while the underlying triangles indicate the supporting structures. The concentric slicing patterns demonstrate the bottom-up printing strategy. Meanwhile, when the scaffolds were printed horizontally, it resulted in vertical slicing patterns for the villus which can be verified by the displayed side view and surface patterns of the scaffold (**Figure 2.5D-E**). To better fabricate micro-features with high resolution, smaller blocks were printed in order and "stitched" together to develop the full-size structure. The stitching boundaries between the small sections are visible in both the top view (**Figure 2.5B**) and side view (**Figure 2.5D**) of the print. The images also highlight the optical characteristics of the printing material. The translucent material enables cell growth characterization without additional staining processes. As demonstrated in **Figure 2.5F**, the SEM photo focuses on the tip region, revealing the surface topology of a villus printed with a 1 μm vertical slicing resolution. The arrows indicate the 5 μm pores printed simultaneously with the villus main structure. Finally, we present the SEM image of the entire structure, further demonstrating the uniformity of the pores on the smooth walls. The quality of the scaffold under a specific printing resolution (1 μm) is sufficient to mimic and recapitulate human villus morphology (**Figure 2.5G**).

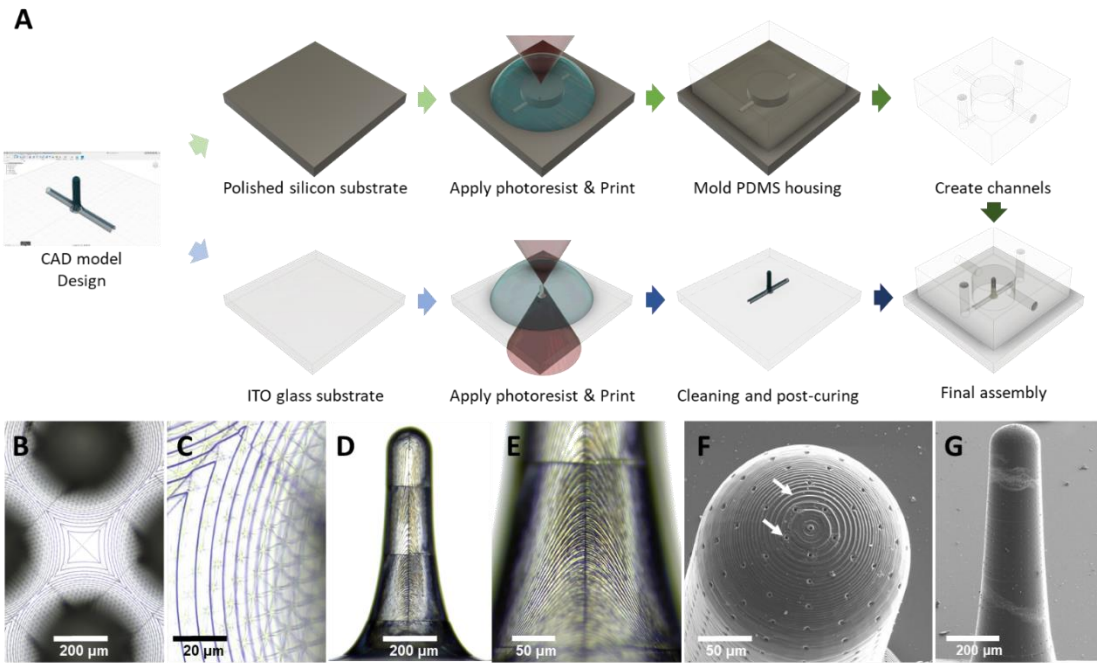

Figure 2.5 Villi-on-a-chip fabrication and printed scaffold verification.

(A) CAD models for both the housing and villi were created. A positive master mold was printed on a silicon substrate, and PDMS was employed to generate the upper housing. Subsequently, ITO glass served as a substrate to support the printed villi, and the two components were assembled to form the final system. (B) For increased precision, smaller sections were printed individually and "stitched" together to complete the design. The top view of the villi revealed the slices and stitching boundaries between these smaller sections. All sections were well-aligned and seamlessly joined. (C) The internal supporting structures were visible due to the transmittance of the printing material, enabling quality assessment and future cell monitoring using conventional microscopes. (D, E) The side view of the villi also displayed the stitched sections. Surface patterns indicated that the structure was printed using a point-by-point and layer-by-layer process. (F, G) SEM images demonstrated that the printing resolution was sufficient for reconstructing critical surface micro-features. The diameter of the surface pores measured 5 µm, a size commonly employed in other models to facilitate cell functions.

2.3.2.2 Cell hosting capability of the printed scaffold

In our study, we aimed to evaluate the ability of IP-S scaffolds to support Caco-2 cell growth and, crucially, their vertical proliferation along the villi sides to establish a complete monolayer on the 1 mm structure. Prior to cell seeding, the sterilized scaffolds were either left uncoated or coated with various materials functioning as extracellular matrices to enhance viability and proliferation. We conducted a series of experiments using (i) uncoated printed scaffolds, (ii) Matrigel, (iii) collagen, and (iv) a Matrigel-collagen combination. Specifically, all scaffolds were sterilized with 75% ethanol, air-dried, and placed in a biosafety cabinet with UV exposure for a minimum of 2 hours. Coating solutions (50 µg/mL type I collagen, 300 µg/mL Matrigel matrix, and the mixture) were freshly prepared and applied to the scaffolds, followed by incubation at 37°C in 5% CO_2 for 2 hours before cell seeding. The villi were then assembled within the entire device and treated with the respective surface coating materials. Subsequently, they were incubated (37°C) for up to 28 days and monitored twice a week using a phase contrast microscope.

In our initial experiments, we observed cell proliferation and migration from the bottom substrate to the uncoated printed scaffold for 14 days post-seeding. Owing to the transparent nature of our printed scaffolds, we monitored and assessed growth under a light microscope twice a week under the tested conditions. Typically, *in vitro* OOCs are visualized only once, at the end of an experimental procedure. Upon live/dead staining with calcein-AM and ethidium homodimer-1, respectively, we confirmed Caco-2 cell viability on the scaffold. Fluorescence images showed that cells were generally highly viable (> 95%), with a few dead cells localized in the crypt regions

(**Figure 2.6A**, top view). Notably, in the side view of Figure 2A, we observed no evident vertical proliferation, corroborating findings obtained with the light microscope. In the experiments illustrated in **Figure 2.6B**, we pre-coated the villi with an ECM coating (type I collagen/Matrigel mixture) and allowed the same cells to proliferate for an identical 14-day period. In this case, the uncoated printed scaffold fluoresced red, while the cells on the far-right image were stained with Calcein AM, indicating high viability and full vertical proliferation. **Figure 2.6C** presents optical phase contrast images of the same scaffolds, emphasizing the junctions between cells and the apparent uniform monolayer. These results confirmed the coated printed villi scaffolds' biocompatibility for cell growth.

To further characterize proliferation, we coated scaffolds with different extracellular matrices in triplicates and cultured the cells for 28 days. We monitored cell growth optically twice a week and recorded the height cells reached vertically along the supporting structure. We discovered that cells grew more slowly but ultimately proliferated and fully covered the scaffold within 28 days post-seeding when the scaffold was coated with collagen alone. The combination of Matrigel and collagen facilitated cell growth in the vertical direction. Cells cultured in media supplemented with collagen exhibited limited attachment to and migration up the scaffold. The vertical migration of cells surpassed that of cells on scaffolds with surface coatings, as mentioned earlier, indicating that the additional collagen in the culturing media provided limited assistance in promoting cell growth vertically on the scaffold. In **Figure 2.6D**, we present the optically visualized height of cells growing on the scaffolds as an indicator of the benefits offered by various ECMs. In the case of no

surface coating, cells remained solely at the bottom (~100 μm). By contrast, scaffolds coated with a mixture of type I collagen (50 μg/mL) and Matrigel (300 μg/mL) facilitated complete cell coverage across the entire scaffold within 14 days after the initial cell seeding.

Three key factors considered when developing biocompatible scaffolds to mimic human tissue are material biocompatibility, sustainability, and mechanical properties. PLGA has been widely used in tissue support structures or scaffolds, including human villi, due to its exceptional mechanical performance[54]. The printing material employed in this study was an acrylate-based photoresist, which exhibits mechanical properties similar to PLGA. When fully cured, it has a Young's modulus comparable to that of 50:50 PLGA (4.6 GPa versus 2.0 GPa, respectively[67,68]), providing the villus scaffold with adequate durability against environmental stressors such as shear stress and corrosion. However, stiffness may also pose a significant limitation. The native villi's Young's modulus is 1.03 MPa[69], indicating that the printed scaffold may not be capable of replicating the physical movements of native villi (e.g., bending induced by flow). Nevertheless, the elasticity of the printed scaffold could be adjusted by replacing the current photoresist with other biocompatible, photo-crosslinkable hydrogels (e.g., PEG-DA) or composite materials.

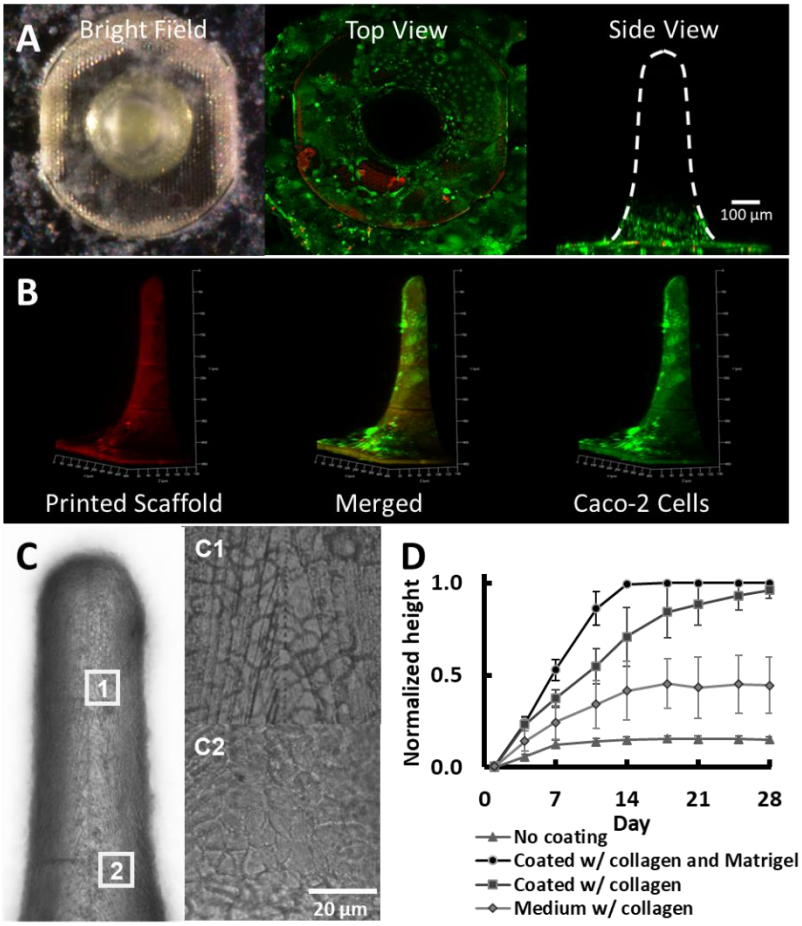

Figure 2.6 Cell culture and viability.

(A) Live/dead staining shows that, without ECM coating, cells could still adhere to bottom region of the printed scaffold but would experience a significant slowdown in the further vertical migrate to the tip region after 14 days, while (B) with proper ECM coating, the scaffold has been shown to full covered with cultured cells after 14 days. (C) The transmittance of the printing material, IP-S, offers the capability of real-time high-resolution cell morphology monitoring without further staining process. (D) Cell could only reach a certain height on the uncoated scaffold, while high cell confluency was monitored on the scaffold coated both type 1 collagen and Matrigel. *(n = 3)

2.3.2.3 Reconstruction of intestinal epithelial barrier in vitro

To fully reconstruct the functions of intestinal epithelium on the printed scaffold, both cell confluency and differentiation were evaluated. As demonstrated earlier, the scaffold was entirely covered with cultured cells after 14 days, and the cells remained more than 95% viable throughout the 28-day culture period. To visualize and assess cell differentiation and tight junction formation, we performed immunofluorescence staining at day 21 using anti-occludin antibodies that target tight junction proteins. Confocal microscopy revealed that cells had proliferated and formed tight junctions along the entire length and base of the scaffold (**Figure 2.7A**). Close-up images display slices at the top (**Figure 2.7B**) and 500 μm from the bottom (**Figure 2.7C**). **Figure 3B-C** also demonstrates epithelial cell morphology on the IP-S-based scaffolds after 21 days of culture. Notably, in the cross-section image, we found that the shell thickness corresponded to a monolayer of cells and that the cells had not penetrated the porous printed scaffold. Interestingly, we observed a slightly higher cell density at the tip region and base of the villi, as indicated by more intense anti-occludin staining. This finding aligns with previous results from a PLGA-based scaffold and native human epithelium *in vivo*[61].

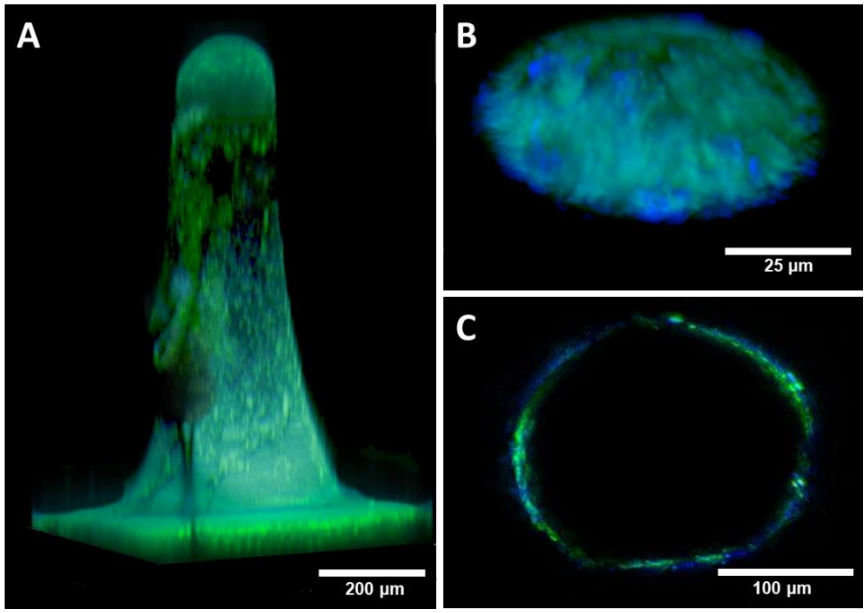

Figure 2.7 Immunostaining of the cells on a porous villus scaffold.
(A) Confocal microscopy of a 3D printed scaffold cultured with Caco-2 with the staining for nuclei (DAPI, blue) and ZO-1 tight junction protein (Alexa Fluor 594, green). The picture shows fully developed tight junction by cells on the scaffold after 21 days, (B) four times magnification shows full coverage at the tip region of the scaffold 21 days, and (C) Z stack image shows the well-developed monolayer of epithelium around the scaffold.

2.3.2.4 Reconstitution of molecular transport functions in vitro

The embedded capillary system is a crucial feature of human villi, enabling rapid exchange of biological materials at the interface and delivering essential substances to support other organs. Conventional filter-based 2D models, which introduce additional resistance that delays molecular transport, often struggle with rapid sampling and real-time sensing. In this study, we designed and fabricated channels within the villi to reconstruct the transport function of human villi. By coupling these channels with a

porous surface, we aimed to improve transport efficiency between the lumen and apical sides of the intestinal epithelial cell (IEC) barrier. We employed COMSOL's fluid simulation capabilities to design and test various conditions *in silico*, aiming to understand molecular exchange in both the bare printed scaffold and the model with intestinal epithelium. Additionally, we compared simulation results with images collected via fluid tests with fluorescent dye to verify the scaffold design.

To establish a villi transport model in COMSOL, we used the same parameters as in the previous printing process (1000 μm in height, 200 μm in diameter). We initially set the surface pore size to 5 μm in diameter, with a 20 μm distance between each pore. To simulate actual culture conditions, we filled the fluidic environment with culture media (DMEM w/ 10% FBS; viscosity: 1.011 Pa·s[70]) in a chamber measuring 5 mm in height and 4 mm in diameter. To model fluidic movement, we set the media to continuously flow from left to right at a rate of 10 μL/hr from time zero. A 20-μm-deep capillary was situated beneath the 5-μm-thick wall. The fluid was set to contain 1 mM of solute (diffusion coefficient: 1e-9 m^2/s) with a flow rate of 3.6 μL/hr, which was used in real fluid tests. We set the endpoint pressure at the outlet to 0 Pa. For scaffolds covered with intestinal epithelium, we set the cell layer thickness to 5 μm to mimic a monolayer of IECs. We assigned a diffusion coefficient of 5e-13 m^2/s to this "thin diffusion barrier" to model molecule permeation across the IECs (the normal drug permeability coefficients in human intestinal epithelial (Caco-2) cells range from approximately 5e-9 to 5e-7 m/s, with a partition coefficient of 0.01[71]).

As illustrated in **Figure2.8**, the color gradient represents solute distribution, with red and blue indicating the highest concentration (1 mM) and 0 mM, respectively. In the upper row of **Figure 2.8A**, rapid molecular movement from the basolateral side to the apical side was observed when the scaffolds were not covered with IECs. This demonstrates the porosity of the printed scaffold, which successfully eliminates the unwanted resistance that hinders molecular transport in many membrane-based models. In the lower row of **Figure 2.8A**, with the fully established Caco-2 monolayer covering the scaffold, permeation across the IECs was substantially controlled due to the barrier provided by the cells and tight junctions. Taken together, these findings highlight the porosity and transport control of this printed model, which offers low molecular retention and high transport efficiency. We then compared our *in silico* results with real images (**Figure 2.8B**). We filled the chamber with collagen solution and conducted tests without flowing through the capillary but with phosphate buffer containing FITC introduced by pressure and paused for 10 minutes. The observed fluorescent gradient near the scaffold surface indicated molecular movement from the capillary to the surrounding media, aligning with the results of the COMSOL simulation shown in **Figure 2.8A**.

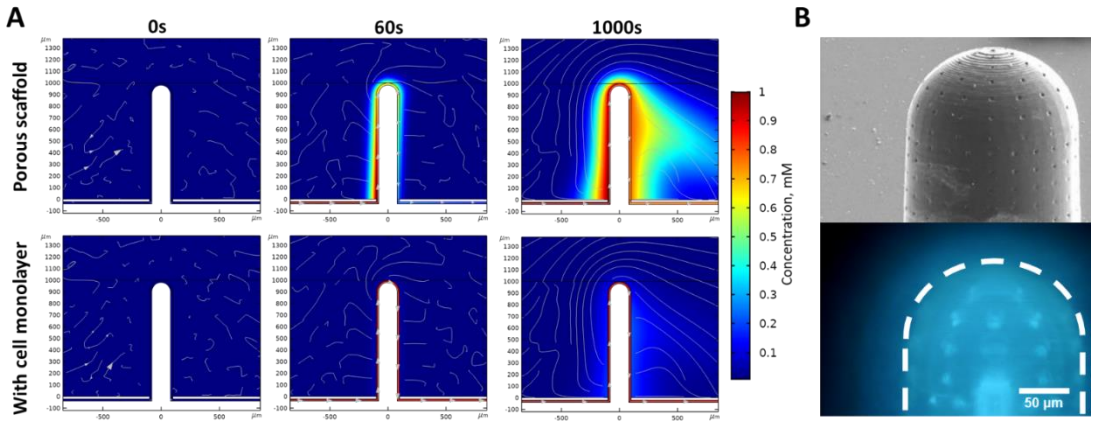

Figure 2.8 The molecular diffusion improvement due to the porous structure.
(A) The upper row showed the molecules inside the capillary quickly move across the printed structure via the designed pathways (surface pores). The bottom row, however, demonstrated the molecular transport may be influenced by a fully reconstructed cell monolayer on the surface of the scaffold. (B) We perfused a fluorescent dye into the scaffold through the internal capillary and observed the fluorescent gradient near the surface which coheres the result of COMSOL simulation we have in A.

We next aimed to examine and track fluid transport along the embedded capillary system within the villi. Factors such as structural sustainability, mechanical strength, and flow rate require further investigation for model optimization. The resultant scaffold thickness was approximately 5 μm, providing sufficient support for the entire structure. As shown in previous test results, this thickness is adequately thin to facilitate molecule exchange at the interface. In the final model assembly, two fluidic pathways were designed to support system operation. The upper part of **Figure 2.9A** displays the cross-section of the device assembly. Capillary fluid was pumped into the microfluidic channel, entering the printed villus from the bottom left, rising to the tip region, and then exiting the system via the outlet at the bottom right. Meanwhile, at the bottom of

Figure 2.9A, a fluid representing the culturing environment could be introduced into the chamber through another pair of inlet and outlet on the PDMS housing.

To further evaluate capillary flow in the operational villus-on-a-chip, we first established an intestinal epithelium monolayer (with fully formed tight-junction barriers) on the scaffold (**Figure 2.9B**). When tested with phosphate buffer, we observed no resistance to fluid flowing into the capillary channel, through the channel, and out into the connecting tubing. Moreover, the tested flow rate did not disrupt the Caco-2 monolayer. We then utilized E. coli cells (~1 μm) engineered to constitutively express dsRed marker proteins as a probe for fluid tracking and analysis. The engineered red-fluorescent E. coli probe was introduced into the system at 10 μL/min. To distinguish between the intestinal epithelium and moving probes, we stained the Caco-2 cells with Calcein-AM. In **Figure 2.9C**, we could visualize both intestinal epithelial cells (IECs) (green) on the outer surface and bacteria (red) within the capillary. However, we found that if the pressure difference between the luminal and apical sides of the villi exceeded 1000 mPa, the cell monolayer might potentially detach from the scaffold (**Figure 2.9D-E**). To address this concern, a "push-pull" perfusion methodology can be employed to reduce or regulate internal pressure in the villi. Equal amounts of positive pressure and vacuum were applied at the inlet and outlet, respectively, maintaining the basal pressure in the scaffold close to atmospheric pressure on the apical side.

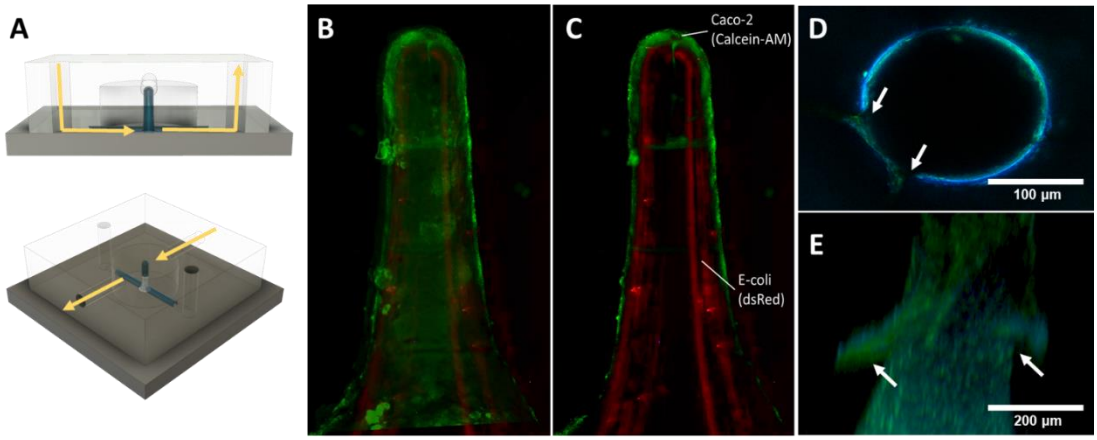

Figure 2.9 The capillary flows in the scaffold.
(A) The device has two pairs of the inlets and outlets. One is for the capillary flow (upper) while another is design for chamber fluids (bottom). (B-C) The Caco-2 cells were stained with Calcein-AM, while the engineered red fluorescent E. coli cells were used to indicate the capillary flow. (D-E) The over-pressure might potentially damage the epithelium and cause cell rupturing from the scaffold.

To demonstrate how the embedded fluid channel design and the 3D printed structure contribute to improved time resolution and sample collection, we performed additional COMSOL simulations. In **Figure 2.6**, we compared molecular transport in both 3D cast villus models and 3D printed villus models with internal fluidic channels. In **Figure 2.6A**, we explained the differences between the two systems. For the cast model, we established a cell monolayer on the porous PLGA scaffold, which is essentially a solid hydrogel that permits limited molecular transport. Conversely, the other image depicts a capillary with diffusion resistance, representative of a printed villus coated with ECM and an epithelial monolayer (~10 μm). In both COMSOL scenarios, we introduced an "environmental flow" containing 1 mM of small molecules to mimic culturing conditions.

In **Figure 2.6B**, we demonstrated and compared molecular movements in both models. The color gradient indicates solute distribution in the cross-section of the model, with red representing the highest concentration (1 mM) and blue representing 0 mM. As shown on the left, uneven molecular transport was observed in the cast villus. Based on the color gradient, diffusion started earlier in regions exposed to higher flow rates, such as the bottom-left area before the villus and the tip region of the villus. This uneven local distribution primarily resulted from non-uniform "transport resistance" and traveling distance along the horizontal and vertical axes. Consequently, this would form "hot spots" on the villus and further impact the time resolution during sample collection. In other words, the same environmental exposure on the surface could potentially lead to varying results, ultimately guiding different biological conclusions.

On the right side of **Figure 2.6B**, no hot spots were observed due to the capillary design and porous scaffold. As previously tested, we showed that the scaffold has little or no resistance to molecular exchange across the structure. Simultaneously, the transport distance from the surface to the capillary remains uniform in this 3D printed model with fluid channels beneath the "shell." As a result, all molecules at the surface experience the same "transport resistance" (a monolayer of Caco-2 cells, ECM layer, and the printed villus scaffold) before reaching the underlying fluid channel. This significantly mitigates concerns regarding sample mixing and enhances the precision and representativeness of sample collection. As the capillary collects samples from a single villus, this model may offer a "single villus resolution," potentially providing new insights into intestinal biology. Finally, we compared several representative chip-based gut models, as shown in the table.

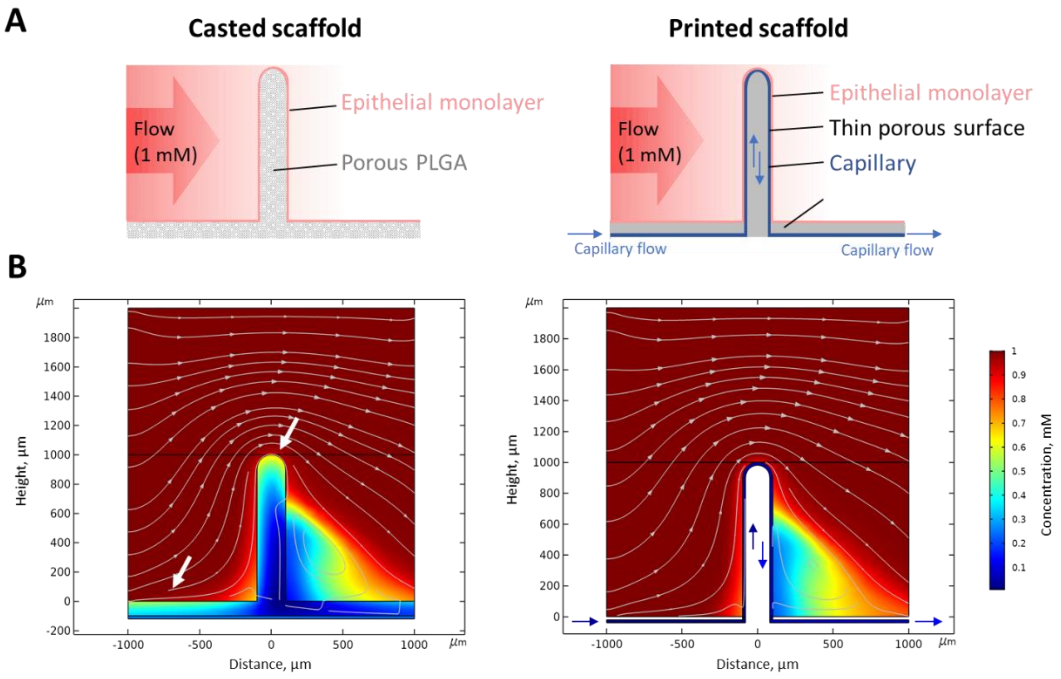

Figure 2.10 Molecular transport difference between casted 3D model and printed 3D model with capillaries.

(A) In both models, an environmental flow with 1 mM of small molecular was introduced into the system from the left to mimic the culturing condition. A porous PLGA covering with a Caco-2 cell monolayer was designed to represent the casted model. A thin, porous structure with a surface Caco-2 cell monolayer and a capillary flow underneath was used to represent the villus-on-a-chip model in this research. (B) On the left, hot spots that indicated ununiform molecular transport could be monitored mainly at the tip and bottom flat region. On the right, the capillary may ensure the sample transport and avoid sample retention at the structure which offers a “single villus resolution”.

Table. 1 Comparison of chip-based gut models.

Model type	Supporting material	Young's modulus	Important feature	
2D porous membrane	PDMS	Not reported	Physiological peristaltic motions	51,66
Cast 3D scaffold	PLGA	2.0 GPa	3D structure with co-cultured probiotics	54
Cast 3D scaffold	PEVA	30 MPa	Long-lasting scaffold material	53
Cast 3D scaffold	poly(glycerolsebacate)	5.6 MPa	Similar elasticity with actual villi	69
Cast 3D scaffold	collagen	Not reported		62
3D-printed villi	IP-S photoresist	4.6 GPa	3D printed scaffold with villi capillary	This work

2.3.3 Rapid Cell Assembly on 3D-printed Microscaffolds

As previously demonstrated, the formation of desired morphologies, such as epithelial monolayers, in the vertical direction typically relies heavily on cell self-assembly (upper panel of **Figure 2.11A**). However, this process can be time-consuming and fraught with uncertainties. In this study, we assessed an active cell distribution technique that promoted even cell distribution on printed 3D structures and accelerated the development of critical features compared to passive cell seeding methodologies (lower panel of **Figure 2.11A**). Specifically, as depicted in **Figure 2.11B**, we envisioned utilizing a fluidic system to guide the movement of target cells, with precise control achieved through pressure regulation. In this system, we first immersed the scaffold surface in media containing cells. Under normal circumstances, cells exhibit limited ability to attach to vertical surfaces due to gravitational settling. However, when negative pressure was applied to the internal space of the scaffold, we generated a pressure-driven flow that transported the media from the exterior to the interior of the

scaffold. Simultaneously, this pressure-driven flow exerted a force that mobilized the cells within the media. Upon reaching the micro-openings on the scaffold, cells obstructed these openings due to the size discrepancy between the cells and the openings. Maintaining constant pressure, we then removed the cells in the media and supplied fresh growth media to the scaffold-bound cells for proliferation. Overall, our goal was to facilitate cell assembly on complex 3D geometries and provide practical solutions for intricate tissue engineering *in vitro* models.

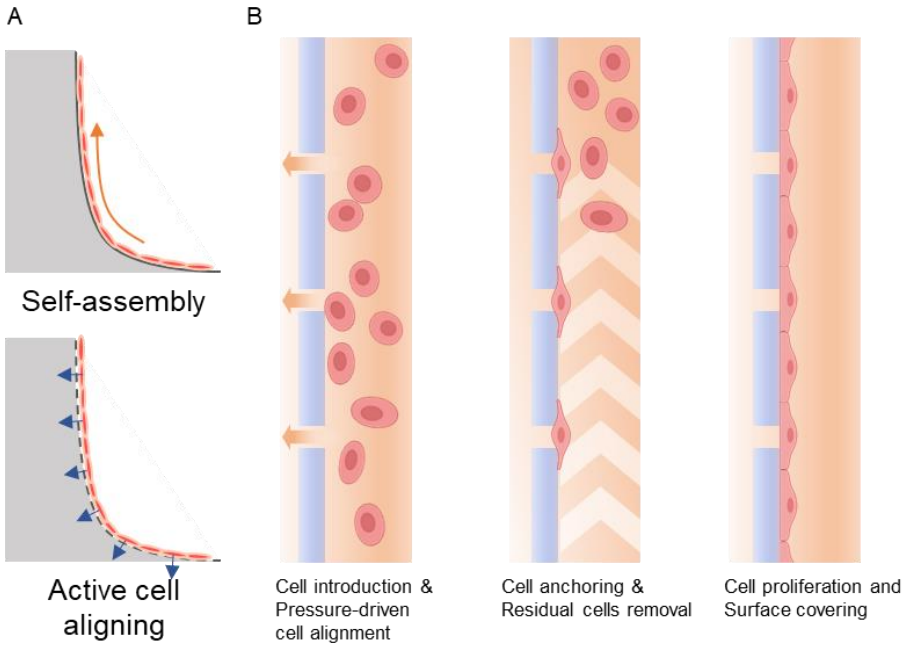

Figure 2.11 Rapid cell assembly via pressure-driven flow.
(A) Schematic representation of two different cell assembly strategies. The one on the top indicates the conventional epithelium formation via self-assembly. The one at the bottom shows the cell alignment via additional flow manipulations. (B) The pressure-driven flow generates the forces and guide cell movements. With higher initial cell density on the vertical surface, the surface can be rapidly covered, and the establishment of the epithelium can be significantly accelerated.

2.3.3.1 Development of the fluidic system for pressure regulated cell assembly.

Pressure and fluidic uniformity are likely dependent on fluidic system design, and their quality may determine cell assembly and viability. In our initial study, we employed a simulation tool to assess pressure uniformity and fluidic performance. Specifically, we created a 2D model representing the porous surface of the scaffold, using the Laminar Flow module of the commercially available COMSOL Multiphysics software. This allowed us to visualize and predict fluidic patterns at various locations and pressure within the defined area on the scaffold. (**Figure 2.12A**). In this model, we used a porous wall (containing 5 μm holes) that represented the surface of printed scaffolds which, meanwhile, defined the exterior (top region in the model) and interior (bottom region in the model) environment. There were two exits in the internal channel for pressure and flow regulation. As illustrated in the top panel of **Figure 2.12B**, we applied a negative pressure at the bottom left and right exits of the scaffold which aided a directional pressure-driven flow. This was seen to facilitate the movement of the liquid sample from the top open area into the scaffold. The uniformity in color observed in the bottom panel of **Figure 2.12B** suggests that the fluidic resistance was likely evenly distributed across each pore on the surface. These results demonstrate that the negative pressure applied at micro-openings on the solid surface was significantly uniform, providing in silico theoretical support for subsequent experiments.

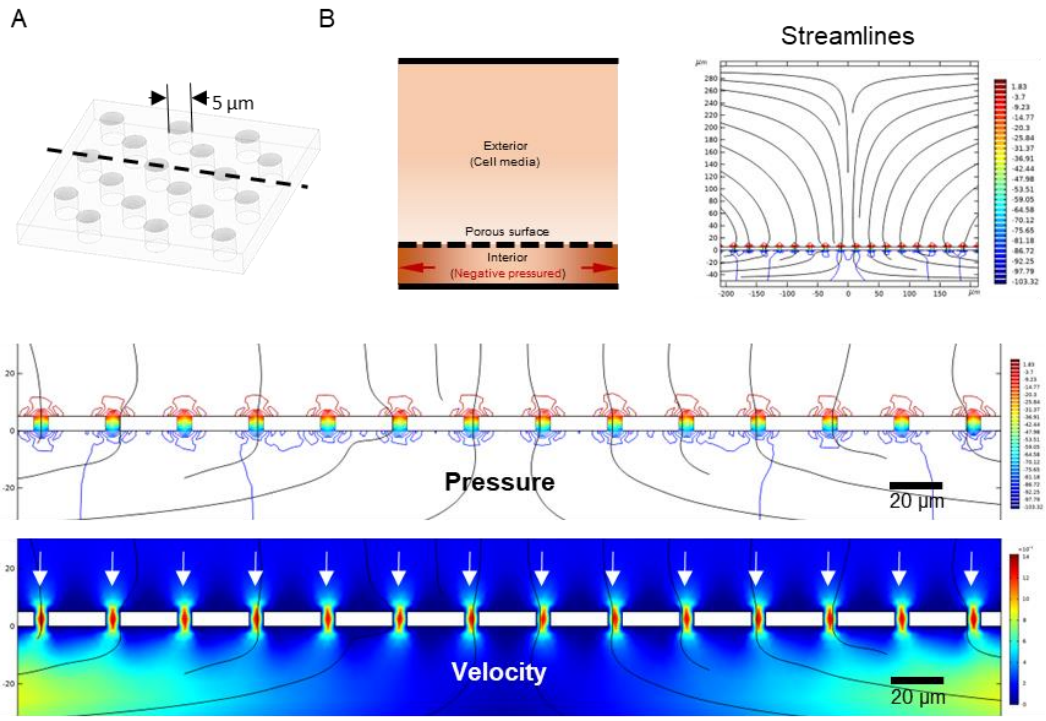

Figure 2.12 COMSOL simulation for the pressure-driven flow model.
(A) The 2D model was converted from the 3D model with a porous surface containing 5 µm holes. (B) The porous surface defines the top region containing culture media and the bottom region representing the internal channels of the scaffold. The micron-size holes on the surface demonstrate their capability to evenly distribute the negative pressure applied to the internal channel.

Next, we developed a representative 3D model to verify the result from simulation. This system comprised two major components: (i) a 3D-printed microfluidic substrate for fluidic control, and (ii) 3D-printed porous scaffolds for cell attachment. As depicted in **Figure 2.13A**, integrated circuit packaging offers an interface that facilitates user connection and access to the micro-level pins on the die via bonding wires and leadframes with manageable sizes. Akin to advanced integrated circuit packaging, the 3D-printed substrate functioned as an interface, providing anchoring spots for the porous scaffold and enabling fluidic transport between the scaffolds and fluid control

modules. Our substrate (25 mm × 25 mm), meanwhile, featured a primary fluidic channel for pump connection, while a secondary fluidic channel connected to the Nanoscribe-printed scaffold above. The substrate included six individual openings at the top, each with a diameter of 150 μm (Figure 2.13B). As depicted in **Figure 2.13C**, we developed a scaffold containing three University of Maryland "M"s. There were 295 pores (5 μm in diameter) on each side of one M structure. The six inlets/outlets at the bottom of the scaffolds aligned with the six openings on the substrate, when connected, the hollow internal channels in the scaffold allowed a rapid pressure delivery to the system. Following the previous printing protocols, we employed Nanoscribe with IP-S resin to generate the porous scaffolds while using a DLP-based printer with clear microfluidic resin to fabricate the substrate. The SEM image also verified the successful construction of this scaffold on the substrate.

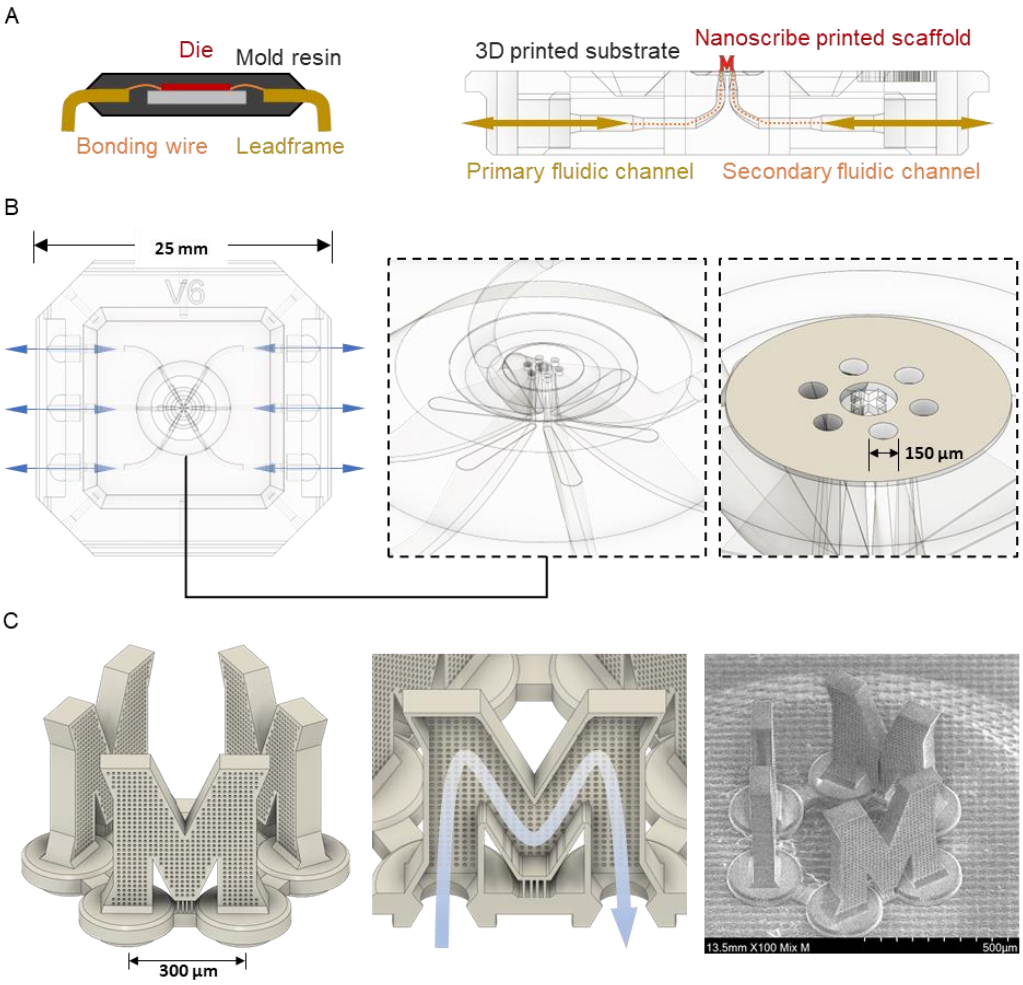

Figure 2.13 Development of the microfluidic substrate and micro-scaffolds.

(A) The microfluidic substrate works as an interface between the critical functional feature (Nanoscribe printed scaffolds) and the fluidic control systems. (B) The microfluidic substrate contains 6 openings which can be individually controlled. These openings can specifically be aligned with the fluidic inlets and outlets on the scaffolds. (C) The scaffold containing three University of Maryland “M”s.

2.3.3.2 Verification of the fluidic control via standard fluorescent particles

We hypothesized that using a conventional pump system with a constant flow rate would lead to dynamic changes in the pressure gradient at each opening during the alignment process, depending on the total cross-sectional area provided. Consequently, the pressure or force exerted on particles or cells would increase as pores became progressively blocked, potentially causing irreversible cell damage or forcing cells to be extruded through the micropores when a certain pressure threshold was reached. To address this issue, we implemented a fluidic transport system with a pressure control feedback module that maintained constant pressure. Thus, the pressure gradient at each pore remained consistent from the beginning to the end of the alignment process.

In the initial study, we demonstrated standard elements and an image-based method to visualize and verify the process guiding particles toward the surface of the printed scaffold. To do that, we employed green fluorescent polystyrene microspheres (5 μm in diameter, 1.05g/cm^3, Ex: 468 nm/ Em: 508 nm) as an indicator for both the flow pattern and the pore size on the scaffold. Specifically, we prepared 0.01% of the particles in 0.01% of Tween-20 PBS solution which represented the media containing epithelial cells and fully immersed the printed scaffolds into the solution. A negative pressure of -20 mbar was applied to the fluidic system, initiating liquid movement towards the internal channels of the scaffold through the patterned micro-openings on the surface. We recorded the particle alignment process using a fluorescence microscope. As demonstrated in **Figure 2.14A**, we observed significant particle movement towards the micropores on the scaffold surface as expected. Upon reaching the pores, particles were stopped and constrained by the scaffold due to the

intentionally designed pore size. This result verified the uniformity of pore size across all printed openings, as particles were effectively supported without passing through the openings.

Due to a constant pressure applied to the internal channel, the suction force applied on the particles remains consistent regardless of the percentage of the opening remaining on the scaffold. Importantly, this process is governed by the pressure gradient between the internal channel and the external environment, offering a controllable cell alignment method that could be finely tuned depending on cell type or material mechanical properties. In subsequent experiments, we employed higher negative pressure, anticipating increased flow rates and more rapid cell assembly. As shown in **Figure 2.14B**, significant particle movement towards the scaffolds and accelerated particle assembly were observed. Importantly, the pattern of particle location was unrecognizable, indicating uniform pressure distribution across all micropores. Overall, utilizing a pressure of -20 mbar for particle immobilization yielded the following results: within 10 seconds, particles occupied 8.5% of the available sites. Subsequently, coverage increased to 17.3%, 28.7%, 32.9%, 44.3%, 58.1%, and 52.5% after 20, 30, 40, 50, 60, and 70 seconds, respectively. Generally, it took only 1 minute to cover approximately half of the available surface area under these conditions. Meanwhile, utilizing a pressure of -50 mbar for particle immobilization yielded the following results: within 10 seconds, particles occupied 14.0% of the available sites. Subsequently, coverage increased to 47.7%, 72.3%, 78.9%, 83.8%, 86.9%, and 91.5% after 20, 30, 40, 50, 60, and 70 seconds, respectively. Generally, approximately three-quarters of the available surface area can be covered within 30 seconds under these

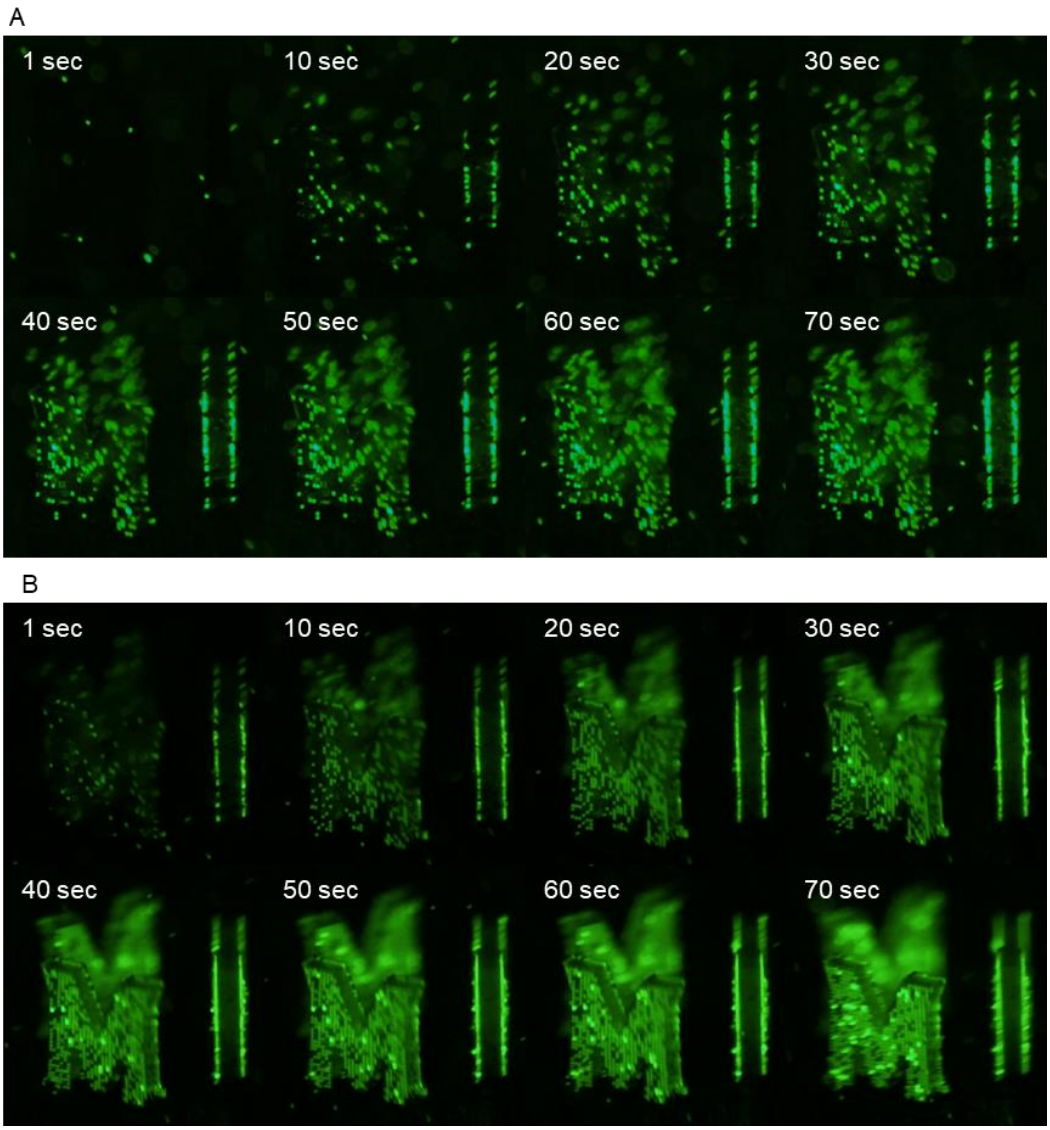

Figure 2.14 Pressure-driven rapid particle assembly.
(A) A negative pressure of -20 mbar was applied to the fluidic system and the movements and locations of particles with green fluorescence was captured with microscope. (B) A negative pressure of -50 mbar was applied to the fluidic system, which significantly facilitated the particle attachment to the surface of the scaffolds.

conditions (**Figure 2.15**). Technically, without the application of vacuum, particle attachment to the scaffold can be extremely limited. This limitation arises from the absence of traction and the reliance on natural settlement through gravity. Potentially,

if the particle was replaced with cells, the cell assembly time can be significantly reduced from 14 days to less than 1 hour.

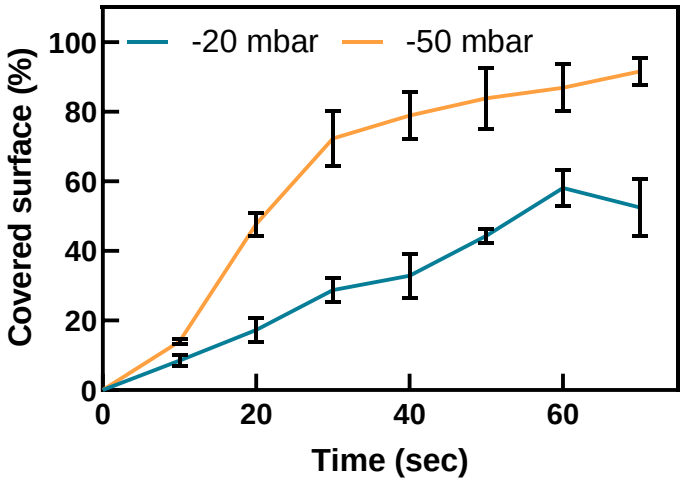

Figure 2.15 Enhancement of surface coverage efficiency through increased pressure. The results demonstrate the particle attachment efficiency was highly correlated with the pressure level applied to the system resulting in a higher surface coverage. *(n = 4)

To gather more information for subsequent cell operations and assess the reversibility of attachment created via suction, we demonstrated that particles on the scaffold could be gently released through pressure manipulation. Specifically, we applied a negative pressure of -20 mbar to the fluidic system for 90 seconds, then released the pressure back to 0 mbar for 5 seconds and monitored particle movements in the solution. As shown in **Figure 2.16**, particles adhering to the scaffold due to the applied negative pressure were observed to instantly detach from the surface upon suction removal, indicating that the attachment was primarily driven by the pressure gradient and that the process is reversible. This result suggests that the force generated on the particles is manageable and potentially suitable for cell alignment applications.

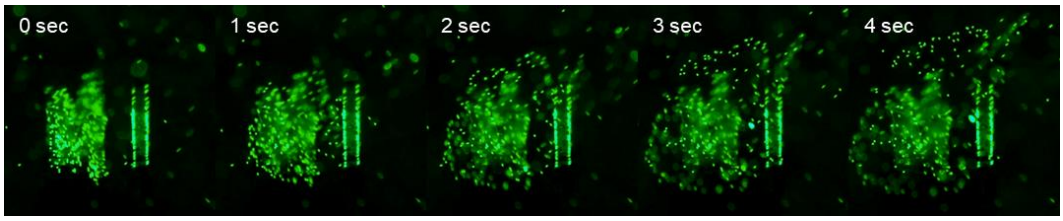

Figure 2.16 Particle release via pressure manipulation.
The particles were attached to the scaffolds due to the negative pressure applied on the pores. Immediate particle detachment was monitored upon the pressure gradient removal.

2.4 Conclusion

In this study, we aimed to assess the potential of additive manufacturing for creating three-dimensional support structures as scaffolds in the in vitro reconstruction of gut epithelium. We primarily explored this topic using two distinct approaches: (i) employing digital light processing (DLP) additive manufacturing to rapidly fabricate scaffolds with desired 3D geometries within a manageable time frame, and (ii) utilizing two-photon direct laser writing (DLW) 3D printing to generate an emulated villus with uniform surface porosity and an internal capillary system. These features facilitate molecular transport along the apical-basolateral axis and from the capillary through the villus and into the luminal regions, respectively.

First, we defined the dimensions of a single villus to be 200 µm in diameter and 1000 µm in height, based on the size of actual human villi. We then 3D printed scaffolds containing 800 of these support structures on an area that fitted the wells of a 24 well plate. Caco-2 cells were chosen and seeded onto the scaffold to validate critical parameters such as cell numbers, viability, and tight junction formation. Comparable

to the cell growth rate previously reported using PLGA-based casted scaffolds, our 3D printed geometries employing clear microfluidic resin provided adequate support and adhesion for Caco-2 cell proliferation, with overall cell viability exceeding 95% after 14 days of culture. As anticipated, cell numbers correlated with surface area in both 2D and 3D environments, suggesting that cells on the 3D support material formed a cellular monolayer. Notably, we observed cell folding phenomena in cells grown on 2D surfaces printed with the same photosolidifying resin, which contributed to increased confluency after 21 days. Further experiments indicated minimal differences in Caco-2 cell viability on bare or growth matrix-coated scaffolds, suggesting the potential for this material to be directly utilized for constructing scaffolds for other human cells following a proper cleaning process. Immunostaining targeting the ZO-1 tight junction protein revealed that proliferated Caco-2 cells exhibited the desired tight junction formation after 21 days of culture. Overall, we demonstrated the feasibility of using 3D printing for the rapid development of scaffolds comprising complex 3D geometries in organ-on-a-chip applications.

Next, we have constructed an artificial full-size intestinal villus using an advanced two-photon DLW 3D printing system. This system accurately recapitulates the 3D gut villus geometric landscape and offers advantages in (i) sampling from a single villus while avoiding sample mixing commonly found in conventional 2D models; (ii) eliminating uneven diffusion patterns due to the thin fluid channels beneath the scaffold. However, because of the differences in size scale, printing the villus and the housing simultaneously becomes limited. Therefore, we developed a methodology to "stitch" together delicate 3D printed segments with the cast housing. We aligned and assembled

these segments to ensure continuous flow of basolateral fluid through the system. Owing to the transparency of the 3D printing material (IP-S), the model villus can be repeatedly visualized during cell growth. With further experimentation, we believe that designing a series of separate flow channels specifically targeting and collecting samples from designated areas could provide location-related information on the crypt-villus axis. The information obtained from the villus microenvironment is critical for understanding the interaction of gut cells with certain localized intestinal pathogens. This understanding will facilitate rapid comprehension of disease progression and, at the same time, promote the development of new therapies.

Finally, we exhibited the pressure regulated cell assembly. The cell settling due to gravity significantly limited the cell assembly along the vertical direction on 3D scaffolds. Typically, the formation of meaningful morphologies relies on the self-proliferation and migration of the cells which sometimes makes it difficult to align with experimental progressions. Here, we reported that, with a negative pressure applied to the internal space of a porous 3D printed scaffold, the facilitated pressure-driven flow could serve as the force guiding the cells to designated positions. The forces are also reversible, and highly manipulatable via pressure regulation. From its humble beginnings as a prototyping tool, additive manufacturing has grown into a technology with the potential to revolutionize industries and redefine how we create, design, and manufacture. As 3D printing continues to evolve, we envision it to enable more transformative impact on the synthetic models.

Chapter 3

3D printed microfluidic device for rapid interrogation of antibody titer and glycosylation

3.1 Introduction

Part of the information relating to antibody titer and glycosylation in the first paragraph was provided by Dr. Dana Motabar.

Over the past few decades, the recombinant antibody therapeutics market has experienced rapid growth, becoming a significant sector of the biopharmaceutical market. Antibody therapeutics have achieved considerable success in various critical therapeutic areas, including cancer, infection, and inflammation, due to their high specificity and selectivity[72–74]. Unlike small molecule pharmaceuticals, which are chemically synthesized, recombinant antibody therapeutics are larger, more complex molecules produced in mammalian cells. Consequently, the biopharmaceutical development process for antibody therapeutics is both costly and time-consuming, given the complexities associated with optimizing host cell lines, bioreactors, processing conditions, and post-synthesis product characterization[75–77]. On average, a biologic takes 10 years and 2.6 billion dollars from initial discovery to market release[78]. Reducing the cost and time required to develop and manufacture antibody therapeutics remains a significant challenge for the biopharmaceutical industry. However, it is necessary to generate safe and effective therapeutics that can reach a broader patient population. An essential aspect of the antibody development process involves monitoring and characterizing critical quality attributes (CQAs), such as N-linked

glycosylation and titer. Titer, referring to the concentration of antibody per liter of cell culture broth, is generally considered a critical process parameter for characterizing upstream efficiency[79]. Traditionally, offline affinity high-performance liquid chromatography (HPLC) is employed to characterize titer[80]. N-linked glycosylation involves the covalent attachment of carbohydrate groups to the asparagine-297 (Asn-297) residue on the CH2 domain of the Fc portion of the antibody. N-glycosylation features a biantennary type with a core structure composed of two N-acetylglucosamine (GlcNAc) groups linked to three mannose groups. Other glycan groups, such as galactose, sialic acid, and fucose, can modify the core glycan structure[81]. N-glycosylation is defined as a CQA, as studies have demonstrated that the distribution of glycoforms on the Fc region can significantly impact the antibody's stability, in-vivo half-life, efficacy, and immunogenicity[82–84]. Current gold-standard methods to characterize glycosylation include complex, offline techniques that involve enzymatic removal of glycans from the antibody, followed by quantification using liquid chromatography, mass spectrometry, or capillary electrophoresis[85,86].

Microfluidic platforms, in recent years, have been widely used in the scientific and biomedical fields. Taking advantage of high selectivity and precise enzyme-substrate affinities, enzyme-based microfluidic biosensors are known to provide rapid and accurate analysis within an automated manner. Microfluidic sensors are manufactured via standardized fabrication processes which enable rapid development for commercialization. This makes them a potentially powerful tool for providing rapid and robust data for quality control and process development in biomedical and biopharmaceutical manufacturing. That is, while the path toward sensor

commercialization is available, their assembly can be complex and their use can involve many affiliated components such as pumps, valves, sensing elements, etc.

We have previously shown how one can create an electrochemical sensor that is assembled in a series of steps where the only inputs (in addition to reagents and buffer solutions) are applied voltage. That is, we first created a sensing interface that is ideally suited for sensing antibodies contained in a variety of solutions[42], then we used the interface within a 3D printed microfluidic housing that is easily designed and fabricated. In the sections below, we describe this sensor, its design, fabrication and use. The electroassembled thiolated PEG-based sensor (i) captures mAbs based on their Fc region and binding affinity to protein G, enabling assessment of antibody titer, and (ii) secondarily, captures mAbs based on their glycan pattern and binding affinity to lectins[42]. Unlike most traditional analytical chemistry methods, our interfaces combine electrochemistry with biological molecular recognition elements. In our previous report [42], the interfaces were established on commercially acquired gold working electrodes and the assembly methodology while simple, still relied on manual, step-by-step interface construction, sample preparation, and finally, sample measurement. Because of the added steps, manual labor, sampling and washing protocols, operational errors were at times, unavoidable.

Instead, to offer rapid, robust, and especially high-throughput approaches for biopharmaceutical process monitoring and control purposes, we built an integrated automated platform based on the existing batch methodology. That is, while traditional microfabrication techniques such as photolithography demand complex and time-

consuming assembly and bonding processes, additive manufacturing allows direct conversion of CAD models into precise geometric 3D hardware. This is accomplished via layer-by-layer printing, 3D-printing, a suite of technologies that has revolutionized the creation and realization of design concepts and their engineering, and enabled rapid development of microfluidic devices for bioanalytical and biomedical applications, such as colorimetric diagnostic assays[87,88], nanomedicine[89], and biopharmaceuticals[90,91].

Here, we have carefully analyzed our previously published protocol[42] using a thiolated 4-arm polyethylene glycol (PEG) that is electroassembled onto a gold sensing surface. This is represented in the **Scheme 3.1** below. The oxidation of thiolated PEG facilitates the construction of interfaces, enabled by the redox cycling of the mediator Fc and the "activation" of sulfhydrl groups on the PEG or other molecular species. The first step is the creation of the hydrogel film by applying an oxidizing voltage to an electrode immersed in a solution of the thiolated PEG and redox mediator 1,1'-Ferrocenedimethanol (Fc)[36]. Then, we further "activate" sulfhydryl groups remaining on the hydrogel film into reactive sulfenic acid groups (SOH as indicated). The recognition elements can now spontaneously form disulfide linkages with the hydrogel upon incubation, providing selective capture of analytes. For the titer detection interface, a novel cysteine-tagged protein G serves as the detection element. Protein G was chosen for titer detection interface because it enables the capture of IgG by binding to the Fc portion of the antibody[92,93]. For the glycan analysis, a galactosylation detection interface is created using a galactose-recognizing lectin, *Ricinus communis agglutinin I* (RCA120), as the detection element. RCA120 allows selective capture of

antibodies with terminal β-galactose (Galβ) glycans based on traditional lectin-glycan binding[94,95]. Importantly, it is bivalent, meaning it can bind to a galactose covalently attached to the PEG as well as a galactose on the subsquently captured antibody. That is, in the previous work, a thiolated galactose was first conjugated to the PEG hydrogel using the Fc-based activation of the PEG thiols, exactly analogously as the assembly of the PEG. This places a galactose on the surface for subsequent assembly of the bivalent lectin. In turn, the lectin serves to capture the antibody in a sample solution. When the sandwich structure is formed after subsequent incubation with the reporter (protein G:HRP), the electrochemical outputs arising from the electron transfer mechanism between HRP, mediator Fc, and hydrogen peroxide H_2O_2 represent the analyte content on the interface.

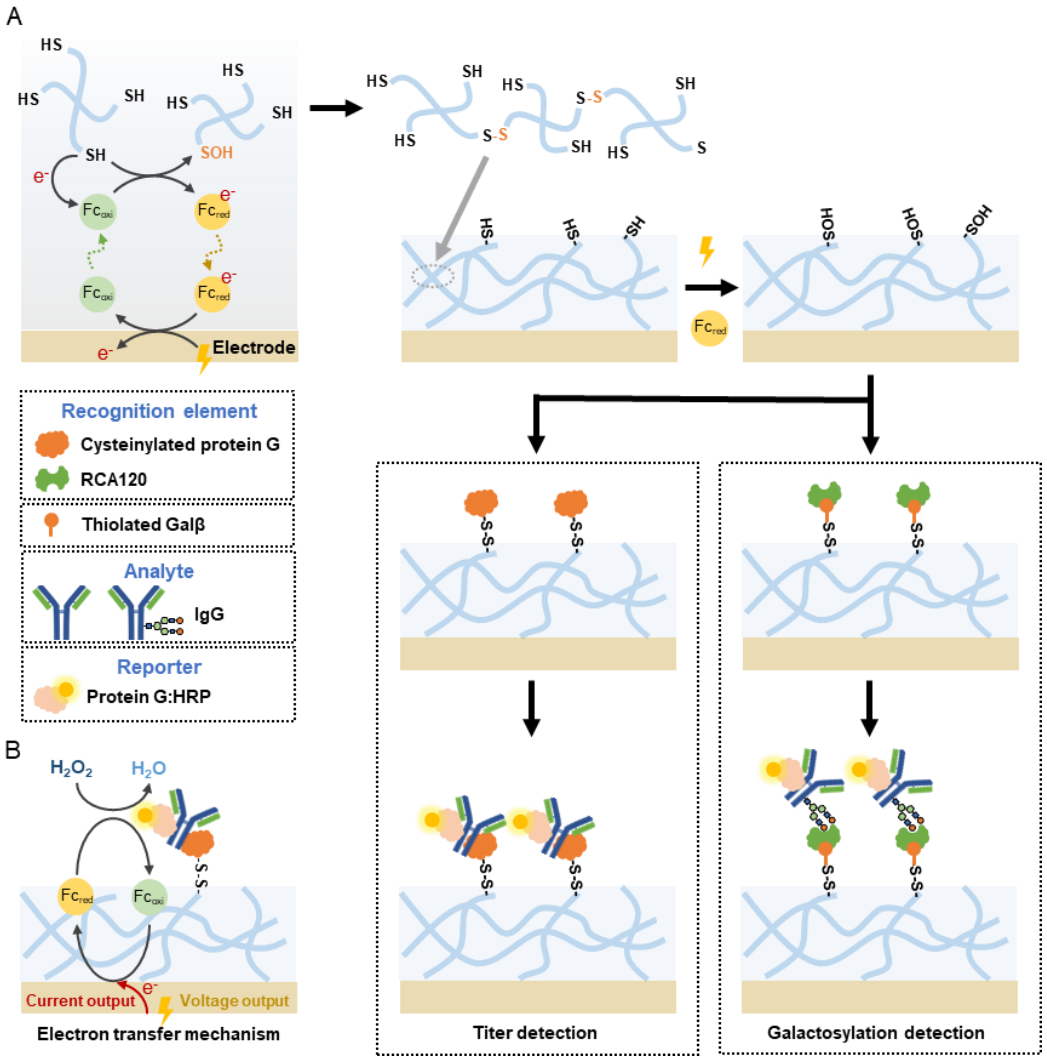

Scheme 3.1 Electrobiofabrication, functionalization, and sample detection of PEG sensor interface.

(A) The electroassembly of interfaces is based on the oxidation of thiolated PEG and subsequent conjugation with the recognition elements. (B) The HRP converts the hydrogen peroxide into water and oxidizes mediator Fc. The redox cycling process between the Fc and the electrode generates the electrochemical outputs that represent the analyte content on the interface.

To create a device that is more rapidly assembled, easier to use, provides replicate measurements in even shorter times, and that ultimately targets deployment in process

development groups or even manufacturing suites, we analyzed each component and process step of the above sensing system and asked the questions: “Is this needed?” and “Can we simplify this?”. A 3D-printed microfluidic device that enables the high-throughput rapid analysis of antibody titer and glycosylation, would be transformative as it could provide real time product measurement (both quantity and quality) which in turn, could be used for on-line optimal process control. For example, one of the first issues discussed was the gold sensing surface. It is well known that thiols adhere to gold. Further, while gold is certainly conductive, there are other substrates that should allow for electroassembly, but that might minimize fouling and maximize electron transfer. We decided to build devices that utilize indium tin oxide (ITO) coated glass as the working electrode onto which we establish the sensor interfaces. ITO has excellent electron transfer qualities and is optically clear so that we can also use fluorescence or image analysis should they be desired. As depicted previously in **Scheme 3.1**, the interfaces employ a thiolated PEG hydrogel and the recognition elements that enable selective capturing of target analytes. To integrate the system into the microfluidic device, steps including gel formation, interface functionalization, and rinsing process were investigated and optimized. Notably, we combined the PEG formation with the interface functionalization steps into one by preparing the deposition solution containing thiolated PEG, Fc, and the recognition elements (**Scheme 3.2**). The disulfide linkages between thiolated PEG monomers and recognition elements can spontaneously form with the hydrogel upon electrodeposition. We then demonstrated that the incubation time for the analyte capturing and protein G:HRP conjugation can be reduced to 30 minutes (50% drop). We also built the system so that 8 simultaneous

measurements were possible, this could include 4 of a sample and 4 of a control, or any combination thereof. As a result, the multichannel 3D-printed device reduces complexity, provides more data, and addresses an unmet need for implementation and operation in the biopharmaceutical industry.

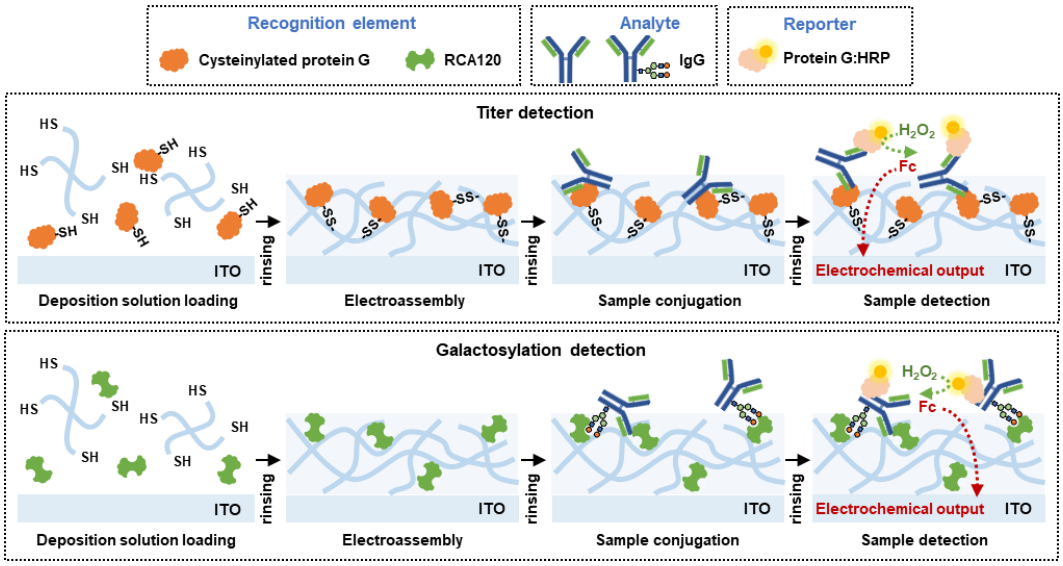

Scheme 3.2 Single-step functionalization via recognition element codeposition.

The simplified interface formation is mainly contributed by the codeposition of the recognition elements with thiolated PEG monomers and the shortened incubation time for analytes and reporter proteins.

3.2 Materials and Methods

Materials

Indium tin oxide coated glass slide, square (surface resistivity 8-12 Ω/sq), RCA120 and fluorescein labelled conjugate (FITC RCA120) were purchased from Vector Laboratories (Burlingame, CA). IgG from human serum, SILU Lite SigmaMAb, and protein G:HRP conjugate and phosphate buffered saline (PBS, pH 7.4) were purchased

from Sigma-Aldrich (St. Louis, MO). Clear 3D microfluidics printing resin was purchased from CADworks3D (Toronto, Canada). 1,1′-Ferrocenedimethanol (Fc) was purchased from Santa Cruz Biotechnology (Dallas, TX). A 1 M stock solution of Fc was prepared in DMSO, and dilutions were prepared in PBS freshly for each experiment. Dulbecco's Modified Eagle medium, high glucose, HEPES, no phenol red (DMEM) was purchased from Thermo Fisher Scientific (Waltham, MA).

Device fabrication and performance assessment

The 3D printed 8-channel microfluidics device with ITO electrodes was designed based on a standard 3-electrode system including a device with 25 mm × 25 mm ITO working electrode (split into 8 sub working electrodes), and an electrical connector that allows wiring to the electrochemical analyzer. A Pt wire that serves as the counter electrode and an Ag/AgCl reference electrode that connect to the device via fluidic connector. (i) To make the 3D printed device housing, designs were created using Autodesk® Fusion 360 and Autodesk® Inventor (Autodesk, Inc, US). The CAD files were then converted to writing-path using the Chitubox 1.9.4 (Guangdong, China). Mars 3 Pro was used to fabricate the housing. When the printing process was completed, the substrate was placed in a bath of methanol with gentle shaking by hand for 1 minute and then dried with nitrogen. This step was repeated three times to thoroughly remove any uncured residues. The prints were then further cured under a 20-Watt UV lamp for 10 seconds followed by a 30-second rest at room temperature. This step was repeated three times to achieve full strength. Purchased precut ITO glass (25 mm × 25 mm) was patterned with CO_2 laser engraver to physically define all electrodes and the connecting region. The cured housing was then aligned with the laser patterned ITO glass and annealed

together with the same photosensitive resin used for printing. (ii) The design and the fabrication of the electrical connector generally followed the same protocol described above. Two 4-way spring connectors (Digi-Key, Part Number 478-4688-6-ND) were then attached to the designed location on the printed electrical connector in which later enabled the physical connection to the ITO device. The other end of the 4-way spring connectors were then soldered with wires which connect to the electrochemistry analyzer. (iii) The fluidic connector was made with a T-shape 3-way connecter. The tubing was glued to the connector with epoxy resins.

For the simulation model: The numerical (finite element method) simulations for infusion-diffusion model was performed using the Laminar Flow module of commercially available COMSOL Multiphysics software (version 5.6). Geometry and fluidic setup were defined based on the dimensions and parameters provided previously. The fluidic conditions were described by Navier-Stokes equations.

For the fluidic test: Two test solution were prepared: 100 mM phosphate buffer (PB) solution (negative) and a 100 mM PB solution containing 100 μM of 1,1′-Ferrocenedimethanol (Fc) (positive). They were connected to the port No.1 and the port No.3 of the 2-way 4-port valve and a flow rate of 1 mL/min and the valve determined the fluid infusion. Each test solution flowed into the microfluidic device for 60 seconds as one independent cycle and the process repeated five times. Meanwhile, an oxidative potential of 0.4V was applied to all working electrodes and measured the currents. The current data from the last 30 seconds of each period was collected and averaged for

analysis. Followed the same protocol, solution with varying Fc concentrations (5, 10, 25, and 100 μM) was tested.

Titer and galactosylation detection interface measurements

Measurements of the current response from the interfaces were performed with the 3-electrode set-up (same as above) using a CHI1040C electrochemical analyzer (CH Instruments). For construction of titer interfaces on the microfluidic device, a solution of Fc (25 mM), PEG thiol (50 mg/mL) and C-terminus cysteine tagged protein G (250 μg/mL in 0.1 M PB, pH 7.4[96]) was prepared and injected (100 μL) into the microfluidic device (using the device injection port). Interface electrodeposition occurred for 1 minute at a constant oxidative potential of 0.8 V. After electrodeposition, the peristaltic pump system was activated and channels were rinsed with wash buffer (PBS, 0.05% Tween-20, pH 7.4) for 10 minutes at a flow rate of 0.5 mL/min (10 RPM coupled with black-black PVC tubing purchased from Gilson). The devices were then sequentially incubated in serially diluted concentrations of IgG (0-1000 mg/L) and protein G:HRP (100 mg/L), respectively, at room temperature for 30 minutes. After each respective incubation (IgG and protein G:HRP), the channels were rinsed with wash buffer for 10 minutes at a flow rate of 0.5 mL/min. Current measurements were then performed using constant potential amperometry. Specifically, the devices were run under an applied potential of 0 V and Fc (0.5 mM) was pumped at a flow rate of 1 mL/min (20 RPM coupled with black-black PVC tubing purchased from Gilson) until a constant baseline was achieved. To generate a current response, the infused liquid sample was then switched to a solution of Fc (0.5 mM) and H_2O_2 (100 μM) and the response from baseline was recorded. The lower limit of detection for the titer detection interface was calculated as

previously described. For construction of galactosylation interfaces on the microfluidic device, the C-terminus cysteine tagged protein G in the deposition solution was replaced with RCA120 (0.5 mg/mL in 0.1 M PBS, pH 7.4).

Evaluation with culture media

Titer and galactosylation detection interfaces were assembled as described previously. Titer detection interfaces were incubated in IgG from human serum (0 – 1000 mg/L) that had been diluted with 0.1 M PBS or with DMEM. Galactosylation detection interfaces were incubated in SigmaMAb (1 g/L) diluted with 0.1 M PBS or with DMEM. We chose to use this antibody standard as it has a known concentration of galactosylated IgG. Interfaces were then incubated in protein G:HRP (100 mg/L). All incubations occurred at room temperature for 30 minutes. Between incubations, interfaces were rinsed with wash buffer at the flow rate of 0.5 mL/min. Current measurements were taken as described above.

Interface regeneration studies

One aspect of the value proposition for a sensor of this type is its potential for reuse. We decided to test whether the surfaces could be stripped of mAb and the reporter, HRP, and then subsequently reused. To evaluate regeneration, the detection interfaces were assembled with IgG from human serum (1000 mg/L) and protein G:HRP (100 mg/L) and measurements of the current response were taken using the same conditions as above. The interfaces were then washed with 0.1 M acetic acid, 1 M sodium chloride, pH 2.8 at the flow rate of 0.5 mL/min in order to decouple IgG and protein G:HRP from the recognition elements on the surfaces, leaving only the capturing proteins (i.e.,

protein G) covalently bind to PEG. Current measurements were taken to confirm that IgG and protein G:HRP were removed. The interfaces were once again re-assembled with IgG and protein G:HRP. Current measurements were taken to confirm the re-binding of IgG and protein G:HRP to the interface surfaces.

3.3 Results and discussion

3.3.1 System and device design, and fabrication

In this study, we developed a 3D printed microfluidic device consisting of an ITO-based electronic sensor interface (**Figure 3.1A**) for high-throughput and automated interrogation of antibody titer and glycosylation. The system utilizes a conventional 3-electrode setup with a shared reference and counter electrode and eight ITO working electrodes, creating a stable environment for the previously developed electroassembled thiolated PEG-based sensor interfaces. The microfluidic chip comprises two main components fabricated separately: (i) a 3D printed housing and (ii) transparent ITO bottom electrodes. We selected ITO as the working electrode (denoted "WE") due to its favorable conductivity relative to gold and other substrates, as well as its compatibility with optical signals (i.e., transparency).

As shown in **Figure 3.1A**, the 3D-printed housing consists of eight individual fluidic channels that are printed for parallel use. They have openings (marked in red in the figure) at the bottom, as well as sample inlets and outlets on the side of the device. The symmetric splitting of fluidic pathways enables an even distribution of the samples introduced into the eight chambers for subsequent measurement. After aligning the chambers with the ITO glass chip (laser engraved into eight parallel sub electrodes in

advance), we annealed the 3D printed housing to the electrodes by applying the same 3D printing resin at the boundary of two material and exposing UV for 10 seconds, thus sealing the openings of the fluidic chambers to prevent leakage and generating eight parallel fluidic interfaces for electrochemical application. We note that the dimensions of the channels define the functional area of the bottom ITO working electrode (l × w × h: 13 mm × 1.5 mm × 200 µm, area: 27.924 mm2) onto which the sensor elements are assembled.

To complete the 3-electrode setup, we designed another separate fluidic connector for the reference and counter electrodes. The fluidic connector contains five openings which, from left to right, are assigned as the counter electrode, potassium chloride solution, reference electrode, fluid outlet, and fluid inlet (right panel of Figure 3.1A). A 1M KCl solution filled in the fluidic connector enables ionic transport and conduction for electrochemical reactions while ensuring fluidic connection for the immersed counter and reference electrodes. Fresh KCl solution was fed to the fluidic connector at a flow rate of 200 µL/min. This flow minimizes mixing with the liquid samples introduced from the fluid inlet. The liquid sample from the microfluidic device enters the fluidic connector via the fluid inlet and encounters the KCl solution entering from the left. The two fluidic flows intertwine at the junction on the right side of the fluidic connector and exit the system together from the fluid outlet. Consequently, we have established a complete fluidic pathway starting from the sample inlet on the microfluidic chip and ending at the fluid outlet on the fluidic connector.

Next, we designed and fabricated an electrical connector to enable the electrochemical capabilities of the microfluidic device (**Figure 3.1B**). This electronics system allows for the interface assembly as well as the subsequent sensing via HRP and added hydrogen peroxide. We designed this connector so that it is easily employed, utilizing a sort of “snap-in” configuration. This avoids the more common alligator clip designs that are less well connected and easily moved/disconnected at the wrong times. Here, our design features two 4-way spring connectors, providing a total of eight connection points for parallel data transfer with the eight test channels already assembled and fused. The connector serves as an interface, linking the ITO device to the electrochemical analyzer. In conjunction with the fluidic connector, the working electrodes, counter electrode, and reference electrode form a complete circuit for electrochemical reactions. Moreover, our design features a “plug-and-play” modularity for the 3D printed microfluidic systems. The ITO teeth of the microfluidic device can be inserted into the slot on the connector, establishing an instant connection via spring metal pins. This "plug-and-play" design enables rapid device replacement and module switching, ultimately facilitating high-throughput, multi-sample detection with ease. The steps for the ITO device fabrication and assembly are illustrated in **Figure 3.1C**.

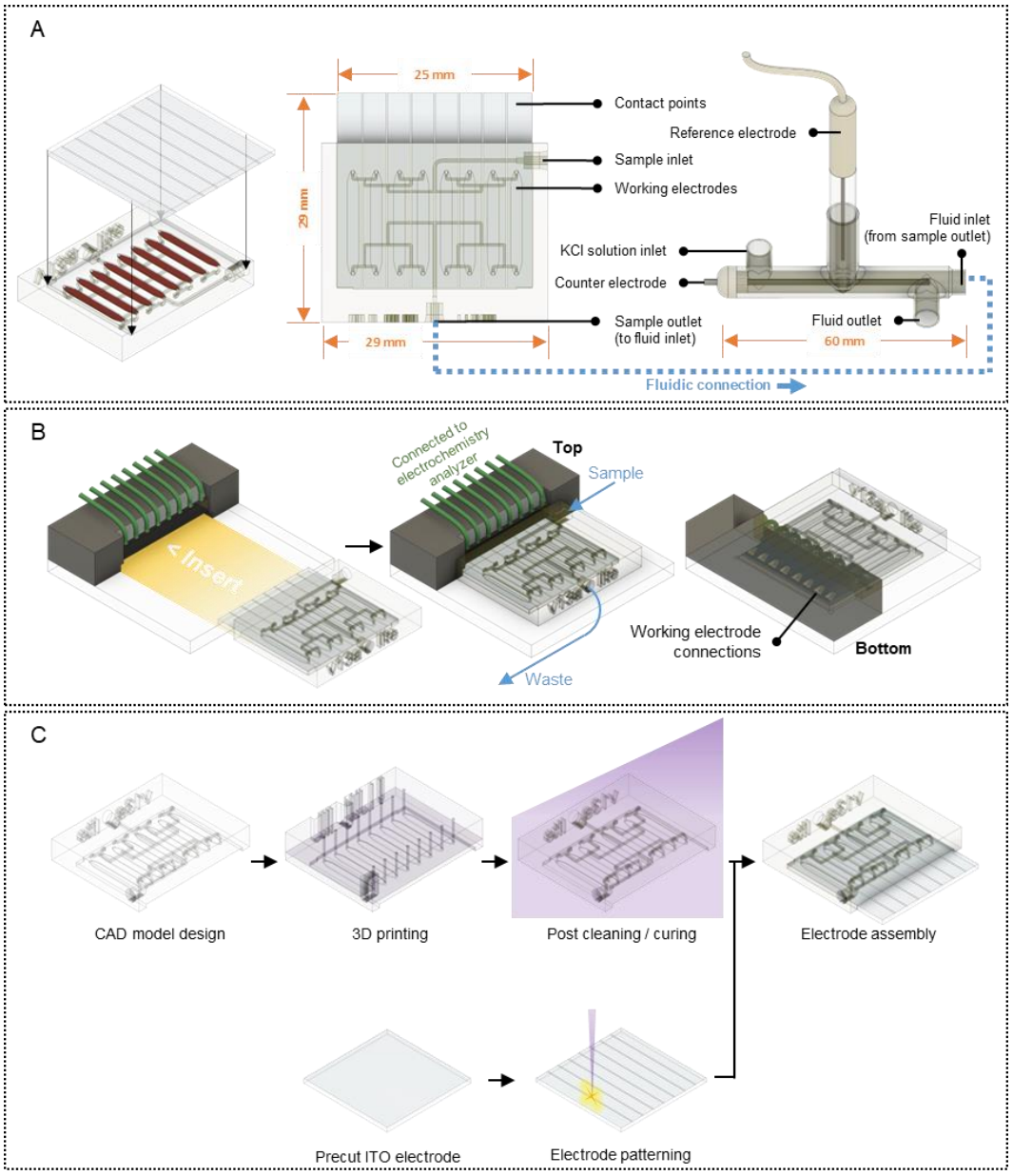

Figure 3.1 ITO microfluidic device and connectors.

(A) The 8 parallel stripe ITO electrodes on the glass substrate align with the 8 channels on the 3D printed device. When bonded together, they together form 8 individual electrochemistry ready channels for the sensor interface fabrication. The fluidic connector comprises the reference electrode and counter electrode and fluidically connects the microfluidic module which enables the ionic transport for the chemical reaction. (B) The electrical connector provides a "plug-and-play" modularity for the 3D printed microfluidic systems and makes it straightforward when the users need to

quickly switch between function modules. (C) All the devices are highly customizable and can be rapidly fabricated using 3D printing. On average, it takes only 10 minutes to make one device.

To enable uniform, simple and precise sample operation, we designed an affiliated fluidic system that utilized an automated valve and pump system. This facilitates fluid control. As depicted in **Figure 3.2A**, the system consists of three automated valves and one peristaltic pump for managing the 11 steps (**Table 3.1**) required for sensor interface fabrication and sample detection (valve and flow diagrams are shown in **Supplementary Figure S3.1**). The first valve (valve A) is a 6-port selection valve, controlling the reagents (ethanol, water, 100 mM potassium, 0.05% Tween-20 in 100 mM potassium phosphate buffer, and 0.5 mM Fc in 100 mM potassium). The second valve (valve B) is a 2-way 6-port valve that regulates the infusion of the peroxide solution needed for sample detection when protein G:HRP conjugates with sample IgG. The third valve (valve C) is a 2-way 4-port valve and controls the sample injection for (i) deposition solution containing PEG gel with recognition elements, (ii) sample with IgG, and (iii) protein G:HRP. As demonstrated in the images in **Figure 3.2B**, the modular design of the system facilitates easy device switching, reagent replacement, and system maintenance.

Table 3.1 System function steps and valve positions

Step	Purpose	Valve position		
		A	B	C
1	System degassing process: Flush the fluidic system with ethanol at a flow rate of 2.5 mL/min for 1 minute.	1	1	1
2	Ethanol removal: Flush the fluidic system with purified water at a flow rate of 2.5 mL/min for 1 minute.	2	1	1
3	System conditioning: Flush the fluidic system with 100 mM PB at a flow rate of 2.5 mL/min for 1 minute.	3	1	1
4	Deposition solution loading and PEG interface deposition: Inject 100 µL of the deposition solution from the sample injection port at valve C.	4	1	2
5	Rinsing: Flush the fluidic system with wash buffer to remove deposition solution residue at a flow rate of 0.5 mL/min for 10 minutes.	4	1	1
6	Antibody sample injection and incubation: Inject 100 µL of the sample solution from the sample injection port at valve C incubate for 30 minutes.	4	1	2
7	Rinsing: Flush the fluidic system with wash buffer to remove sample residue at a flow rate of 0.5 mL/min for 10 minutes.	4	1	1
8	Protein G:HRP solution injection for antibody conjugation: Inject 100 µL of the Protein G:HRP solution from the sample injection port at valve C and incubate for 30 minutes.	4	1	2
9	Rinsing: Flush the fluidic system with wash buffer to remove protein G:HRP residue at a flow rate of 0.5 mL/min for 10 minutes.	4	1	1
10	Mediator Fc solution injection: Infuse the fluidic system with 0.5 mM of Fc solution at a flow rate of 1 mL/min for system background recording.	5	1	1
11	Reaction reagent (Fc + H_2O_2) injection: Infuse the fluidic system with 0.5 mM of Fc solution containing 100 µM of H_2O_2 at a flow rate of 1 mL/min for system for signal reading.	5	2	1

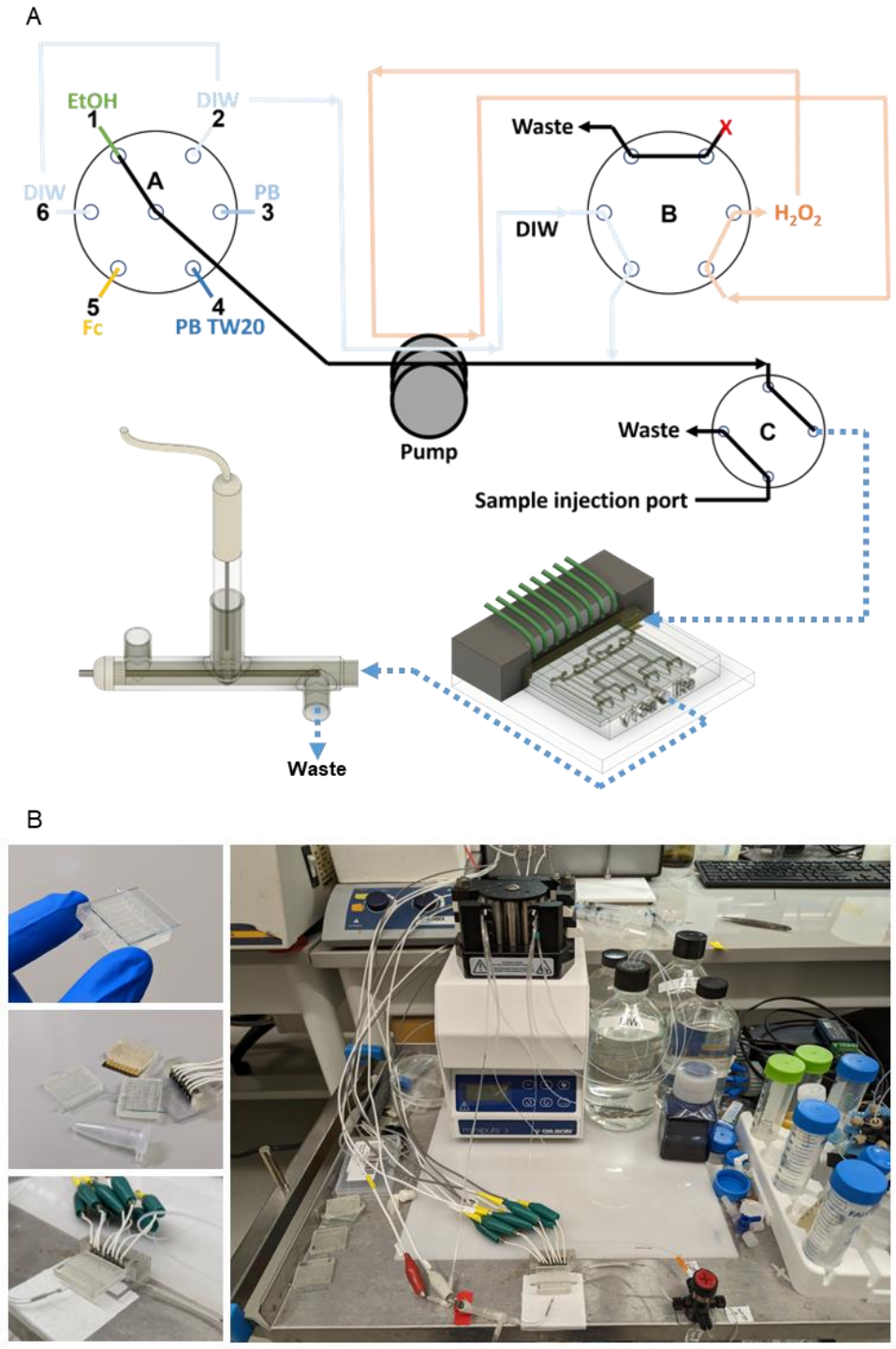

Figure 3.2 System design.

(A) The system features three automated valves and a pump to enable fluid control. Reagents or samples exit the associated system from the outlet on the right side of valve C and are then delivered to the microfluidic chip. (B) The device is assembled with a

3D-printed housing containing all fluidic channels and a patterned electrode chip featuring the desired conductive materials (e.g., gold or ITO). The device can be inserted into the electrical connector for easy connection to the pump system and electrochemical analyzer, allowing for automated operation.

3.3.2 Channel uniformity and fluidic performance

Fluidic uniformity and stability are likely channel dependent, and their quality further determines system robustness and measurement reproducibility. In initial studies, we utilized both a simulation tool and actual fluidic examinations (electrochemical measurement of Fc solution) to determine the flow uniformity and fluidic performance. Specifically, we developed a 3D model of the device, using the Laminar Flow module of commercially available COMSOL Multiphysics software for visualization and prediction of the fluidic patterns at various locations and flowrates within the microfluidic device (**Figure 3.3A**). Using these computational tools, we honed in on a flow rate of 1 mL/min for the sample flow (and assembly/wash flows) and due to its successes, we used this flow rate in all subsequent experiments. That is, our COMSOL model and predicted performances matched well our experimental results. As illustrated in the top panel of **Figure 3.3B**, our computational design uses symmetric splitting of the fluid in the channels and this was seen to evenly distribute the liquid sample into eight parallel detection channels and the flows, which were then merged into one combined flow exiting the system from the outlet at the top. The uniformity in the color of **Figure 3.3B** indicated that the fluidic resistance was likely properly dispersed into each channel. To find a representative flow pattern in eight detection channels, we simulated the flow velocity at the focal plane 50 μm above the bottom

electrode (at the surface of the PEG interface in the channel along the vertical direction) (the bottom panel of **Figure 3.3B**). The result demonstrated that, when the liquid samples entered the middle straight section in the channel, the flow velocity generally remained at the same level across all eight channels.

Next, we evaluated the fluidic performance through electrochemical reactions and electrical signals (**Figure 3.3C**). Specifically, we prepared a 100 mM phosphate buffer (PB) solution (negative) and a 100 mM PB solution containing 100 μM of Fc (positive), infusing each test solution into the microfluidic device for 60 seconds at a flow rate of 1 mL/min and repeating the process five times. We then continuously applied an oxidative potential of 0.4V to all working electrodes and measured the current on each. Theoretically, Fc can be oxidized and release electrons at the electrode, generating a corresponding current, when there is an applied voltage. As anticipated, we observed minimal currents during an infusion stage with PB, while significant current spikes were detected during Fc infusion (top panel of **Figure 3.3C**). Both the dynamic data and the current data taken from the last 30 seconds of each period that was collected and averaged (middle panel of **Figure 3.3C**), are depicted. These are representative of the general performance of the combined fluidic system, electrochemical reaction, and instrumental process. Notably, the system seems quite robust. The measurements are steady, and all 8 channels give similar amplitude and dynamic responses. Meanwhile, it is also noteworthy that, at a flow rate of 1 mL/min, the recorded signal demonstrates that a rapid response of the electrode is feasible, with a current change detected and reaching equilibrium within 2 seconds after a fluidic switch. As illustrated in the detail of the middle panel of **Figure 3.3C**, the device exhibited promising electrochemical

results, showing a high degree correlation and alignment with the simulation results. Finally, we note that the response from the electrochemical reaction primarily depends on the mediator concentration, so we prepared Fc solutions with varying concentrations (5, 10, 25, and 100 μM) and evaluated the corresponding Fc signal at a flow rate of 1 mL/min. Following the same testing procedures as described earlier, we demonstrated that there was a minimal difference between 25 and 100 μM of Fc, while 5 μM of Fc provided up to 74% of the signal compared to 100 μM of Fc.

Overall, these studies show that the ITO microfluidic device, its associated fluidic system, and electrochemical analyzing capabilities, were robust, reproducible, and rapid. Moreover, because of the snap-in or plug and play designs, we anticipated excellent utility in future antibody measurements.

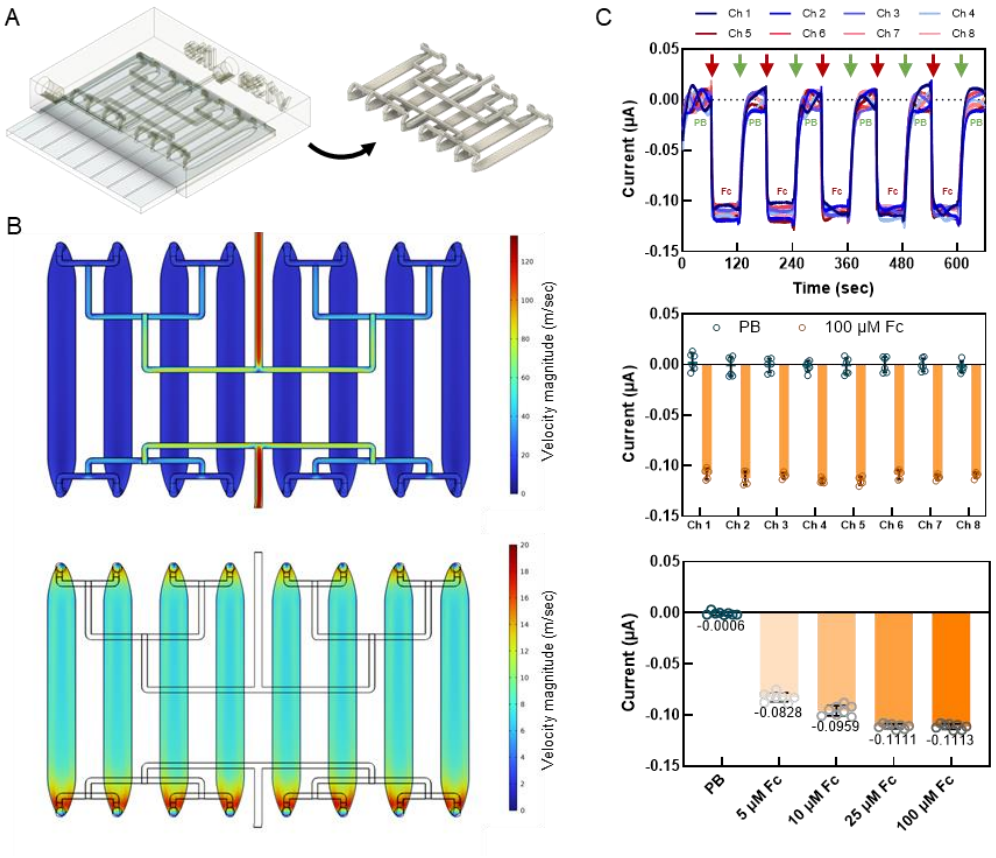

Figure 3.3 Simulation and fluidic test using redox mediator Fc.

(A) The 3D model for COMSOL simulation was generated directly from the original device model. (B) The top panel demonstrates that the infused fluidic sample can be distributed across all parallel channels and merge again at the exit. The bottom figure displays the flow velocity 50 μm above the bottom ITO electrode, representing the uniformity of flow within the channels. (C) The currents measured during repeated infusion between the PB solution and the Fc solution confirm the robustness and reproducibility of the overall system. *(n = 8)

3.3.3 Electroassembly of thiolated PEG-based sensor interfaces

For the determination of the sensor interface electrofabrication on ITO electrodes, we first recapitulated the steps previously described for the formation of the sensor interfaces for target IgG detection but within our device (**Figure 3.4A**). First, the

deposition solution (a mixture of 25 mM of Fc, 50 mg/mL of thiolated-PEG, and 250 μg/mL of C-terminus cysteine tagged protein G prepared in 0.1 M PB, pH 7.4) was added to immerse the ITO electrode. The interface electrodeposition occurred for 1 minute at a constant oxidative potential of 0.8 V. Solutions containing 62.5 mg/L of IgG and 0.1 g/L of protein G:HRP were also separately prepared for the final assembly. Wash buffer (0.05% Tween-20 in 0.1M PB) was used for rinsing the hydrogel to remove unconjugated residues between steps. Next, we prepared mediator Fc solutions (0.5 mM) with and without peroxide (100 μM) for the electrochemical output test. We note that the HRP on the reporter protein G ultimately converts the peroxide in the solution into redox-active radicals, leading to Fc oxidation. By applying a potential of 0 V on the electrode, we record the redox signals of Fc in the form of current. As shown in **Figure 3.4B**, we initially infused the Fc solution at a flow rate of 1 mL/min to record the system's blank signals. We then used this data to define the sensitivity of this interface. After 30 seconds, we switched the valve and introduced peroxide into the system, resulting in an instantaneous current spike (3 seconds) After a series of tests of IgG, we found that the current spike corresponded to the total amount of reporter protein G:HRP conjugated to the analyte IgG. Consequently, the current represented the IgG conjugated to the recognition elements.

In additional experiments, we then switched the valve and repeatedly infused the Fc solution to monitor the interface's response time. As recorded, the current returned to its initial level within 20 seconds, indicating that the H_2O_2 molecules in the hydrogel could be thoroughly eliminated shortly after the supply stopped. The repeated cycle reproduced an average 93% of the original response showing the reproducibility of the

sensor interface. The current data from the last 7.5 seconds of each period was collected and averaged, representing the general output of the system. The result was plotted in the right panel of **Figure 3.4B**. As demonstrated in **Table 3.2**, the relative standard deviation (RSD) of individual electrode with and without H_2O_2 were under 0.45% and 1.85%, respectively. Additionally, the RSD of the blank test (Fc solution) and test group (100 µM H_2O_2) across all eight electrodes were 2.53% and 3.56%, respectively. Together, the electroassembly of thiolated PEG-based sensor interfaces performed high reproducibility of hydrogel and interface formation.

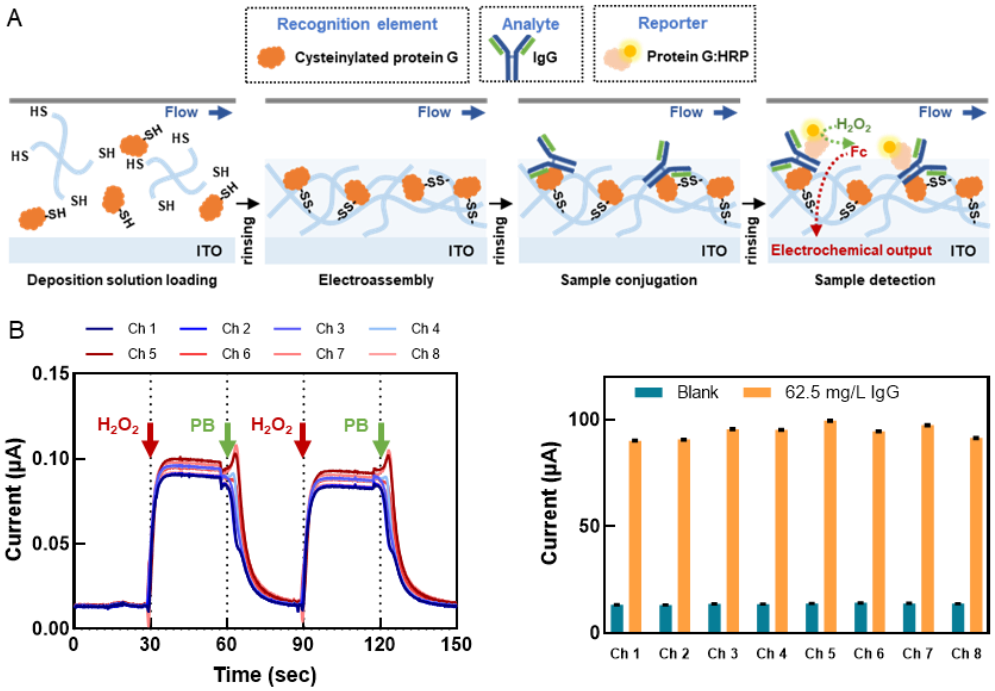

Figure 3.4 Electroassembly and reproducibility of sensor interfaces

(A) Schematic representation of the electroassembly of thiolated PEG-based sensor interfaces. Three major steps are required for the IgG detection: (i) electroassembly of the PEG recognition region, (ii) sample conjugation, (iii) reporter protein G:HRP conjugation. Rinsing is required for reducing non-specific bindings. (B) The current data for two cycles of PB- H_2O_2 infusion. The repeating data demonstrates high

reproducibility and robustness of hydrogel and interface formation. (C) The signals with H_2O_2 show significant differences from the blank. The low standard deviations also indicate the high stability of the signal delivering process. The sample preparation was assisted by Dr. Dana Motabar. *(n = 8)

Table 3.2 Sensor interface performance and stability of all eight channels.

	Ch 1	Ch 2	Ch 3	Ch 4	Ch 5	Ch 6	Ch 7	Ch 8	**Overall**
Blank	13.22	13.11	13.64	13.54	13.86	14.13	13.89	13.79	**13.65**
Blank SD	0.19	0.21	0.21	0.18	0.25	0.26	0.25	0.21	**0.35**
Blank RSD	1.47%	1.63%	1.51%	1.36%	1.77%	1.85%	1.77%	1.54%	**2.53%**
62.5 mg/L IgG	90.17	90.71	95.59	95.26	99.58	94.56	97.47	91.41	**94.34**
62.5 mg/L IgG SD	0.37	0.35	0.41	0.40	0.42	0.39	0.43	0.41	**3.36**
62.5 mg/L IgG RSD	0.41%	0.38%	0.43%	0.41%	0.42%	0.42%	0.44%	0.45%	**3.56%**

3.3.4 Detection of antibody titer and galactosylation

We first assessed the capability of the protein G recognition interface to conjugate and detect IgG. The experimental process and setup are previously discussed in **Scheme 3.2**. As illustrated in the left panel of **Figure 3.5A**, we employed a one-step deposition strategy to construct the recognition interface. Moreover, we tested the fluidic system using the design protocol outlined in **Table 3.1**. After the system conditioning steps, the deposition solution (a mixture of 25 mM of Fc, 50 mg/mL of thiolated-PEG, and 250 μg/mL of C-terminus cysteine-tagged protein G prepared in 0.1 M PB, pH 7.4) was

loaded, followed by electrodeposition for 1 minute at a constant oxidative potential of 0.8 V. The valve switched, rinsing the interface with the wash buffer. Varying concentrations (62.5, 250, and 1000 mg/L) of human IgG samples were prepared and infused into assigned microfluidic devices to incubate with electroassembled sensor interfaces. Following the protocol, the reporter protein G:HRP was then conjugated, forming the sandwich structure that converted the analyte content information into electrochemical signals. After conducting a series of tests at various IgG concentrations, we found that the current level corresponded to the total amount of sandwich conjugations (cysteine-tagged protein G-IgG-protein G:HRP). Consequently, a calibration curve was developed (**Figure 3.5B**), enabling the current to represent IgG concentration. As observed in the plot, the first and second measurements across all channel responses were rapid, consistent, and reproducible. The responses relative to their IgG concentration were then modeled using a Langmuir isotherm, showing a good fit ($R^2 = 0.96$).

Next, we evaluated the capability of the RCA120 recognition interface to conjugate and detect IgG galactosylation. As illustrated in the right panel of **Figure 3.5A**, we once again used the one-step deposition strategy to construct the PEG network with RCA120 recognition elements. The deposition solution (250 μg/mL of C-terminus cysteine-tagged protein G replaced with 500 μg/mL of RCA120) was loaded, followed by electrodeposition for 1 minute at a constant oxidative potential of 0.8 V. After testing varying concentrations (62.5, 250, and 1000 mg/L) of human IgG samples, we observed that the dynamic range of the sensor interface using one-step deposition with RCA120 differed from that with C-terminus cysteine-tagged protein G (**Figure 3.5C**).

This suggested that replacing recognition elements on the current interface condition may alter protein absorption and orientation on the interface. As discussed in previously published literature, adsorbed proteins quickly undergo surface-induced unfolding to increase their contact area, spreading out over the surface and interacting with neighboring proteins. Protein-protein interactions can further inhibit an adsorbed protein's ability to spread out on the surface[97]. To determine if there is a linear response region, we investigated lower concentrations of human IgG samples (0.1, 1, and 30 mg/L). The responses relative to their IgG concentration were then modeled using a Langmuir isotherm, showing a good fit ($R^2 = 0.94$). However, further investigation on the sample concentration may be required to find the linear range.

We have demonstrated that both sensor interfaces for detecting antibody titer and galactosylation can be electroassembled and constructed on ITO electrodes within a 3D printed microfluidic device. When combined with the fluidic system and automated valving and pump system, these results showcase the integrated system's potential for high-throughput measurements in bioprocessing settings.

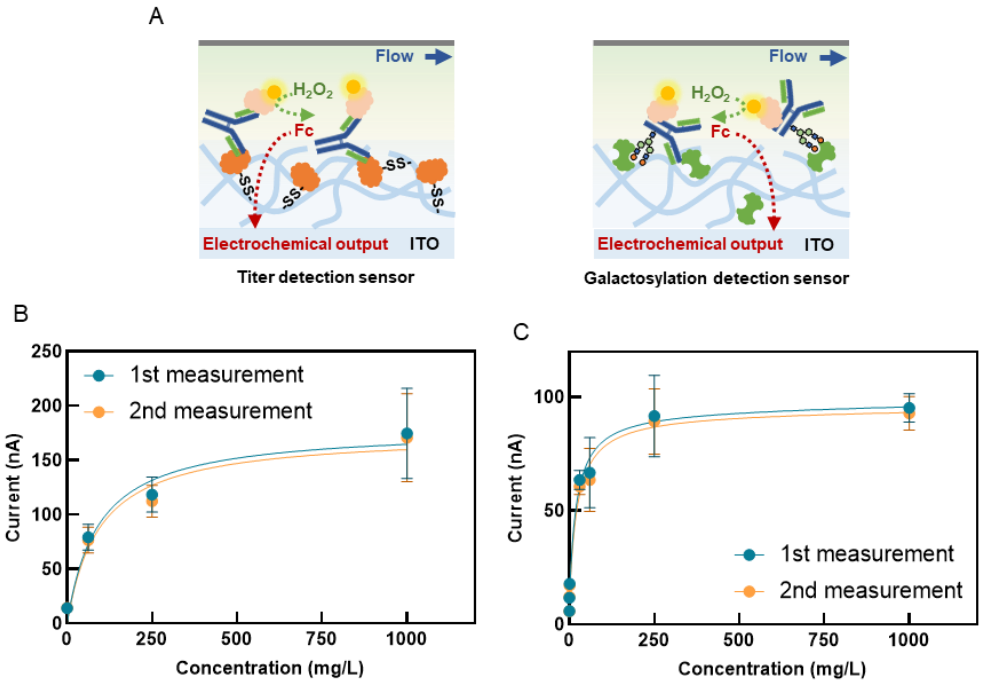

Figure 3.5 Analytical performance of antibody titer and galactosylation detection

(A) Schematic illustrates the interfaces that facilitate titer and galactosylation measurements in the microfluidic device. (B) Measurements taken with IgG (concentrations of 0, 62.5, 250, 1000 mg/L) and protein G: HRP (100 mg/L) with the integrated microfluidic housing and the tier detection sensor. Current responses from channels are consistent, rapid, and reproducible. Averaged responses can be fit with Langmuir isotherm model. (C) Measurements taken with IgG (concentrations of 0, 62.5, 250, 1000 mg/L) and protein G: HRP (100 mg/L) with the integrated microfluidic housing and the antibody galactosylation detection sensor. Current responses from channels are consistent, rapid, and reproducible. Averaged responses can be fit with Langmuir isotherm model. The sample preparation was assisted by Dr. Dana Motabar. *(n = 8)

3.3.5 Sensor evaluation with antibody in culture media

To broaden the applicability of the interfaces for upstream bioprocessing, we aimed to characterize the interfaces using a representative sample from an upstream setting. We

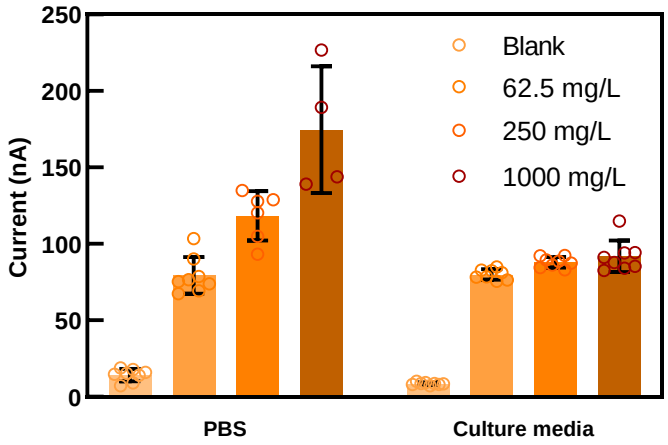

Figure 3.6 Electrochemical responses comparison between sample prepared in PB and culture media.

For the group containing 62.5 mg/mL IgG, the response remains consistent in both matrixes, while for higher IgG concentrations, the signal has significantly attenuated when prepared with DMEM. The sample preparation was assisted by Dr. Dana Motabar. *(n = 3)

chose Dulbecco's Modified Eagle Medium (DMEM) as the test matrix to determine if mammalian cell media components impacted the performance of the interfaces. The experimental conditions applied to the interfaces were consistent with those in previous sections, except that the systems were infused with solutions of IgG spiked into either PBS with 0.05% Tween-20 or DMEM. As depicted in **Figure 3.6**, we observed that the response was able to re-establish at lower IgG concentrations (62.5 mg/L). However, at higher IgG concentrations, the average current values and performance plateaued, even when applying identical experimental setups. In general, these results indicate that the interfaces can be used to qualitatively determine IgG concentration in mammalian cell culture media. However, further investigation of the sample preparation may be

required to provide more evidence for the sensor conjugation and find the linear range under this specific circumstance.

3.3.6 Regeneration of interfaces

In our previously published results, we demonstrated that a low pH regeneration buffer containing 0.1 M acetic acid and 1 M sodium chloride, pH 2.8, could effectively decouple protein-antibody interactions[42]. The regeneration buffer can remove the conjugated IgG while keeping the cysteinylated protein G (for the titer detection interface) intact on the PEG network. Here, we evaluated the regeneration process on this interface situated atop the ITO electrode in the microfluidic device. As depicted in the schematics in **Figure 3.7A**, after initial measurements, we infused the regeneration buffer into the microfluidic device at a flow rate of 0.5 mL/min for 10 minutes, followed by a rinsing buffer to remove acidic residues. The interfaces were then sequentially incubated with IgG sample solution and protein G:HRP solution, and repeat measurements were taken following the previously described protocol. As illustrated in **Figure 3.7B**, we compared three conditions (no IgG, 62.5 mg/mL of IgG, and 250 mg/mL of IgG) and found that the electrochemical responses were completely diminished after treatment with the regeneration buffer, suggesting that the IgG and the reporter protein G:HRP were decoupled and removed from the system. After reconjugating the IgG and protein G:HRP under the same conditions, we observed that the signal strengths from the second conjugation were nearly identical to the original measurements. The results suggest that the interfaces containing the recognition elements remained intact after the acidic decoupling process and were still able to maintain their initial capturing capability without significant loss of activity.

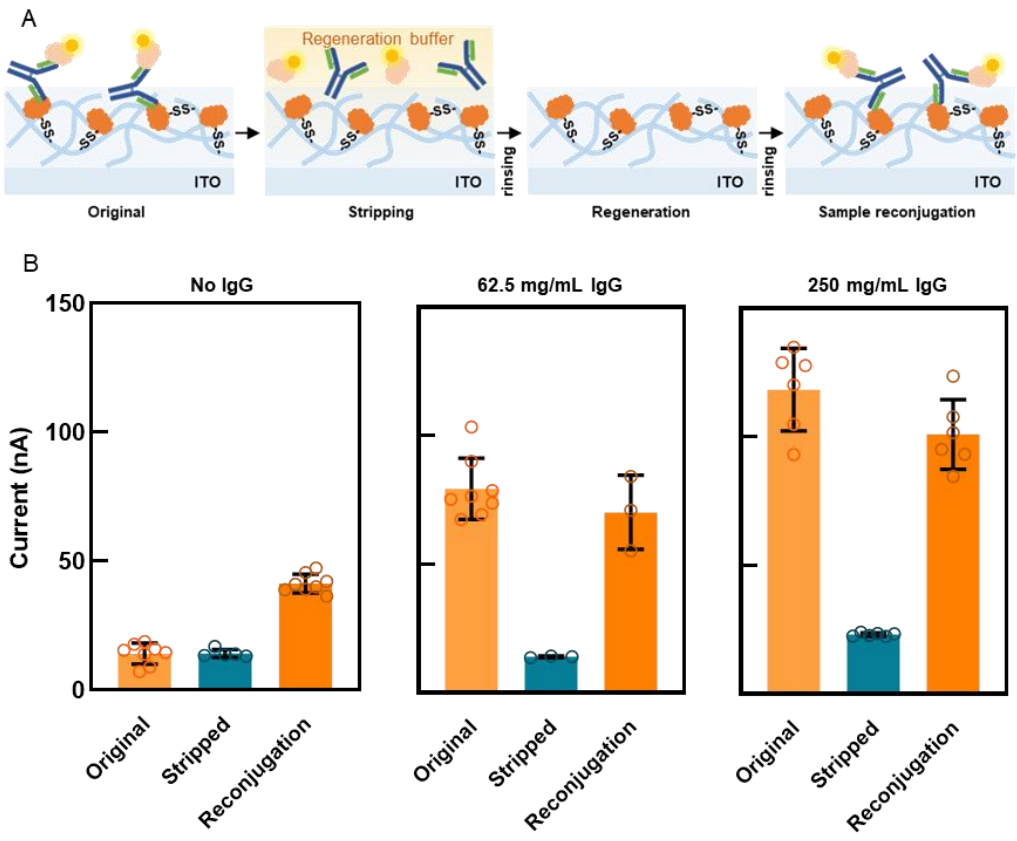

Figure 3.7 Regeneration of interfaces.

(A) Schematic representation of the regeneration process. The initial protein-antibody conjugation is decoupled due to the low pH environment, leaving the recognition elements retained on the PEG for next assembly. (B) The completely diminished electrochemical signals suggest that the interface has been regenerated. Meanwhile, the returning signals indicate that the conjugation can be reestablished and recapture the initial performance. *(n = 8)

3.3.7 Supporting Information

A

Valve	Position	Function/Reagent
A	1	Ethanol
B	1	Water
C	1	Degas

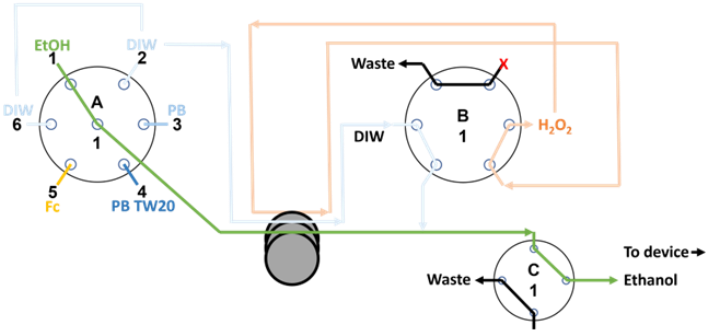

B

Valve	Position	Function/Reagent
A	2	Water
B	1	Water
C	1	Remove EtOH

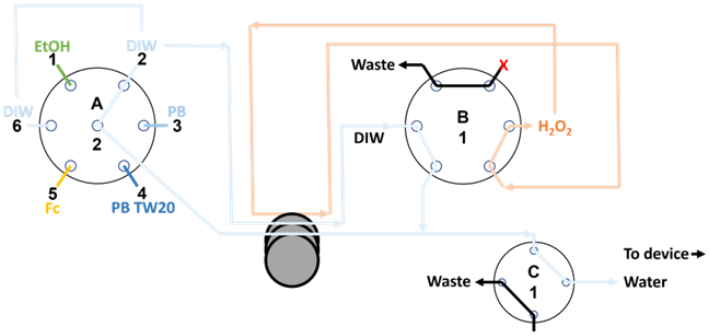

C

Valve	Position	Function/Reagent
A	3	PB
B	1	Water
C	1	Condition

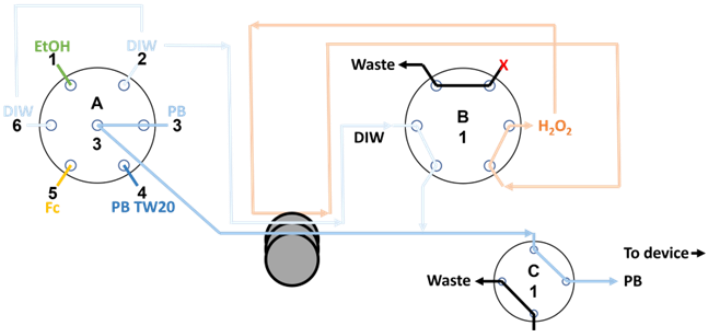

D

Valve	Position	Function/Reagent
A	4	PB + Tween 20
B	1	Water
C	2	PEG deposition

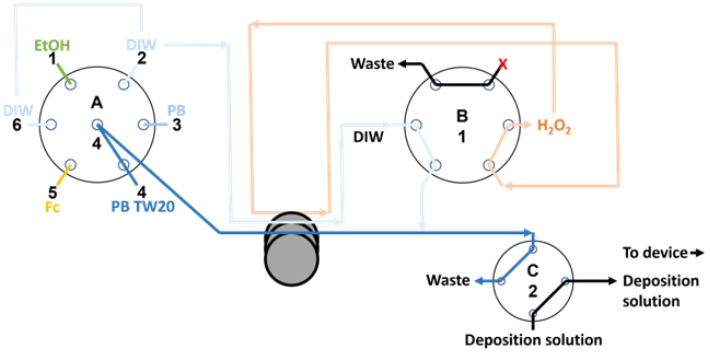

E

Valve	Position	Function/Reagent
A	4	PB + Tween 20
B	1	Water
C	1	Wash

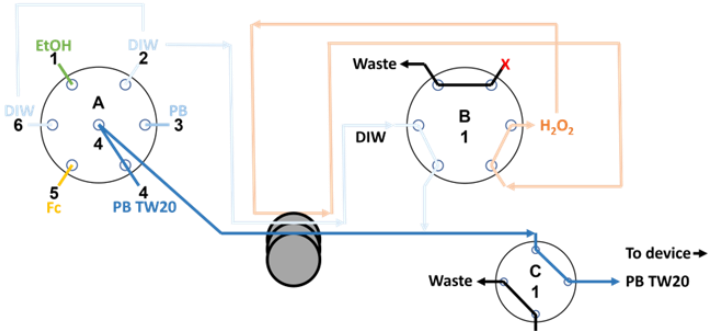

F

Valve	Position	Function/Reagent
A	4	PB + Tween 20
B	1	Water
C	2	IgG binding

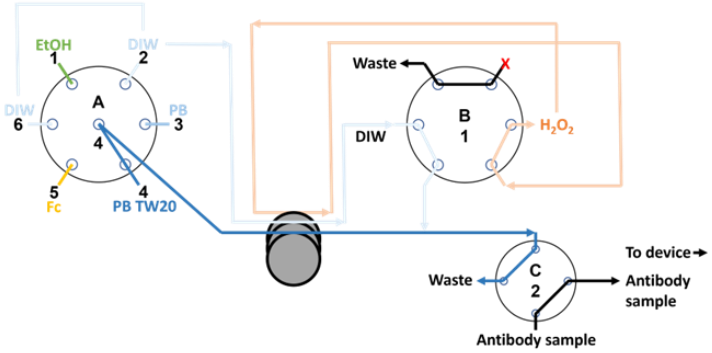

G

Valve	Position	Function/Reagent
A	4	PB + Tween 20
B	1	Water
C	1	Wash

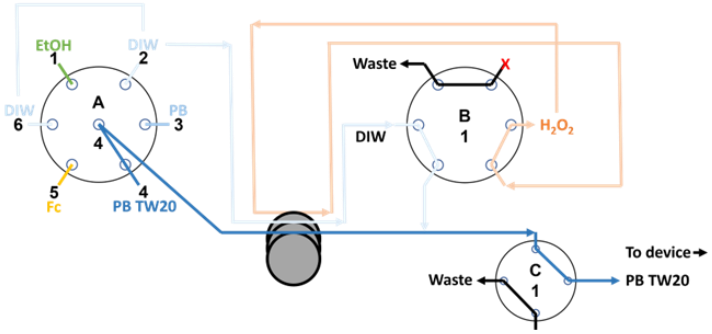

H

Valve	Position	Function/Reagent
A	4	PB + Tween 20
B	1	Water
C	2	Protein-G HRP binding

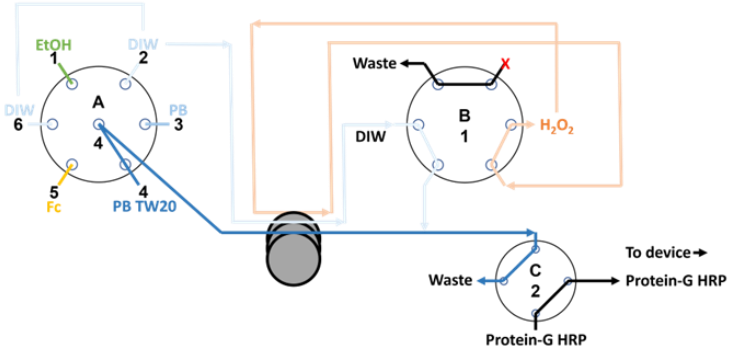

I

Valve	Position	Function/Reagent
A	4	PB + Tween 20
B	1	Water
C	1	Wash

J

Valve	Position	Function/Reagent
A	5	Fc
B	1	Water
C	1	Fc baseline

K

Valve	Position	Function/Reagent
A	5	Fc
B	2	H_2O_2
C	1	Fc + H_2O_2

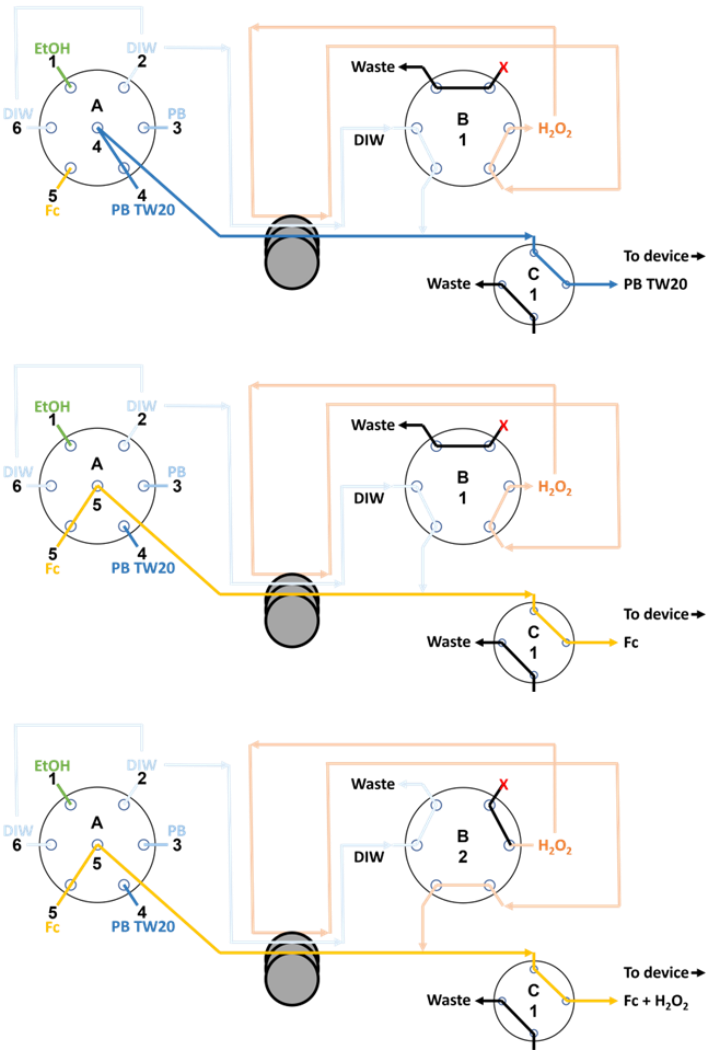

Figure S3.1 Schematic representation of the fluidic system of the proposed microfluidic platform.

(A) fluidic system degas process. (B) ethanol removal. (C) buffer conditioning. (D) deposition solution loading and PEG interface deposition. (E) buffer rinsing for deposition solution residue removal. (F) antibody sample injection and incubation. (G) buffer rinsing for sample residue removal. (H) protein G:HRP solution injection for antibody conjugation. (I) buffer rinsing for protein-G-HRP residue removal. (J) mediator Fc solution injection for system background recording. (K) reaction reagent (Fc + H_2O_2) injection for signal reading.

3.4 Conclusion

In this work, we developed a 3D-printed microfluidic device for rapid and high-throughput electrochemical interrogation of antibody titer and glycosylation. We first designed and fabricated an 8-channel microfluidic device coupled with ITO electrodes and their affiliated fluidic and electrical connectors. Specifically, we showcased that 3D printing was capable of precisely generating all fluidic routes and critical features, such as splitting pathways and parallel test channels, which are essential for stabilizing liquid sample distribution. To verify the design, we utilized COMSOL simulation to quantitatively examine the flow pattern and velocity across all test channels. The simulation results were shown to be highly correlated with subsequent fluidic test results. Equally important, by introducing the automated valving and fluidic transferring system, we enabled precise fluidic control that significantly reduced labor and manual processes required for operation. As a result, this led to a substantial enhancement in signal consistency and improvement in reproducibility. We then demonstrated that the "plug-and-play" modularity provided the opportunity for rapid device replacement and module switching, which could potentially offer solutions for multi-sample quality examination during biopharmaceutical production.

Next, we demonstrated that the microfluidic device is amenable to integration with the electroassembled thiolated PEG-based antibody detection interface. Specifically, we showed that the recognition elements could be constructed in a single, rapid step on the PEG network, and the analyte and reporter proteins could be successfully conjugated to the interface in the defined test channels via controllable fluidic transport. The integrated device detected a range of IgG concentrations, and the responses were

modeled by a Langmuir isotherm. We further evaluated the matrix effect and the interface regeneration for reuse, which aids in understanding the performance coupling with online operating systems and the possibility of lowering cost and accelerating analysis. Overall, in biomanufacturing, rapid assessment of both antibody titer and galactosylation can facilitate researchers' decision-making processes and improve product quality consistency for better efficacy and safety. Additionally, we envision this device as a standardized platform for universal electrochemical sensing applications in the future.

Chapter 4

Development of a universal spectroelectrochemical modular interface via additive manufacturing

4.1 Introduction

Information integration and modularization of advanced science catlyzes modern technology. The swift expansion of fields such as robotics, electric vehicle manufacturing, and even software development all share a common foundation in the principles of integration and modularization. Information integration and modularization, meanwhile, drive progress and innovation across the rapidly growing machine-to-machine communication (M2M) and internet of things (IoT), suggesting that, in the future, the development of sensors and the capability to digitize information defines the frontier of smart technology's growth and evolution. With its capability to translate biological information into processible digital languages, we foresee a transformation in electrochemistry akin to that already underway in robotics, where activities previously limited to specialists have broadened to encompass a diverse group of entrepreneurs, hobbyists, and even children. Such a paradigm shift for electrochemistry, in my view, could be expedited by the proliferation and simplification of makerspaces, which offer accessible design and fabrication resources to the public.

As the gold standard interface, multiwell plate is one of the most successful and highly modular tools in the biochemical field. It facilitates numerous fundamental biological research due to its capability to support miniaturized chemical reactions and high-

throughput optical screening. However, to be better blended into the era of information integration, we believe that the biochemical and biomedical fields need a novel multi-functional interface that can not only independently functionate but also serves as the key module that allow for easy attachment and detachment of end effectors, sensors, and other devices. Together, by bundling and integrating useful information from different aspects, we can ultimately generate a comprehensive picture of the target which promotes better decision making and phenomenon investigation (**Scheme 2.1**). In this study, we demonstrate the potential of this concept by employing 3D printing to create a spectroelectrochemical modular interface that integrates optical imaging, chemical reaction, and bidirectional electrical information processing capabilities in a manner that enables its integration into a multiwell plate analyzer. Specifically, we highlight the ability of this modular interface to provide unique and valuable insights in three burgeoning applications within the field of electrochemistry. We showcase its modularization capacity, which allows for seamless integration with conventional analytical tools such as electrochemical analyzers, plate readers, and fluorescence microscopes.

(i) Protein structural analysis. The investigation of antibodies and the development of antibody therapeutics have garnered attention for their potential to enhance our understanding of human diseases and their treatments. Redox modifications are a common method for optimizing antibody efficacy, but they also pose risks for maintaining functional structures (e.g., disulfide reduction)[98,99]. However, both upstream and downstream processes can be costly and time-consuming due to the complexities arising from limited access to antibody structural information and

constrained monitoring strategies during the development process. Our objective is to provide a straightforward yet reliable electrochemical tool that enables access to redox-based biological information and convert it into digital signatures using the proposed standardized system. However, traditional electrochemical methods often depend on intricate electrode surface modifications to enhance sensitivity and anti-fouling capabilities. Thus, we combined the 3D printer housing designed based on standard 96 well plate and indium tin oxide (ITO) coated glass into the basic functioning unit of the system. This constructed the missing critical functionality of the well plates and generated an interface that, when coupled with mediators, facilitates a robust digitalization of biochemical information into processible electrical signatures.

(ii) Electrofluorochromic materials analysis. Electrofluorochromic materials represent an innovative category of smart materials that exhibit reversible dynamic changes in color or opacity and fluorescence in response to an applied electric field [100,101]. These materials have attracted significant interest due to their unique optical properties and diverse applications across various industries, such as energy, electronics, and healthcare. For example, in the energy sector, energy-efficient smart glass[102] can modulate the transmission of light and heat, reducing the power consumption for temperature control. Other applications including flexible transparent displays[103], bioimaging[104], and data storage devices[105] are facilitating the development of a more sustainable world. However, the alteration in the optical properties of these materials is significantly correlated with the redox state transitions. That is, assessing the real-time and *in situ* responses offers invaluable insights into electron transfer processes. Thus, the growing demand for practical analytical solutions providing *in situ* or even

operando measurements has emerged as a critical bottleneck in understanding the fundamental mechanisms of these electrochemical reactions[106,107]. As two of the most sensitive sensing techniques, the combination of optics and electrochemistry has become a powerful tool for examining electron transfer and its associated optical characteristics. Advanced with its good electrical conductivity and optical transparency, ITO becomes one of the most widely used material for working electrode on electrochemistry-based biosensors and *operando* measurements [108–110]. Here, we demonstrate the potential of this system to offer comprehensive information for electrofluorochromic material characterization.

Our prior research has demonstrated the manipulation of redox-associated color changes and the ability to form molecular memory when coupled with redox mediators [27,31,35,39,40,111]. However, specialized instrumental setups are typically necessary to record the optical response in conjunction with electrochemical reactions. Meanwhile, high-throughput experimentation (HTE) has been widely integrated into established research setups due to its ability to simultaneously monitor and compare multiple target samples.[112] When combined with appropriate optical tools, high-throughput imaging offers the potential to rapidly investigate the dynamics of cellular pathways[113] and the local mechanical properties of materials[114]. In this study, we leveraged the transparency of ITO and facilitated rapid acquisition of catechol-PEG data, visualizing optical changes and capturing electron transfer information. Our 3D-printed device maximumly utilized the strength of multi-well design adopted from standard well plates for high-throughput operation and further equipped it's *in situ*, and *operando*

functionality, which together optimally enabling better control over conditions across all tested examples.

(iii) Electrobiofabrication and electrogenetic induction. Through the use of synthetic biology, there is an opportunity to engineer cells which can be incorporated into biohybrid devices for specific outputs (e.g., cell-based sensing interface). Electrogenetic approaches, which integrate electronic-responsive genetic structures with advanced signal processing and control mechanisms, offer a precise and controllable strategy to tackle programmable cells[115–117]. Our research team has specifically focused on electrogenetic methods that depend on diffusible mediators to carry redox information between an electrode and responsive cells, where the designed gene circuits can be promoted by the surrounding redox status[115,118]. Previous research has demonstrated the concept of "living electrodes" wherein the electrogenetic cells can be assembled onto gold surfaces via peptide surface display and electrode-generated hydrogen peroxide triggers the electrogenetic circuits[119]. However, the study of a chosen group of cells in the general population becomes challenging due to the lack of technique to enable simultaneous evaluation to the cell-cell interaction in the artificial biofilm. Mediator-facilitated electrodeposition, conversely, offers spatial control through physical confinement of the cells. Meanwhile, owing to the coupled electronics and optics, our ITO device can also modulate the redox nature of the microenvironment, providing new insight in biological responses.

Overall, by advancing 3D printing and ITO configurations that manipulate defined microenvironments and at the same time enable bidirectional transfer of the signaling

events, we are in a better position to discover new insights on the complexities of the redox-signaling. By developing an easy-to-use modular device that incorporates electronic and optical sensors as well as convenient liquid handling, we believe we can position electrochemistry to play an important and integral role in further developing information transfer. That is, we anticipate contributing biological information to the Internet of things. Such advances will serve to elucidate fundamental understanding of redox phenomena at the molecular levels and at the same time, facilitate new knowledge of cell physiology and other complex biological systems. Perhaps these will contribute to the development of new therapeutic molecules and biomaterials.

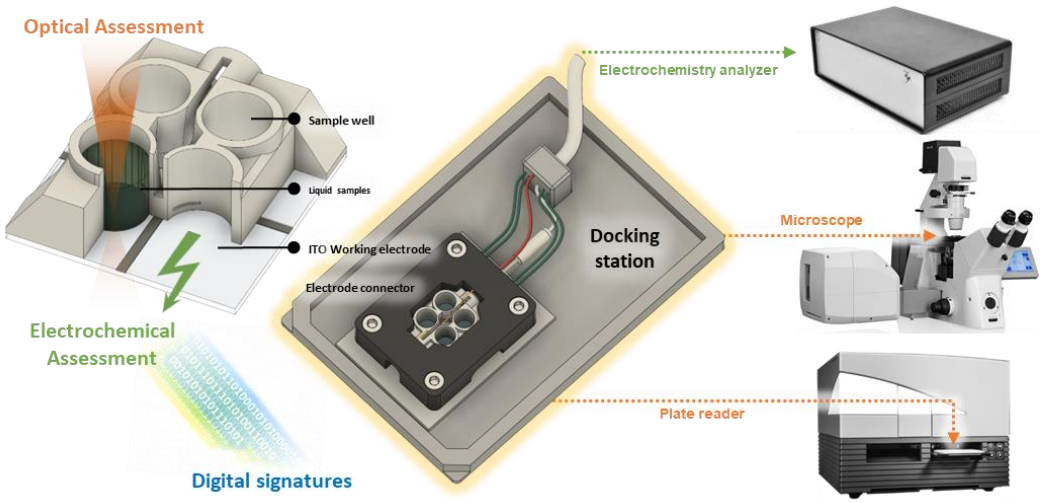

Scheme 4.1 The multi-well spectroelectrochemical modular system.

4.2 Materials and Methods

Materials

Indium tin oxide coated glass slide, square (surface resistivity 8-12 Ω/sq), IgG from human serum, ethylenediaminetetraacetic acid (EDTA), Trizma HCl and Trizma base

(collectively, Tris), 5,5-dithio-bis-(2-nitrobenzoic acid) (DTNB, aka Ellman's Reagent), potassium ferricyanide(III) (Ferricyanide), potassium hexacyanoferrate(II) trihydrate (Ferrocyanide), and phosphate buffered saline (PBS, pH 7.4) were purchased from Sigma-Aldrich (St. Louis, MO). Black 3D printing resin was purchased from ELEGOO (Guangdong, China). 1,1′-Ferrocenedimethanol (Fc) was purchased from Santa Cruz Biotechnology (Dallas, TX). L-histidine monohydrochloride monohydrate and L-histidine were purchased from Avantor (Allentown, PA). 0.1 % formic acid was purchased from Honeywell (Phoenix, AZ). A 1 M stock solution of Fc was prepared in DMSO, and dilutions were prepared in PBS freshly for each experiment. TCEP bond breaker solution, Zeba Spin Desalting columns (7K MWCO), Slide-A-Lyzer Dialysis Cassettes (10K MWCO), and DL-dithiothreitol (DTT) were purchased from Thermo Fisher Scientific (Waltham, MA). Ag/AgCl reference electrode was purchased from Pine Research Instrumentation (Durham, NC)

Device fabrication and performance check

The 3D printed 4-well and 8-well device with ITO electrodes was designed based on a standard 3-electrode system including a device with a 25 mm × 25 mm ITO working electrode (split into 4 or 8 sub working electrodes), and a docking connector with a Pt wire serving as the counter electrode, and an Ag/AgCl reference electrode. The connector immobilized the device onto the docking station which allows wiring connection to the electrochemical analyzer. (i) To make the 3D printed device housing, designs were created using Autodesk® Fusion 360 and Autodesk® Inventor (Autodesk, Inc, US). The CAD files were then converted to writing-path using the Chitubox 1.9.4 (Guangdong, China). Mars 3 Pro was used to fabricate the housing.

When the printing process was completed, the substrate was placed in a bath of methanol with gentle shake for 1 minute and then dried with nitrogen. This step was repeated three times to thoroughly remove any uncured residues. The prints were then further cured under a 20-Watt UV lamp for 10 seconds followed by a 30-second rest at room temperature. This step was repeated three times to achieve full strength. Purchased precut ITO glass (25 mm × 25 mm) was patterned with laser engraver to physically define all electrodes and the connecting region. The cured housing was then aligned with the laser patterned ITO glass and annealed together with the same photosensitive resin used for printing. (ii) The electrode connector followed the same design and fabrication steps described previously. 4-way spring connectors (Digi-Key, Part Number 478-4688-6-ND) were then attached to the designed location and enabled the physical connection to the ITO device. The 4-way spring connectors were then soldered with the wires and the Molex female sockets (Digi-Key, Part Number WM9449DKR-ND) for later connection with Molex rectangular cable (Digi-Key, Part Number WM19582-ND) which connected to the electrochemistry analyzer. (iii) The docking station was made of acrylic sheet. The size of the docking station is based on the size of a regular 96 well plate. The acrylic sheet was then cut using CO_2 laser engraver and machined to generate the screw threads for the connector.

Antibody reduction protocol

Human IgG samples were prepared to 5mg/mL in phosphate buffered saline (PBS), pH 7.4. For reduced samples, TCEP was added to 1-4 mL of human IgG for a final TCEP concentration of 10 mM. Both intact and reduced samples were covered and incubated for 3 hours at room temperature. Intact and reduced samples were dialyzed using Slide-

A-Lyzer dialysis cassettes (0.5 mL to 3 mL, 10K MWCO) in 1,000 times the dialyzed sample volume of 1X phosphate buffered saline (pH 7.4), overnight at 4°C. Samples were aliquoted and stored at -20° C if not immediately used. Buffer controls were performed using PBS (pH 7.4) with 10 mM TCEP and overnight dialysis at 4° C with the same setup as IgG sample dialysis.

Determination of antibody reduction by standard approaches

To confirm IgG reduction, microchip capillary electrophoresis (CE) was performed using a 2100 Bioanalyzer (Agilent). Intact and reduced IgG samples were run using the Agilent Protein 230 kits under non-reducing conditions following the manufacturer's protocol. A sulfhydryl assay was performed to measure the free thiol content of intact and reduced antibody samples. Briefly, 1.25 mL of reaction buffer (100 mM sodium phosphate, 1 mM EDTA, pH 8) was mixed with 25 µL of 4 mg/mL DTNB solution (in reaction buffer). 125 µL of intact or reduced IgG (3 mg/mL, 1.5 mg/mL, 0.75 mg/mL, and 0.25 mg/mL, dilutions made using PBS) was added to the mixture, followed by 15 minutes of incubation at room temperature. After incubation, 200 µL of each reaction mixture was added to a clear 96-well plate in triplicate. Spectral absorption at 412 nm was measured and free thiol content was calculated using the molar extinction coefficient of TNB (14,150 M-1 cm-1) according to the manufacturer's protocol.

Determination of antibody reduction by mediated ITO-based electrochemical probing

Cyclic voltammetry (CV) and chronocoulometry (CC) measurements were taken using a CHI1040C electrochemical analyzer (CH Instruments; Austin, TX). The

measurements were performed with the designed 3D printed 8-well device with ITO electrodes and its docking station. For electrochemical measurement, samples were diluted to the designed concentration with the Fc stock solution and PBS with Fc final concentration to be 50 μM. CV measurements were taken over a potential range of 0 V to 0.5 V at a scan rate of 2 mV/s. Chronocoulometry measurements were taken at a constant input potential of +0.4 V for 60 seconds and then switched to a reductive potential of +0.1 V for another 60 seconds. 50 μL of the Fc standard solution was added into each well for the blank measurement followed by 100 μL PBS rinse to remove residue. 50 μL of the sample was then added into the well for the following CV or CC measurements.

Determination of antibody reduction by mediated gold-based electrochemical probing

CV and CC measurements were taken using the same setup as above but with the following modifications. The electrochemical setup was a 3-electrode system containing a 2 mm diameter gold working electrode, a platinum wire counter electrode, and an Ag/AgCl reference electrode. 100 μL of sample was loaded into a low-volume sample cell (BASi Research Products). The working electrode was placed in the low-volume cell, and the cell was submerged in 1 mL PBS alongside the reference and counter electrodes. The porous frit of the low-volume cell facilitated contact between the sample (IgG) and reference (PBS) solutions while avoiding cross-contamination. A single gold working electrode was used for each of three replicate measurements. Between each measurement, the gold working electrode was polished using 0.05 μm alumina powder.

Measurement of the impedance and surface characteristics on ITO devices

Cyclic voltammetry (CV) and Electrochemical Impedance Spectroscopy (EIS) measurements were performed using a CHI6273C electrochemical analyzer (CH Instruments; Austin, TX). The 3D-printed 8-well ITO devices were set up the same as mentioned in the previous sections but with the following modifications. Both intact and reduced human IgG stocks (5 mg/mL) were diluted to the targeted concentrations with PBS. 2 mM ferricyanide ($K_3Fe(CN)_6$, Ferri) stock solution and 2 mM ferrocyanide ($K_4Fe(CN)_6$, Ferro) stock were prepared separately in PBS and then mixed at 1:1 ratio before use as the final solution (Ferri/Ferro solution) and 100 μL of the solution was added into each well for CV and EIS measurements. CV measurements were taken over a potential range of -0.3 V to 0.7 V at a scan rate of 100 mV/s. Before EIS measurements, the open circuit potential was checked each time. Then, EIS measurements were taken using a frequency range from 0.05 Hz to 10 kHz with a perturbation amplitude of 5 mV from the open circuit potential.

Measurement of the impedance and surface characteristics on standard gold electrodes

The regular 3-electrode system was set up the same as mentioned in the previous sections. 20 mL of Ferri/Ferro solution was prepared in a glass beaker for the CV and EIS measurements. Before the measurements, the gold standard electrodes were rinsed with PBS and Ferri/Ferro solution to remove any residues. CV measurements were taken over a potential range of 0 V to 0.5 V at a scan rate of 100 mV/s. EIS measurements were taken using a frequency range from 0.05 Hz to 10 kHz with a perturbation amplitude of 5 mV from the open circuit potential.

Fluorescent thiolated-PEG binding test to the electrodes

The FITC labeled PEG-SH was prepared in the PBS with the FITC-PEG-SH at the final concentration of 5 mg/mL. 20 μL of the solution was then dropped on the electrodes and incubated in a covered box at room temperature for 2 hours. The electrodes were then rinsed with PBS 3 times to remove any unattached fluorescent molecules. The electrodes were checked under a microscope for the residue of the FITC-PEG-SH.

Catechol-PEG hydrogel fabrication on ITO

Electrodeposition was performed using the designed 3D printed 4-well device with ITO electrodes and its docking station and performed with a CHI1040C electrochemical analyzer (CH Instruments; Austin, TX). The deposition solution containing 50 mg/mL PEG-SH with catechol (50 mM) was prepared in the 100 mM potassium phosphate buffer (pH = 7.4). 100 μL of the solutions was loaded into the wells and applied with constant voltage (1V) for 30 to 60 seconds, unless otherwise noted. The unreacted solutions were immediately removed from the wells followed by 3 times of 200 μL PBS rinse to remove residues. The catechol-PEG gels were then incubated in 200 μL PBS for 30 minutes to remove access unattached free catechol in the hydrogels.

Determination of redox states of the catechol-PEG on ITO using redox mediators

Mediators (0.2 mM of Fc and 0.5 mM of Ru) were prepared in the 100 mM potassium phosphate buffer (pH = 7.4) and 100 μL of the mediator solution was then added to the wells. CV measurements were taken over a potential range of -0.6 V to +1 V at a scan rate of 10 mV/s. Chronocoulometry measurements were taken at a constant input potential of +1 V for 60 seconds and then switched to a reductive potential of -0.6 V

for another 60 seconds. Same experiments were also repeated with PBS without mediators. The device was placed under the fluorescence microscope for imaging or inserted into the plate reader (Molecular Devices, San Jose, CA)/ TECAN Spark plate reader (Tecan Group Inc.; Männedorf, Switzerland) with the docking station for absorbance/ fluorescence measurements. Videos were recorded using Camtasia recording software (TechSmith, East Lansing, MI). The images/ videos were processed using ImageJ and Lightroom (Adobe, Mountain View, CA).

Functional artificial biofilm fabrication with cells

Electrodeposition was performed using the designed 3D printed 4-well device with ITO electrodes and its docking station and performed with a CHI1040C electrochemical analyzer (CH Instruments; Austin, TX). 2X stock solutions containing 100 mg/mL PEG-SH containing 10 mM of Fc were prepared in 100 mM potassium phosphate buffer (pH = 7.4) and then mixed with 2X cell stock (DH5α-dScarlet) solutions prepared in PBS (OD_{600}=6) to form the final cell/PEG-SH/Fc solutions. 100 μL of the solutions were loaded into the wells and applied with constant voltage for 120 seconds, unless otherwise noted. A constant voltage of +0.8, was applied to induce PEG-SH cross-linking for the test. The unreacted solutions were immediately removed from the wells followed by 3 times of PBS rinse to remove residues. 150 μL of PBS or culture media containing DH5α-sfGFP (OD_{600} = 0.3) were then added into the wells for the coming tests. DH5α-dScarlet and DH5α-sfGFP are both prepared starting from an overnight culture and reinoculated in the LB media from OD_{600} = 0.01. The cells then harvest when OD_{600} reached 0.3. The cells were then washed with PBS twice to thoroughly remove the LB media and prepared into the target concentration in the PBS

or culture media (DH5α-dScarlet in PBS, OD_{600} = 12; DH5α-sfGFP in LB, OD_{600} = 0.3).

Chemical induction and electrogenetic induction using hydrogen peroxide

The following solutions were prepared: (i) LB media with or without DH5α-sfGFP, (ii) (iii) LB media containing 200 μM of hydrogen peroxide (with or without DH5α-sfGFP). 150 μL of the solutions were added into the wells containing artificial biofilm settling on the bottom ITO electrode. For the groups aimed to evaluate the electrogenetic induction, a reductive potential (-0.8 V) was applied to the wells containing LB media and LB media with DH5α-sfGFP (OD_{600} = 0.3) for 30 minutes to verify the later fluorescence signals from the DH5α-dScarlet cells in the artificial biofilm. All cells then cultured in a 37ºC incubator for 3 hours.

Cell imaging and fluorescence detection

The device was examined with the Zeiss Axio Observer Z1 confocal fluorescence microscope (Carl Zeiss AG, Jena, Germany) for imaging with the docking station for fluorescence measurements. The images/ videos were processed using ImageJ and Lightroom (Adobe, Mountain View, CA).

4.3 Results and Discussion

4.3.1 Rapid Electrochemical Detection for Antibody Structural Integrity Using ITO coupled 3D-printed Platform.

4.3.1.1 Fabrication of the ITO device and the docking station

In this study, we developed an experimental platform consisting of an ITO-based electronic device and a docking station (Figure 4.1) for simultaneous electrochemical and optical characterization of samples. The system employs a typical 3-electrode setup, with a shared reference and counter electrode and customizable working electrodes, providing an operando operating interphase. The ITO device comprises two principal elements that were fabricated separately: (i) a 3D printed housing and (ii) transparent ITO bottom electrodes. We selected ITO as the working electrode (WE) due to its compatibility with optical signals. The independent wells and docking station were designed with the same dimensions as a conventional 96-well plate to facilitate adaptation to conventional optical/electrochemical analyzers. As depicted in **Figure 4.1A**, the 3D-printed housing is positioned on the transparent ITO bottom electrodes, with the size of the 3D-printed wells determining the area of the bottom working electrode. The central well for the agarose salt bridge is shared by neighboring wells, facilitating ionic transport between the working, counter, and reference electrodes. **Figure 4.1B** presents a schematic of the electrode connector and the ITO device. The connector acts as an interface, providing a physical connection between the ITO device and the electrochemistry analyzer. The 4-way spring connectors touch the contact points for the working electrodes on the ITO device, while the platinum wire anchored

to the connector makes physical contact with the central salt bridge, serving as the counter electrode.

To assemble the functional system, 1% agarose in a 1M KCl solution was first heated, and 60 µL of the liquid agarose was injected into the central well of the ITO device to cast the agarose salt bridge, enabling the ionic connection for the electrochemical reactions. After the agarose solidified, the reference electrode was connected to the side opening of the device, creating a space for subsequent salt bridge solution filling. Next, 150 µL of 1M KCl solution was added to the central well, submerging both the agarose salt bridge and the side-way reference electrode. With the device fully assembled, the counter electrode on the connector was immersed in the 1M KCl solution present in the central salt bridge well, completing the circuit of the standard 3-electrode system. In parallel, with its high customizability using 3D printing, we also created an 8-well version for high-throughput sample detection and to demonstrate the remarkable versatility of this platform. The steps for the ITO device fabrication and assembly are illustrated in **Figure 4.1C**.

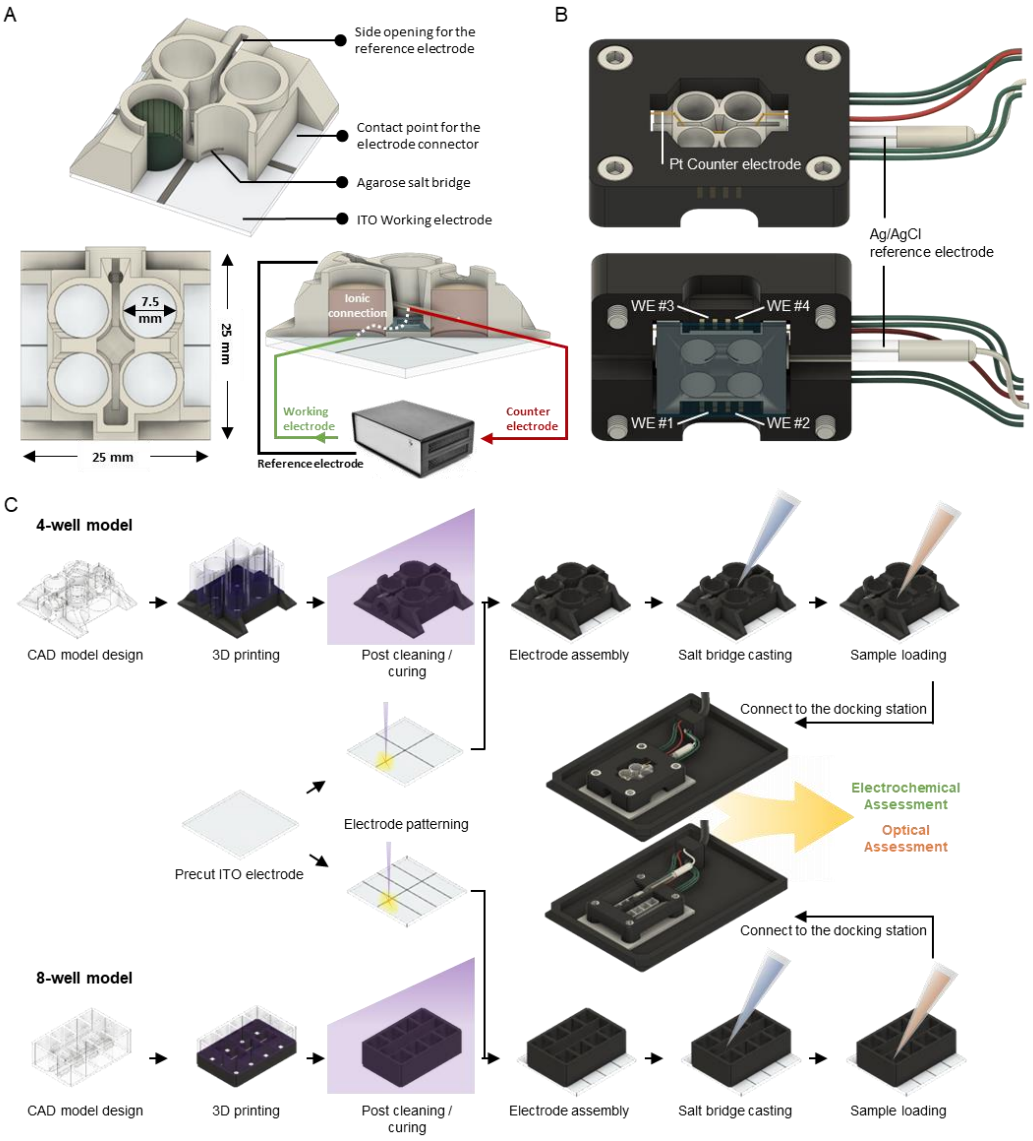

Figure 4.1 The fabrication of the testing platform using customizable 3D printed hosing coupled with transparent patterned ITO electrode.

(A) The 3D printed housing with sample wells and central salt bridge well is located on the top of the ITO electrodes. The central salt bridge facilitates the ionic transport and electron flow. (B) The electrode connector is equipped with a platinum wire as the counter electrode. When assembled with the ITO device, the counter electrode immerses into the salt bridge and completes the electrochemical circuit. The spring connectors touch the contact points on the ITO device and link to electrochemistry analyzer. (C) The 3D model was initially designed using CAD software and the prints

were fabricated using LCD resin 3D printers. Several methanol rinses were applied to remove any uncured resin. The prints were then post-cured in a UV box to reach the maximum structural strength. Meanwhile, the ITO coated glasses were patterned using carbon dioxide laser engraver to generate the electrodes that aligned with the wells on 3D printed housings. UV activated glue was used to bind the 3D printed housings and the patterned ITO electrodes. Once the device assembly is completed, the electrode area is well-defined by the cross-section area of the wells. An agarose gel was then cast in the middle chamber which later served as the salt-bridge that connected all four wells. When connected to the docking station, the ITO electrodes could be individually controlled by the electrochemistry analyzer.

4.3.1.2 Anti-biothiol fouling indium tin-oxide for antibody reduction measurement.

The stability of the interphase and sensor performance are critical for achieving a sensor with a wide dynamic range and versatility. However, conventional bare gold or unmodified electrodes commonly experience electrode fouling due to nonspecific binding, which can be further aggravated by biothiol-enhanced binding because of the strong gold-thiol bond formation[120] (**Figure 4.2A**). To understand how biothiol binding influenced redox measurement, we employed a surface sensitive technique, Faradaic EIS, which can provide information about surface properties and the interaction of surfaces with species of interest[121]. For this, the Faradaic EIS technique measures the impedance change of the interface on the electrode surface using the redox reaction of redox couple (Ferri/Ferro). First, we verified the uniformity across all ITO and gold electrodes via testing their initial impedances and CV profiles (**Supplementary Figure S4.1**). For sample measurements, we incubated 100 µL of 0.25 mg/mL reduced IgG in PBS in the wells of the ITO device and on the gold standard electrodes for 10 to 60

minutes. Electrochemical impedance spectroscopy (EIS) measurements in the presence of 1 mM Ferr/Ferro solution showed that the impedance of bare gold and ITO was 456 Ω and 6256 Ω, respectively. However, when incubated with reduced IgG samples, the impedance of the gold electrode significantly increased with increasing incubation time. After 60 minutes of incubation, the impedance of the gold electrode increased by 2212%, whereas it was only 83% for ITO. The impedance increase of ITO was found to be stable after reduced IgG incubation, with very little correlation to incubation time, and an overall average impedance increase of 86% (**Figure 4.2B**). The cyclic voltammetry (CV) results were consistent with the EIS measurements, as we observed that only the distance between the reduction peak potential and the oxidation peak potential widened (indicating a decrease in surface electron transfer efficiency) on ITO, while the peak current did not show significant reduction. In contrast, when gold was treated with reduced IgG, both peak-to-peak widening and significant peak current attenuations were observed. After incubation with the reduced IgG on both electrodes, the gold electrode showed a significant increase impedance of EIS and great redox peak separation of CV results, compared with ITO. It indicates that the reduced IgG can facilitate the surface fouling of the gold electrode to a greater extent compared to the ITO electrode. Further confirmation of the anti-biothiol fouling capability using ITO, 10 µL of 5 mg/mL FITC-labeled thiolated-PEG prepared in PBS was dropped on gold and ITO and incubated in a cover box for 2 hours. After the FITC-PEG-SH residue was removed from both electrodes with 3 rinses for PBS, we monitor the fluorescence with a fluorescence dissecting microscope. We found a clear green, fluorescent spot on gold whereas we noticed the minima fluorescent response on ITO (**Figure 4.2C**). This result

corresponds to the impedance measurements from EIS. Overall, we confirmed that ITO could work as a good electrode material for biothiol measurement and is capable of performing good anti-biofouling characteristics while treated with antibodies with varying reduction levels.

The impedance for both gold and ITO calculated based on the fitting of Nyquist plots are shown in **Table 4.1**.

Table 4.1. The calculated impedance of gold and ITO treated with reduce IgG.

Time / Electrode	Bare	10 mins	20 mins	30 mins	60 mins
Gold	455.60	3011.95 (+561%)	4686.52 (+929%)	5801.17 (+1173%)	10533.4 (+2212%)
ITO	6256.63	11974.40 (+91%)	11846.90 (+89%)	12093.5 (+93%)	11449.70 (+83%)

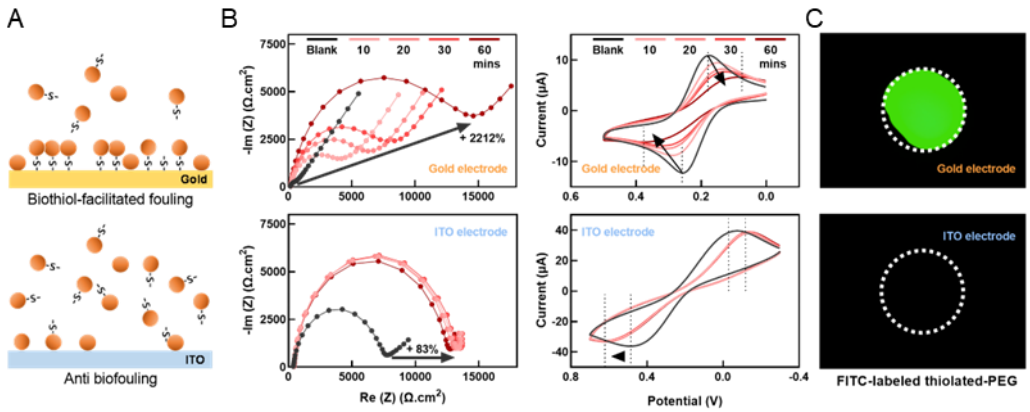

Figure 4.2 The measurement of reduced structure in the antibody via ITO electrode. (A) The exposed thiol groups from the reduced IgG would facilitate the biofouling of the gold electrode. This process is also a time-dependent phenomenon which makes the performance unpredictable. The same phenomenon on ITO electrode was significantly

attenuated. The performance both on CV and CC remain representative. The FITC-labeled thiolated-PEG staining test visualizes the gold-thiol bond formation and confirms ITO has a better anti-thiol-fouling capability. (B) The gold-thiol binding facilitated the increase in EIS measured at the surface of the gold electrode. We monitored a 2212% increase in EIS after 60 minutes of incubation in the solution containing reduced antibodies. This phenomenon was not seen when the electrode material was replaced with ITO. The EIS increase could be recognized as protein nonspecific binding and this value instantly plateaued after 10 minutes of incubation. The CV current profiles verified the results from EIS measurements. Both peak broadening and current attenuation were monitored at the groups using gold electrode, while the groups using ITO electrode only demonstrated a slight peak broadening with minimum current attenuation. (C) The fluorescence signal monitored under fluorescence microscopy indicated the gold-thiol binding between fluorescent-labeled thiolated PEG and the gold surface.

4.3.1.3 Detection of antibody reduction using mediated probing.

Here, we test the efficacy of our method for measuring molecular electrochemical properties by demonstrating the electrochemical characterization of cysteine, which is a well-characterized redox-sensitive molecular "switch" in biological systems. When antibodies undergo reduction, including disulfide bond disruption, there is a corresponding increase of cytsteine thiol groups. As a result, smaller IgG variants (Heavy-Heavy, Heavy-Light, Heavy, and Light chain forms) that have exposed free thiol groups are present in the samples (left panel in **Figure 4.3A**).

We propose to exploit redox properties of the exposed thiol groups to characterize the reduction and disassembly of antibodies. The mediator Fc works was a messenger shuttling the electrons from the free thiol on the reduced antibodies to the electrode.

Specifically, the oxidative form of Fc can diffuse into the solution and interact with the free thiol groups and capture electrons[122,123]. This switches the redox state of Fc from oxidative to reductive. The reduced Fc then interacts with the ITO electrode and delivers electrons and returns to its oxidative form again. The redox cycling reaction serves as a bi-direction flow that carries the structural information correlated to the disulfide bond reduction to the electrochemical analyzer and converts it into a digital signature (right panel in **Figure 4.3A**). The ability to detect such changes in redox properties through electrochemical characterization holds immense promise in the field of biosensing, where rapid and accurate detection of molecular changes is essential for diagnosis and treatment.

As illustrated in **Figure 4.3B**, when coupled with redox mediator Fc, two electrochemical methods with distinct voltage input schemes, cyclic voltammetry (CV) or chronocoulometry (CC) can be used for the detection of the biothiol from the exposed cysteine on the reduced IgG. For CV, the oxidative and reductive peak currents ($i_{peak,ox}$ or $i_{peak,red}$) are defined as the minima and maxima in the peak currents, respectively. For CC, the oxidative charge (ΔQ_{Ox}) is defined as change in charge during the first 60 seconds, while the reductive charge (ΔQ_{Red}) is defined as the change in charge during the second 60 seconds. To assess the ability of the ITO device coupled with redox mediator for differentiating between intact and reduced antibody, we used commercially available IgG from human serum as a standard for the intact antibody. Tris(2-carboxyethyl)phosphine (TCEP) was used as the reducing agent for the reduced antibody to cleave the disulfide bonds that connect the critical components of the antibody. TCEP was spiked into the IgG stock (5 mg/mL) at a final concentration of

10 mM and incubated for 4 hours, followed by dialysis into PBS to purify the IgG stock. To characterize the antibody structural integrity, microchip capillary electrophoresis (CE) was used (**Figure 4.3C**). CE can differentiate samples based on molecular weights, allowing us to investigate the composition of the sample (e.g., heavy chain, light chain, and any intermediate species) after reduction. In brief, the CE results showed that the reducing agent TCEP was able to convert the intact IgG into fully reduced heavy and light chains. However, the reducing agent TCEP used for IgG reduction is known to have has its own electrochemical signature[124] that could potentially interfere with the identification of the electrochemical signature of the biothiol in the reduced IgG samples. Therefore, buffer controls for intact and reduced IgG (**Supplementary Figure S4.2**) were used to confirm that TCEP was effectively removed after dialysis. Overall, we confirmed that the TCEP reduction protocol was effective in breaking the disulfide linkages in the intact IgG and forming its subcomponents with exposed free biothiol sites.

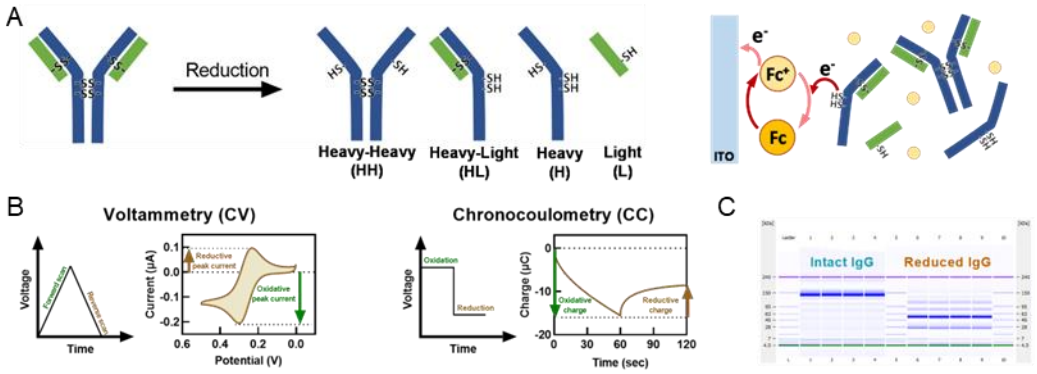

Figure 4.3 The structural reduction in the antibody and mediated redox measurement. (A) When antibody reduction happens, smaller compartments with free thiol groups are present in the samples. Redox mediator Fc works as a messenger that carries the

structural information correlated to the disulfide bond reduction to the ITO electrode and converts it into a digital signature. (B) CV provides a sweeping potential that covers the oxidation and reduction region while CC offers a step switching between constant oxidative and reductive potentials. (C) CE results confirmed the reduction of intact IgG with the generation of fully reduced heavy and light chains.

In the left panels of **Figure 4.4A**, we show the results of the CV measurement of Fc (50 μM) mixed with a range of IgG concentrations (0.25, 0.75, 1.5, and 3 mg/mL). Since this method measures the exposed biothiol level in the IgG sample, we observed that the Fc-mediated reduction and oxidation response from intact IgG samples remained unchanged across all concentrations evaluated compared to the control (50 μM Fc). However, when we applied the same measurements to the reduced IgG samples, we discovered redox cycling between Fc and the reduced IgG as noted by oxidative current amplification and reductive current attenuation at the peak potentials. At the same time, we discovered that both the increase in the oxidative current and the decrease in reductive current corresponded to the increase of total exposed biothiol content in the IgG samples. Upon comparing the ratio between oxidation and reduction peak currents, we observed that ITO's anti-biothiol fouling capability reliably discriminated the reduced components from the intact and control samples. In contrast, the performance of the system using a gold electrode was significantly suppressed by thiol-triggered nonspecific binding **Figure 4.2B**. The CC result demonstrated that by applying consistent oxidative and reductive potential for the same duration, we could better correlate the total content of free thiol group with the antibody level (right panels of **Figure 4.4A**). We observed that the ratio between oxidation and reduction charges formed a linear association with the concentration of reduced IgG. Meanwhile, as

expected, there was no significant difference between intact IgG and the Fc blank sample.

To acquire the structural integrity, measurements rely on the messenger (mediator Fc) carrying redox information from the free biothiol groups to the electrode. The transport is diffusion-based, and it becomes the rate-determining step in the measurement. Here, we investigated the impact of scan rate on the sensitivity and signal-to-noise ratio of free biothiol detection (**Supplementary Figure S4.3**). In brief, we observed that the increase in both reduction and oxidation peak currents directly correlated with the increase of the scan rate from 2 mV/s to 10 mV/s. However, when measuring reduced IgG, the oxidative peak current still dominated over the reductive peak current. Moreover, the oxidative/reductive peak current ratio reflected a reduction in the signal-to-noise ratio. We then tested the hypothesis that the mediator only accesses and reacts with the exposed thiol groups from the reduced antibodies, regardless of the sample's total concentration. To assess this, Fc (50 μM) was spiked into IgG mixed in the following ratios: 100% intact, 75% intact/25% reduced, 50% intact/50% reduced, 25% intact/75% reduced, and 100% reduced (total IgG concentration of 3 mg/mL for all samples). In **Figure 4.4D**, we found that the amplification on oxidative response and the attenuation on reductive response were free thiol concentration dependent. These data confirm that the loss of protein structural integrity due to the reduction of disulfide linkages can be converted into a convenient electronic signature. Meanwhile, without complicated surface modification and due to its anti-biothiol fouling characteristics, we showed that ITO can be a simple but effective electrode option for acquiring electrochemical fingerprints of the complex biomedical samples. Finally, we have

demonstrated that the rapid electrochemical access to free thiol sites on reduced antibodies exhibits analytical performance comparable to conventional chemical strategies. We employed Ellman's assay to verify the levels of free sulfhydryl groups in the reduced antibody samples, revealing a strong correlation between the exposed free biothiol levels and the concentrations of reduced antibodies (**Supplementary Figure S4.4**). As shown in **Figure 4.4E**, the results obtained from the electrochemical method on our ITO device (oxidative/reductive charge ratio from CC) were significantly correlated with those from the chemical method (Ellman's assay) across all tested concentrations. This finding suggests that, when paired with the ITO device, our mediated electrochemical platform offers a rapid, robust, and reproducible method for accurately representing reduced antibody information, essential for quality control in biotherapeutic development and biopharmaceutical manufacturing.

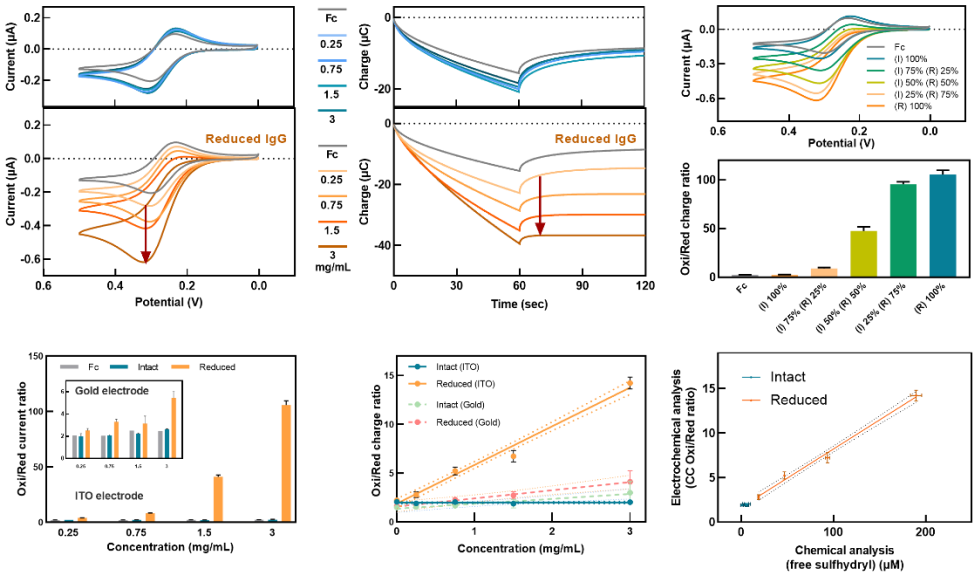

Figure 4.4 The measurement of reduced structure in the antibody via ITO electrode. (A) When testing reduced IgG, both CV and CC results show clear amplification on oxidative peak current and oxidation charge, with the attenuation on reductive peak

current and reduction charge. Meanwhile, both CV and CC show no significant difference between intact IgG and Fc. (B) The oxi/red peak current ratio demonstrates an obvious performance enhancement when using ITO electrodes. (C) The oxi/red charge ratio illustrates its capability to be used as an analytical indicator to quantify the total free biothiol in the sample when coupled with ITO electrodes. The results are compatible with the result from Ellman's assay. (D) The results indicate the specificity of the method for only accessing the sites with free thiol groups regardless to the sample total concentration. (E) The electrochemical assessment and chemical analysis demonstrated a strong correlation and comparable performance on free thiol detection. *(n = 3)

4.3.2 ITO-based operando technique for electrofluorochromic material characterization.

4.3.2.1 Controllable catechol electrofluorochromic hydrogel deposition.

Polyethylene glycol (PEG) is a widely used hydrogel material in pharmaceuticals[125], tissue engineering[126], and green chemistry[127] for its ability to work as supports and even catalysts. The formation of the PEG hydrogel starts from the polymerization of PEG monomers with reactive terminal functional groups such as thiolate PEG, amine PEG, and maleimide PEG. Previous research had demonstrated the strategy that induces polymer oxidation for crosslinking of thiolated PEG using redox mediators (e.g., pyocyanin (PYO)[40], catechol (CAT)[35,40], 1,1'-ferrocenedimethanol (Fc)[36], potassium hexachloroiridate (Ir)[36], and acetosyringone (AS)[35,36]). The polymer can be further functionalized depending on the mediators or doping materials to demonstrate unique optical signatures or electrochemical features. Mediators like catechol can not only be used to facilitate the monomer crosslinking process but also confer electrochemical/colorimetric features to the polymer. Catechol-based materials (e.g.,

catechol-chitosan and catechol-PEG) have been reported to have unique absorption at the UV-Vis depending on its oxidation/reduction status. However, the difficulty of applying optical measurement on traditional electrochemistry setups could be a barrier that hindrances the understanding of the function polymers. Here, thiolated PEG monomer was prepared in the buffer (100 mM PB) containing catechol to facilitate the polymerization by oxidizing the thiol groups at the terminal of the 4 arms in the monomer to form disulfide bonds. When an oxidative voltage was applied, the cross-linked catechol-PEG polymer formed a thin but uniform layer on the ITO electrode (**Figure 4.5A**). To further investigate the correlation between electrofabrication and catechol-PEG formation, we utilized the ITO device and deposited PEG (well No.1) and catechol-PEG (well No.2 to 4). We applied varying deposition times (30, 45, and 60 seconds) to wells No.2, No.3, and No.4, respectively. As illustrated in Figure 4.5B, the charge delivered from the electrode during the 30, 45, and 60-second intervals were 38 mC, 45 mC, and 57 mC, respectively. The thickness of the catechol-PEG hydrogel is highly correlated to the time the oxidative potential has been applied which is also proportional to the charge used by the catechol in the solution for monomer crosslinking. Together with the increase of the gel thickness, the darkening of the hydrogel also suggests that the functionalization of the catechol-PEG with the polymerization of melanin. Before reaching the gel thickness plateau, the color change of the catechol-PEG is attributed to both the degree of catechol polymerization induced by oxidation and the increase in gel thickness.

We then subsequently measured the absorbance spectrum as well as the fluorescence excitation and emission spectra using the ITO device docking station and a plate reader.

The UV-Vis spectra indicated that as the deposition duration increased, the absorbance increased across all scanned wavelengths. Notably, we observed a significant absorbance increase in the region between 400 nm and 500 nm, suggesting an increase in the number of oxidized catechol molecules[40]. Meanwhile, we found the material also demonstrates unique fluorescent signature. The fluorescence spectrum reveals that catechol-PEG exhibits an excitation peak at 436 nm and an emission peak at 516 nm. This suggested that catechol-PEG is not only electrochromic but also electrofluorochromic. Next, we placed the docking station under the fluorescence microscope for both colorimetric and fluorescence imaging. All four wells can be visually monitored and evaluated simultaneously. We noticed that the darkening of the gel and the fluorescence intensity were both highly correlated to the thickness and the brown color of the catechol-PEG within window of 30 second to 60 second of electrofabrication (**Figure 4.5C**). Meanwhile, as the negative control, the PEG hydrogel exhibited undetectable color change or fluorescence.

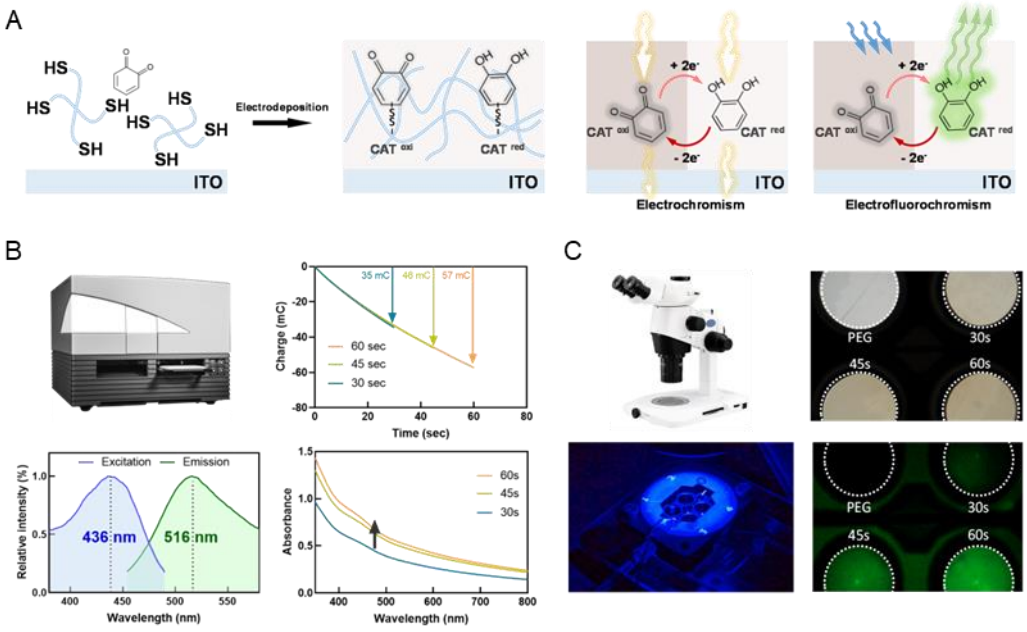

Figure 4.5 Catechol-PEG and its electrochromic and electrofluorochromic characteristics.

(A) Catechol played two important roles in the formation of this functionalized biomaterial. The oxidative power provided from the ITO was delivered to the thiol terminals via catechol diffusion. Catechol also covalently conjugated to the PEG network which further functionalized the hydrogel. The catechol polymerization also enabled the electrochromic and electrofluorochromic features that allow the color and fluorescence change corresponding to the redox state of the material. (B) The increase of UV-Vis absorbance aligns with the increase of deposition charge. Catechol-PEG has an excitation peak at 436 nm and an emission peak at 516 nm. (C) The color and fluorescence across all tested groups could be simultaneously monitored under the microscope. The functionalized catechol-PEG shows clear difference compared to the PEG control.

4.3.2.2 Optical signatures of redox-active catechol-PEG hydrogel.

As demonstrated in the previous articles [27,31,39,40], the optical properties of the catechol moieties of the catechol-conjugated hydrogels vary with redox state. Here, we characterized the optical responses (both UV-Vis absorption and fluorescence emission) depending on the mediators' redox-state switching. Specifically, we used a solution containing 2 redox mediators (0.2 mM of Fc and 0.5 mM of Ru) to switching the redox state of the catechol-PEG and collected time-dependent absorption at 480 nm and the fluorescence emission at 520 nm every 6 seconds as illustrated in **Figure 4.6A**. Here, we show the potential, scanning time, and absorbance and fluorescence for one cycle of cyclic voltammetry (CV) measurements, and these plots show that a pair of "peak and valley" are observed on both absorbance and fluorescence. The maximum absorption corresponds to most of catechol-PEG oxidation, while the minimum absorption corresponds to most of catechol-PEG reduction. In contrast, the maximum fluorescence corresponds to most of catechol-PEG reduction, and the minimum fluorescence corresponds to most of catechol-PEG oxidation (**supporting material Video 4.1**). The two profiles oscillated as one sine wave while another is 180 degrees out of phase, respectively. However, when the catechol was removed from the hydrogel (pure PEG hydrogel), we noticed the same absorbance and fluorescence oscillation also disappeared which indicated that the absorbance and fluorescence feature were mainly provided by the catechol groups that covalently conjugated to the PEG crosslinked backbone[31,40].

We further tested the material with cycling the applying voltage between a constant oxidative potential and reductive potential. In **Figure 4.6B**, we show the potential,

scanning time, absorbance and fluorescence for three cycles of cyclic chronocoulometry (CC) measurements. We noticed that the oxidation of catechol-PEG by Fc was amplified compared with its reduction by Ru. Here, we used a higher concentration of Ru (0.5 mM) to compensate for the attenuation. The plots show that the absorbance and fluorescence of catechol also oscillated with both turning points located at the time the potential switched (**supporting material Video 4.2**). The fluorescence image also indicated the maximum fluorescence appeared at the end of reduction period while the minimum fluorescence appeared at the end of the oxidation period. Compared with CV, CC switches between a constant oxidative potential and a reductive potential. This makes both colorimetric and fluorescent change to be more linear but limited by the diffusion of mediators. If we removed the mediators from the solution (pure PB), the catechol-PEG would not be able to change its redox state and lose its capability to change both absorbance and fluorescence. Overall, we found that the functionalized catechol-PEG has convincing redox-based optical features not only on UV-Vis absorbance but also fluorescence. The oscillations of both two optical signatures are 180 degrees out of phase from each other.

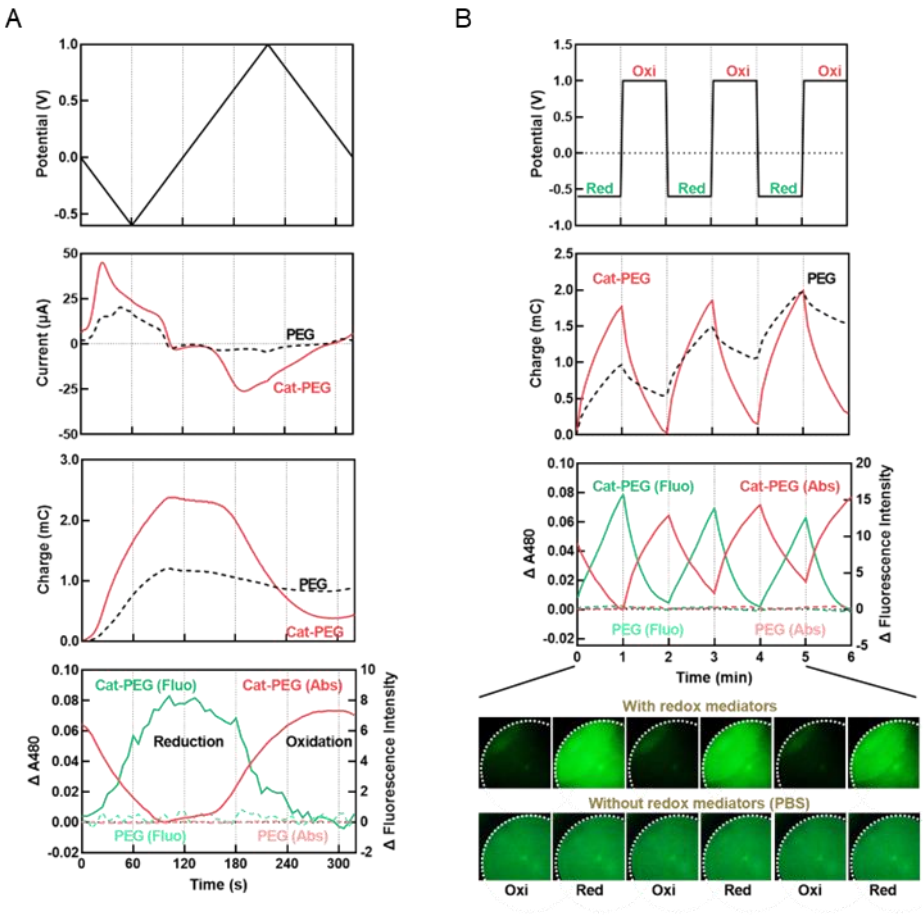

Figure 4.6 Characterization of catechol-PEG electrochromic and electrofluorochromic oscillation via ITO-based operando technique.

(A) Time series output curves for the response to the sweeping input potential for probing by a Fc-Ru mediator-pair. The UV-Vis absorbance and the fluorescence oscillated 180 degrees out of phase. (B) The fluorescent and colorimetric change when CC was applied. The repeating of the fluorescence response indicates that the catechol enables the electrofluorochromic characteristic.

4.3.3 Investigation of the oxygen depletion and electrogenetic induction in the functional artificial biofilm

4.3.3.1 Functional artificial biofilm fabrication

In the previously reported research [36], we found that a PEG-based cell artificial biofilm can be made on the electrode using mediated electrodeposition and the hydrogel microenvironment is highly biocompatible. We created the 'artificial biofilm' through electroassembly of the target cells with thiolated-PEG to form a cell-containing hydrogel. Specifically, the deposition solution was the mixture of cells (OD_{600} = 6) and thiolated-PEG monomers (50 mg/mL) with redox mediator Fc (5 mM). Then we added 100 µL of the deposition solution into wells of the ITO device and applied an oxidative potential (+ 0.8V) for 180 seconds on the working electrode which triggered the mediator-facilitated oxidation of thiol groups at the terminals of thiolated-PEG to generate the crosslinked network. Meanwhile, the cells in the deposition solution would be "codeposited" or immobilized in the formed hydrogel (**Figure 4.7**). The charge delivered from the electrode during the formation of the artificial biofilm across all wells stated consistent with the deposition duration (**Supplementary Figure S4.5**). After the gel formation, the uncured deposition solution was removed from the wells and the gel was rinsed with 1 mL of PBS twice. To "functionalize" the artificial biofilm, we engineered an *Escherichia coli (E. coli)* reporter cell (MJC683) has an extra copy of constitutively expressed *oxyR* (in addition to the one already existing on the genome) and expresses mScarlet-I fluorescent protein upon H_2O_2 induction (**Figure 4.7B**). The right panel of **Figure 4.7B** illustrates our hypothesis that locally generated H_2O_2 to trigger and activate the redox-responsive regulon *oxyRS* in MJC683. To verify this, we

also tested the H_2O_2 production capability using the ITO device (**Supplementary Figure S4.6**). Consistent with previous reports, the H_2O_2 production was stoichiometrically proportional to reduction duration and applied charge.

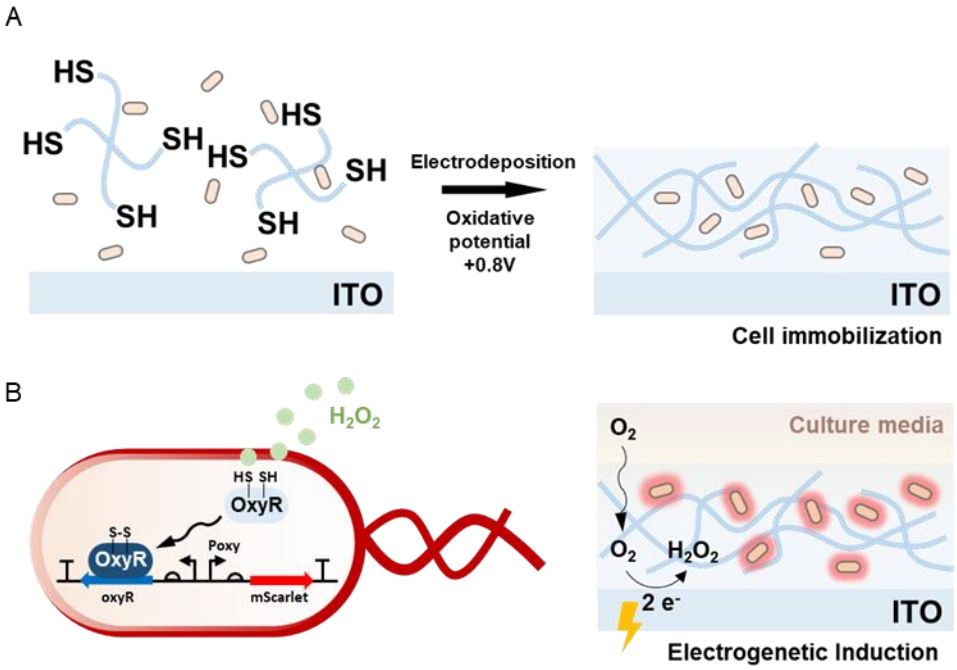

Figure 4.7 Mediated formation of artificial biofilm.

(A) Deposition solution containing selected cells (OD_{600} = 6), thiolated-PEG monomers (50 mg/mL) and redox mediator Fc (5 mM) was loaded into the wells. An oxidative potential (+0.8V) was applied to facilitate the crosslinking of disulfide bonds and further triggered the gel network formation and cell entrapment. (B) Engineered *E. coli* reporter cells (MJC683) that expresses mScarlet-I fluorescent protein upon H2O2 induction can be electrognetically induced.

4.3.3.2 Local oxygen depletion inhibits electrogenetic induction in the functional artificial biofilm

In the initial study, we confirmed in liquid culture that MJC683 is capable of expressing mScarlet-I fluorescent protein upon H_2O_2 induction (**Supplementary Figure S4.7**). For the artificial biofilm formation, the overnight culture of MJC683 was reinoculated in fresh LB media and harvested at OD_{600} = 0.3. The cells were then washed with PBS twice and concentrated for electrofabrication. The artificial biofilm was electrodeposited for 180 seconds, and 150 µL of the LB media was added to the well for cell culture. Confocal microscopy was used to record images, initial fluorescence levels, and fluorescence intensity three hours after induction across all tested groups. As illustrated in **Figure 4.8**, we tested five different conditions: (i) LB only (negative control), (ii) 200 µM H_2O_2 chemical induction (positive control), (iii) electrogenetic induction (-0.8V for 30 minutes), (iv) 200 µM H_2O_2 chemical induction with the presence of other cells in the culture media, and (v) electrogenetic induction (-0.8V for 30 minutes) with the presence of other cells in the culture media. We observed that the negative control had minimal fluorescence signals, while the group chemically induced by adding 200 µM of H_2O_2 exhibited significant red fluorescence. This indicates that the physical confinement of the cell in the PEG-hydrogel has inconsequential influence on cell induction and fluorescent protein production. We then applied a reductive potential (-0.8V) for 30 minutes to electrochemically produce H_2O_2 from the bottom ITO electrode. A similar fluorescent response was observed after three hours when compared with the positive control, indicating that the cells immobilized in the PEG gel can be electrogenetically induced and are capable of generating desired responses.

Notably, even if the total H_2O_2 generated from the electrode is not compatible with the amount added in the chemical induction group, the cells induced electrogenetically still produce similar levels of fluorescence signal. Terrell et al. previously demonstrated that the level of H_2O_2 on the electrode surface is significantly higher than the surrounding media[119]. When immobilized on the electrode surface, the cells can quickly expose themselves to the chemical microenvironment manipulated by the electrode. In other words, cell entrapment enables the opportunity to utilize localized oxidative chemicals and activate gene expression.

Furthermore, we introduced another engineered *E. coli* reporter cell line that constitutively expresses GFP (DH5α-sfGFP) to represent invading cells. In the presence of both 200 μM H_2O_2 and DH5α-sfGFP cells (OD_{600} = 0.3) in the LB media, we observed a significant reduction in the fluorescence response from MJC683. We hypothesize that, when proliferating, the green cells in the media rapidly consume the dissolved oxygen and generate a vertical oxygen gradient. The top green cells become a barrier, leading to the MJC683 cells constrained at the bottom of the device experiencing notable oxygen depletion. The lack of oxygen could contribute to the slowdown of gene expression and protein folding processes, resulting in a low fluorescence level. The DH5α-sfGFP cells could also uptake surrounding H_2O_2, leading to a reduction in H_2O_2 available for inducing MJC683 cells. Meanwhile, in the presence of DH5α-sfGFP cells (OD_{600} = 0.3) in the LB media, we once again applied a reductive potential (-0.8V) for 30 minutes to electrochemically produce H_2O_2 from the bottom ITO electrode. However, we observed a significant reduction in the current and charge representing oxygen reduction to peroxide (**Figure 4.9**). The recorded

reductive charges for the group with only LB media and the group with cells in the LB were 2.22 mC and 0.48 mC, respectively. Additionally, we observed a significant reduction in the fluorescence response from MJC683 after 3 hours. We hypothesized that the oxygen gradient generated along the vertical direction due to the presence of the DH5α-sfGFP cells inhibited the oxygen content and its transport to the electrode, leading to a reduction in peroxide production. Consequently, the reduction in cellular fluorescence response and gene expression was primarily due to the lack of peroxide production resulting from the decreased dissolved oxygen.

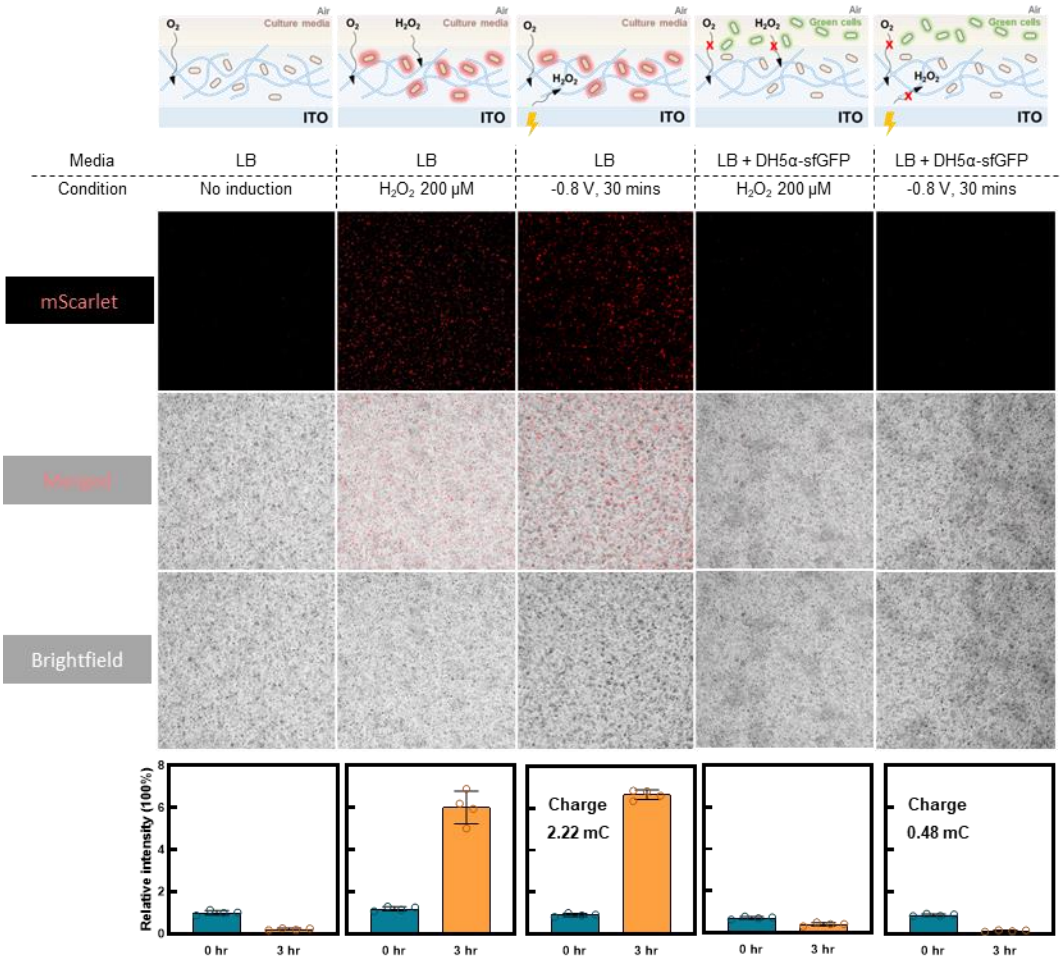

Figure 4.8 Local oxygen depletion inhibits electrogenetic induction.

With an artificial biofilm positioned atop the ITO electrode, we created an environment to investigate the correlation between vertical oxygen gradient, co-existing cells, and electrogenetic induction. In the absence of peroxide induction, the mScarlet fluorescence from MJC683 cells remained minimal. When chemically stimulated or electrogenetically induced, a strong fluorescence signal could be detected after 3 hours. However, when electrochemically induced in the presence of DH5α-sfGFP cells in the LB media, local oxygen depletion inhibited peroxide generation, leading to reduced mScarlet-I production. Additionally, when induced with peroxide addition, the DH5α-sfGFP cells consumed the H_2O_2 required for MJC683 cells, resulting in decreased gene expression. *(n = 4)

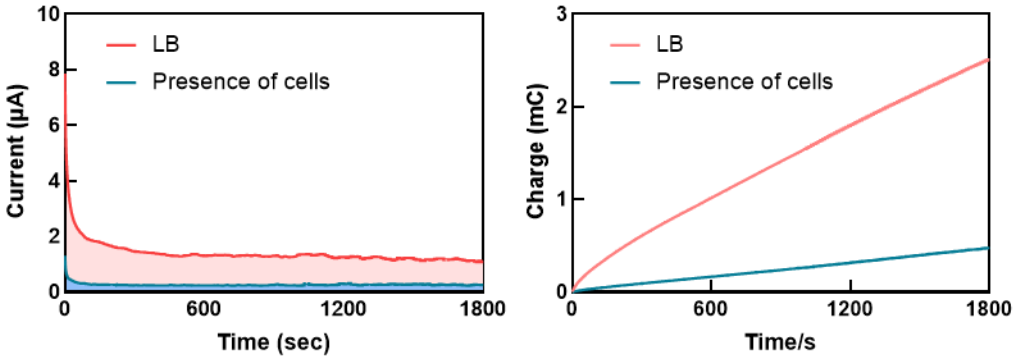

Figure 4.9 Fluorescence signal of MJC683 cell upon H_2O_2 induction.

A significant current and charge reduction was observed when other cells were presented in the LB media. The reduction represents the decrease of oxygen reduction to peroxide.

4.3.4 Supporting Information

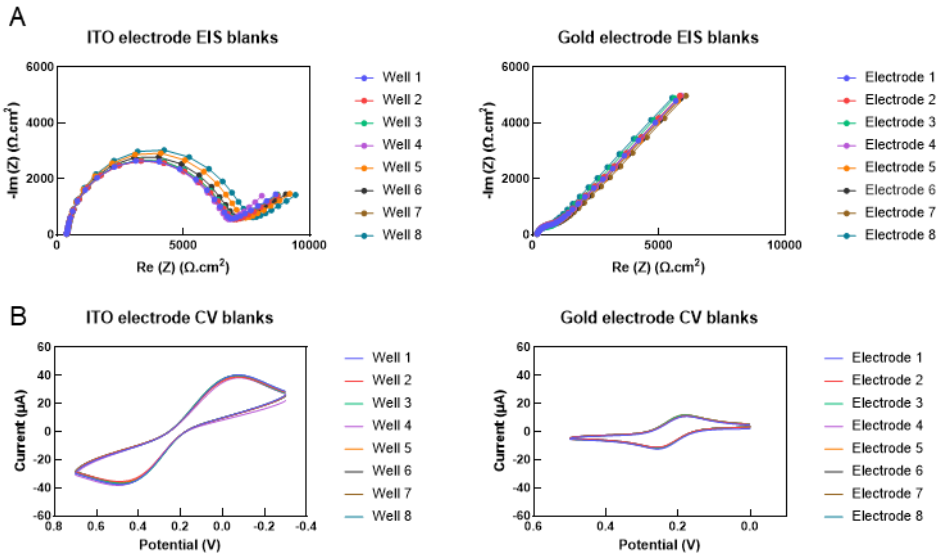

Figure S4.1. (A) Nyquist plots show that the impedance difference between the wells in the ITO device, and the gold standard electrodes is insignificant when tested using Ferri/Ferro solution. (B) CV plots also indicate that there is minimal difference between the electrodes.

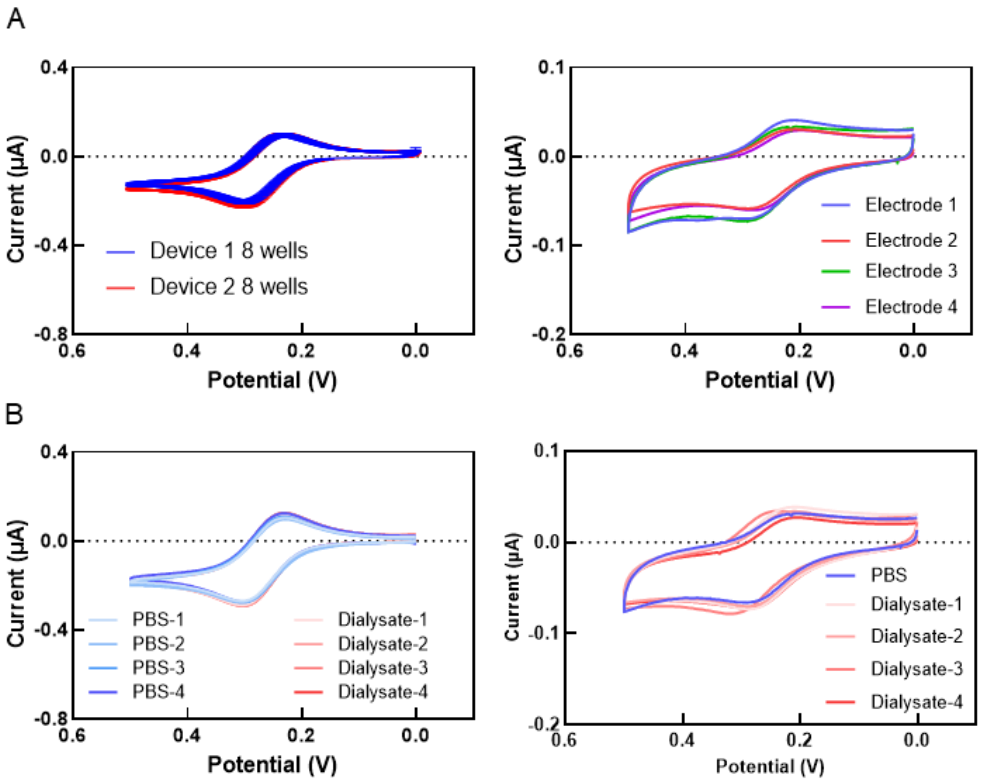

Figure S4.2. (A) CV plots show that the difference between the wells in the ITO device and different devices, and the gold standard electrodes is insignificant when tested using Fc solution. (B) CV plots show that there is minimal difference between the buffer control (PBS) and the dialysate samples (mixed with Fc) that were collected after the IgG purification when tested with ITO device and gold standard electrodes.

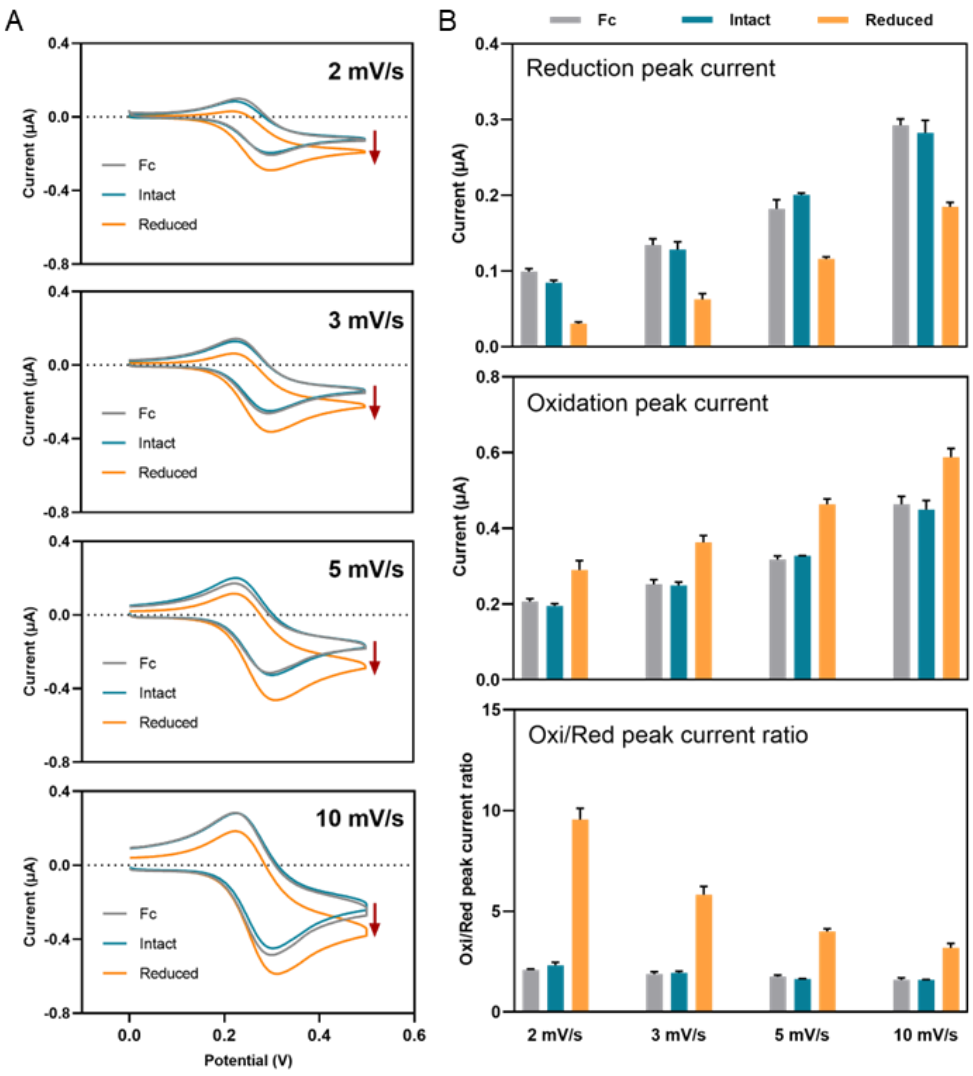

Figure S4.3. (A) The CV results show that the reduced IgG could be clearly distinguished from the intact IgG and Fc control across all scan rates tested (2, 3, 5, and 10 mV/second). (B) We demonstrate that the scan rate is tightly associated with both reduction and oxidation peak currents. Along with the increase in scan rate, bio reduction and oxidation peak current increase. However, the reduced IgG still contributed to the amplification in oxidation peak current and the attenuation in reduction peak current. Overall, the Oxi/Red peak current ratio shows a reduction in the signal-to-noise ratio when a higher scan rate was chosen. This is mainly limited by the mediator diffusion and reduction in interaction time with the thiol groups. *(n = 3)

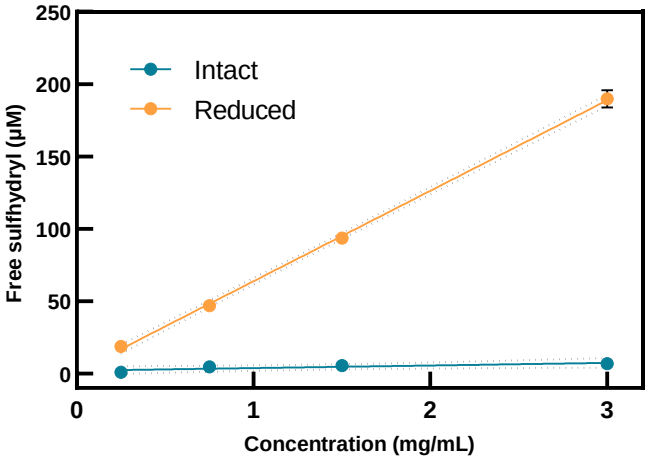

Figure S4.4. Ellman's assay results. The free sulfhydryl groups in the reduced antibody have a strong correlation to exposed free biothiol levels and the concentrations of reduced antibodies. *(n = 3)

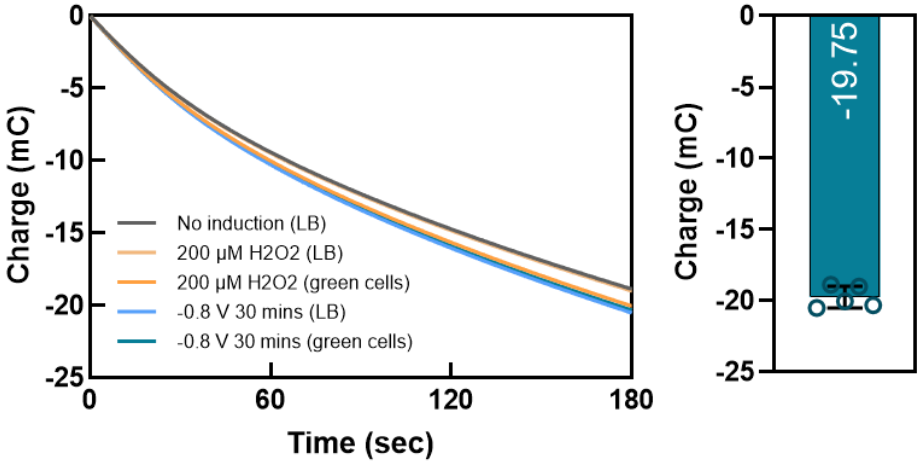

Figure S4.5. The charges for the artificial biofilm deposition across all tested groups. An average of charge -19.75 mC was recorded with a relative standard deviation (RSD) 3.87%.

$$\text{Relative standard deviation (RSD)} = \frac{Standard\ deviation}{Average}$$

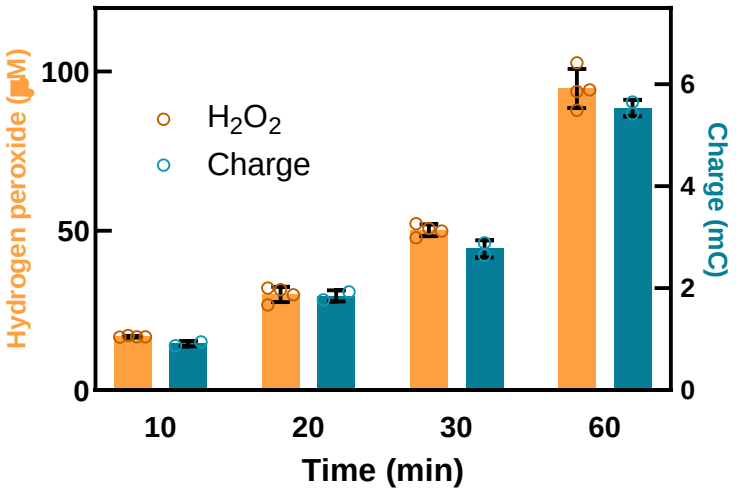

Figure S4.6. H_2O_2 production via from the ITO device.

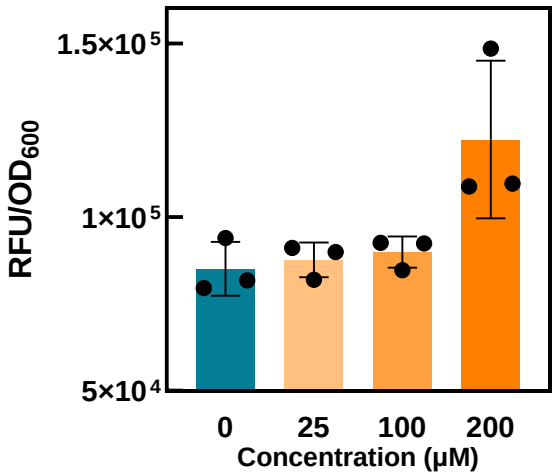

Figure S4.7. Fluorescence signal of MJC683 cell upon H_2O_2 induction in liquid culture. *(n = 3)

4.4 Conclusion

In this work, we first developed a simple, easy-to-fabricate 3D printed platform designed to establish a universal interface for high-throughput *operando* investigations

across a wide variety of samples. Leveraging the characteristics of additive manufacturing, we created a structure with multiple sample wells and a central salt bridge junction that enables simultaneous electrochemical measurements. Furthermore, the highly conductive and transparent ITO electrodes facilitate both *in-situ* and *operando* electrochemical assessments and optical evaluations of the samples. The connector and docking station serve as a standard port that enables bidirectional information exchange and provides the opportunity to utilize conventional, powerful analytical instruments. To demonstrate the potential of this concept, we explored three different applications, including (i) antibody structural integrity investigation, (ii) electrofluorochromic biomaterial characterization, and (iii) artificial biofilm electrogenetic induction.

In the first section, we demonstrated the anti-biothiol fouling capabilities of ITO electrodes. Traditional sensor interfaces often rely on surface modifications to enhance their ability to avoid nonspecific binding. Gold, as the standard and most popular material for electrodes, can be significantly influenced by the exposed thiol groups in biological samples containing proteins or antibodies. We showed that ITO exhibits extraordinary resistance to biothiol binding, making it an excellent material for biomedical purposes. When coupled with electrochemical analysis, we found that the amplified oxidation and attenuated reduction reactions of the mediator Fc can be used as an indicator for reduced IgG detection. The oxidative/reductive charge ratio also illustrates its capability to rapidly provide quantitative readings (2 mins) that are compatible with results from traditional assays. By avoiding complicated modifications

and enabling rapid testing of reduced antibodies, we demonstrate the potential of this device for use in biopharmaceutics, biomanufacturing, and biomedical tests.

In the second section, we demonstrated that a simple and inexpensive 3D printed device is capable of offering operando monitoring for electrofluorochromic material characterization. Unlike traditional operando techniques that rely on highly customized instrumental setups, we showed that the optical measurements of catechol-PEG hydrogel with simultaneous electromagnetic field changes can be easily recorded using plate readers and visualized via fluorescence microscopy. As a result, we reported the electrofluorochromic characteristics of catechol-PEG for the first time. We demonstrated the unique fluorescence excitation and emission spectra of this material and confirmed that the colorimetric absorption and fluorescence emission oscillate depending on the redox state of the catechol conjugated on the PEG backbone. Oxidation leads to the darkening of the material and quenching of the fluorescence, while reduction reverses its optical response.

Finally, we demonstrated the integration of bioelectronic systems with an electrogenetic framework. When coupled with redox mediators, a PEG-based artificial biofilm can be functionalized via engineered cells immobilized in this crosslinked network. As an example, we introduced two engineered cells, MJC683 and DH5α-sfGFP cells, which respond to peroxide by expressing mScarlet red fluorescence protein and constitutively express GFP, respectively. When immobilized in the PEG gel, we observed that MJC683 remained responsive and expressed mScarlet-I fluorescent protein upon H_2O_2 induction. Additionally, the reductive potential applied

to the ITO electrode was capable of accumulating enough localized peroxide to electrogenetically activate the oxyR promoter and generate the desired fluorescence response. However, when DH5α-sfGFP cells were present on top of the artificial biofilm, we observed a significant reduction in fluorescence signals from the MJC683 cells. The local oxygen depletion caused by the presence of other cells hindered both chemical and electrogenetic induction which provides hints to understand cell interactions in an electrochemically defined microenvironment. Here, we showcased the potential of this ITO device as an experimental platform for fundamental microbiology, as well as bioelectronics and biosensing applications.

Given the significant reduction in barriers to microdevice fabrication and the ease of customizing structural features afforded by 3D printing technology, we envision that the demonstration of this ITO device and docking system could serve as a foundation for the concept of using low-cost devices in a wide range of advanced bioelectronic, bio-optic, and biopharmaceutical applications. Ultimately, through standardization, open-source affiliates, and united communication protocols, we envision this approach to build a universal platform that shares digital signatures derived from nature with machines and humans.

Chapter 5

Mediated Electrochemistry Enables Redox-based Cross-species Assembly and Communication

5.1 Introduction

In 2019 alone, a staggering 4.95 million deaths worldwide were associated with antimicrobial resistance (AMR) by infectious syndrome, resulting in 189 million years of life lost. Researchers have reported that six pathogens each contributed to over 250,000 deaths per year globally, with *E. coli* responsible for the highest number of deaths attributable to AMR[128]. A strong correlation has been observed between the ability of bacteria to form biofilms and the prevalence of bacterial infections. These densely packed micro-communities primarily consist of a diverse range of extracellular polymeric substances (EPS), including polysaccharides, proteins, and DNA. These components create an interface that enables bacteria to proliferate in harsh surrounding environments[129]. Moreover, this protective barrier renders biofilms less susceptible to host immune responses and antimicrobial treatments.[130].

Investigating the microstructure of bacterial biofilms offers valuable insights into their mechanical properties and intercellular communication, significantly expanding our understanding of these intricate micro-communities. However, the complex process of biofilm formation that dynamically intervened by both intracellular and intercellular signals poses a fundamental challenge to studying them in their natural state[131–133]. The morphology and conformation of biofilms can vary dramatically between different

experimental setups. Consequently, there is an urgent need for a standardized experimental platform that provides a controllable microenvironment for biofilm development. Methods like electrostatic assembly[134] accelerate the accumulation of the cells while still relying on naturally secreted ingredients to establish the EPS. The biofilm is a highly hydrated microenvironment with its water content varying from 50% up to 95%[135], which makes hydrogels favorable materials to create artificial biofilms where high water content and robust mechanical properties are desired. To mimic the mechanical properties of biofilms, researchers have employed various hydrogel-bacteria mixtures, such as bacterial-chitosan constructs[136] and Ca^{2+}-alginate films[137,138]. When combined with techniques like electrochemistry, these artificial biofilms can be further functionalized for practical applications, such as monitoring water quality[139] and producing chemicals through CO_2 valorization[140]. Moreover, electrochemical analytical approaches offer stability and sensitivity, making them uniquely suited for investigating interactions between electrical interfaces and biofilms[141]. Electrochemistry, however, can be used as not only an analytical technique but also a fabrication technique.

Due to its capability to tailor the formation of desired materials, electrofabrication is an emerging biofabrication technique that offers complementary additive manufacturing capabilities for applications in the life sciences[142]. Mediated electrofabrication offers a rapid and controllable methodology to generate desired biomaterials. For instance, the mediator 1,1'-Ferrocenedimethanol (Fc) facilitates the crosslinking of PEG hydrogels through the oxidation of thiol groups in thiolated-PEG monomers, leading to the formation of disulfide bonds. Previous research has also

demonstrated that this process can be used as an effective strategy for cell entrapment or immobilization, offering precise spatial control of cells within a biocompatible hydrogel matrix, which is crucial for maintaining cell viability and functions[36].

In this study, we have demonstrated mediated electrofabrication of artificial biofilm with engineered *E. coli* reporter cells. Specifically, we utilize a previously developed ITO 3D-printed device that facilitates simultaneous electrochemical interrogation and optical assessment within a defined microenvironment. This approach allows for the visualization of cell behavior and distribution within the PET crosslinked structure. Moreover, we examined the role of the mediator Fc in the electrofabrication of artificial biofilms through the following steps: First, by investigating the oxidative potential applied to the ITO electrode, we demonstrate that the electroassembly process is robust and strongly correlated with the charge delivered to the system. At the optimal oxidative potential, we observe that the thickness of the artificial biofilm can be electrochemically adjusted. Second, the cells entrapped within the artificial biofilm exhibit a unique distribution, with cell density increasing gradually from the electrode surface until it reaches its theoretical density, followed by a decreasing slope at the biofilm-liquid interface. Third, we find that cell entrapment efficiency is dependent on mediator concentration. Our analysis reveals that the mediator concentration generally dictates the capability of gel formation; however, effective cell immobilization only occurs when an appropriate mediator concentration is present in the environment.

We further present a straightforward, tool-free approach for dynamically controlling cell distribution within artificial biofilms. Our findings indicate that gravity settling can

facilitate cell-cell interactions and initiate small aggregations, significantly altering cell distribution within the PEG network. Additionally, we demonstrate that electrofabrication allows for precise tailoring of the boundaries between two attached yet independent artificial biofilms containing distinct cell populations. Specifically, we introduce the "Deposit-Cure-Deposit" strategy to enable or disable the cell entrapment capabilities of the hydrogel. This approach facilitates the formation of a buffering zone or overlapping region between the two cell types, providing researchers with a method to precisely incorporate complexity into standardized *in vivo* models.

In summary, by combining a redox mediator with thiolated PEG, we demonstrate the broad capabilities of electrofabrication to create a robust and reproducible standardized microenvironment that simulates the densely packed micro-communities found in biofilms.

5.2 Materials and Methods

Materials

Indium tin oxide coated glass slide, square (surface resistivity 8-12 Ω/sq), and phosphate buffered saline (PBS, pH 7.4) were purchased from Sigma-Aldrich (St. Louis, MO). Black 3D printing resin was purchased from ELEGOO (Guangdong, China). 1,1′-Ferrocenedimethanol (Fc) was purchased from Santa Cruz Biotechnology (Dallas, TX). A 1 M stock solution of Fc was prepared in DMSO, and dilutions were prepared in PBS freshly for each experiment.

Device fabrication and performance check

The design and fabrication of the 3D printed 4-well device with ITO electrodes was previously described in chapter 2. In brief, the 3D printed device housing was assembled with the ITO glass with laser engraver electrode patterns to form the final test platform.

Cell culture protocol

E. coli reporter cells (DH5α-sfGFP or DH5α-dTomato) that can constitutively express high levels of sfGFP were cultured overnight in the Luria-Bertani broth (LB) in a 37°C shaker and the supernatant was removed (centrifuged at 3000 rcf for 10-15 mins) and the cells were washed twice with PBS and resuspended to the desired concentration in PBS before use.

Electrodeposition of PEG-SH and immobilization of Cells

Electrodeposition was performed using the designed 3D printed 4-well device with ITO electrodes and its docking station and performed with a CHI1040C electrochemical analyzer (CH Instruments; Austin, TX). 2X stock solutions containing 100 mg/mL PEG-SH with various Fc concentrations (1, 2, 4, and 10 mM) were prepared in 100 mM potassium phosphate buffer (pH = 7.4) and then mixed with 2X cell stock solutions prepared in PBS (OD_{600}=2, 6, 12) to form the final cell/PEG-SH/Fc solutions. 100 μL of the solutions were loaded into the wells and applied with constant voltage for varying durations (10, 20, 30, 45, 60, 120, and 180 seconds), unless otherwise noted. A constant voltage of +0.2, +0.5, +0.8, and +1.0 V, was applied to induce PEG-SH cross-linking for the test of potential optimization, and +0.8 V was used for the rest of the tests. The unreacted solutions were immediately removed from

the wells followed by 3 times of PBS rinse to remove residues. 100 μL of PBS or culture media were then added into the wells for the coming tests. Plate reader and confocal microscopy were then used for fluorescence measurement and the cell counts.

For the FITC-labeled thiolated-PEG and DH5α-dTomato cells codeposition test: 100 μL of the deposition solution containing 50 μg/mL of FITC-labeled thiolated-PEG and DH5α-dTomato cells (OD_{600}=12) was added into the wells. An oxidative potential (+0.8 V) was applied for 180 seconds to electroassemble the hydrogel. The unreacted solutions were immediately removed from the wells followed by 3 times of PBS rinse to remove residues. 100 μL of PBS was then added into the wells for imaging. Plate reader and confocal microscopy were then used for fluorescence measurement and the cell counts.

For the test of biofilm boundaries: 100 μL of the deposition solution containing DH5α-dTomato cells (OD_{600}=2 or 12) was added into the wells. An oxidative potential (+0.8 V) was applied for varying durations (30, 45, and 60 seconds) to electroassemble the 1st layer of hydrogel. The unreacted solutions were immediately removed from the wells followed by 3 times of PBS rinse to remove residues. 100 μL of PBS with or without 5 mM of Fc was then added to the well immersing the 1st layer of hydrogel. An oxidative potential (+0.8 V) was repeatedly applied for 30 seconds. The solutions were immediately removed from the wells followed by 3 times of PBS rinse. 100 μL of the deposition solution containing DH5α-sfGFP cells (OD_{600}=2 or 12) was added into the wells. An oxidative potential (+0.8 V) was applied for 120 seconds to form the 2nd layer of hydrogel. The unreacted solutions were immediately removed from the wells

followed by 3 times of PBS rinse to remove residues. 100 μL of PBS or culture media were then added into the wells for the coming tests. Plate reader and confocal microscopy were then used for fluorescence measurement and the cell counts.

Cell imaging and fluorescence detection

The device was examined with the Zeiss Axio Observer Z1 confocal fluorescence microscope (Carl Zeiss AG, Jena, Germany) for imaging or inserted into the TECAN Spark plate reader (Tecan Group Inc.; Männedorf, Switzerland) with the docking station for fluorescence measurements. The images were processed using ImageJ and Lightroom (Adobe, Mountain View, CA).

5.3 Results and discussions

5.3.1 Cell immobilization and entrapment on PEG-based artificial biofilm.

Initially, we investigated the correlation between oxidative potential and artificial biofilm morphology (gel thickness and cell distribution). Here, to deposit the cell-containing artificial biofilm, we suspended engineered *E. coli* reporter cells that constitutively express GFP (DH5α-sfGFP) (OD_{600} = 6) into a deposition solution (50 mg/mL thiolated-PEG, 5 mM Fc) and applied with a range of oxidative potentials (0.2, 0.5, 0.8, and 1.0 V) to trigger the disulfide crosslinking. We also tested two deposition duration (60 seconds and 180 seconds) across all evaluated potentials. We then used a confocal microscope to evaluate the gel thickness and cell distribution in the hydrogel. As shown by the representative composite fluorescence images (**Figure 5.1A**), no cell was detected in the group using an oxidative potential at 0.2 V regardless of the deposition duration due to the issue of forming an effective crosslinked structure. The

charge recorded from the electrochemistry analyzer also confirmed that 0.2 V could not provide sufficient energy density and trigger the oxidation of the mediator-facilitated crosslinking reaction. Meanwhile, when the oxidative potential was raised to 0.5, 0.8, and 1.0 V, we detected the fluorescence from the entrapped cells in the PEG networks. As illustrated in **Figure 5.1B**, we also noticed that the density and distribution of cells stayed consistent across all the groups with oxidative potential above 0.5 V with the same deposition duration. The same charge accumulating profiles along the gel forming process remained aligned across all tested oxidative potential above 0.5 V, suggesting that the rate-determining step of the could be the diffusion of the Fc and its interaction with thiolated-PEG but not the oxidative potential provided by the electrode. To ensure the gel formation, 0.8 V was chosen as the oxidation potential for the later tests. Interestingly, we monitored that the cell distribution in the artificial biofilm is a bell-like symmetric distribution. The peak of the cell distribution sitting at the middle of the PEG gel. This may suggest that the crosslinking process of the mediator-facilitated cell-hydrogel codeposition is an overlapping of several dynamic and progressive curing steps. Overall, this provided a digital-based methodology to precisely control the features of this living material on ITO electrode.

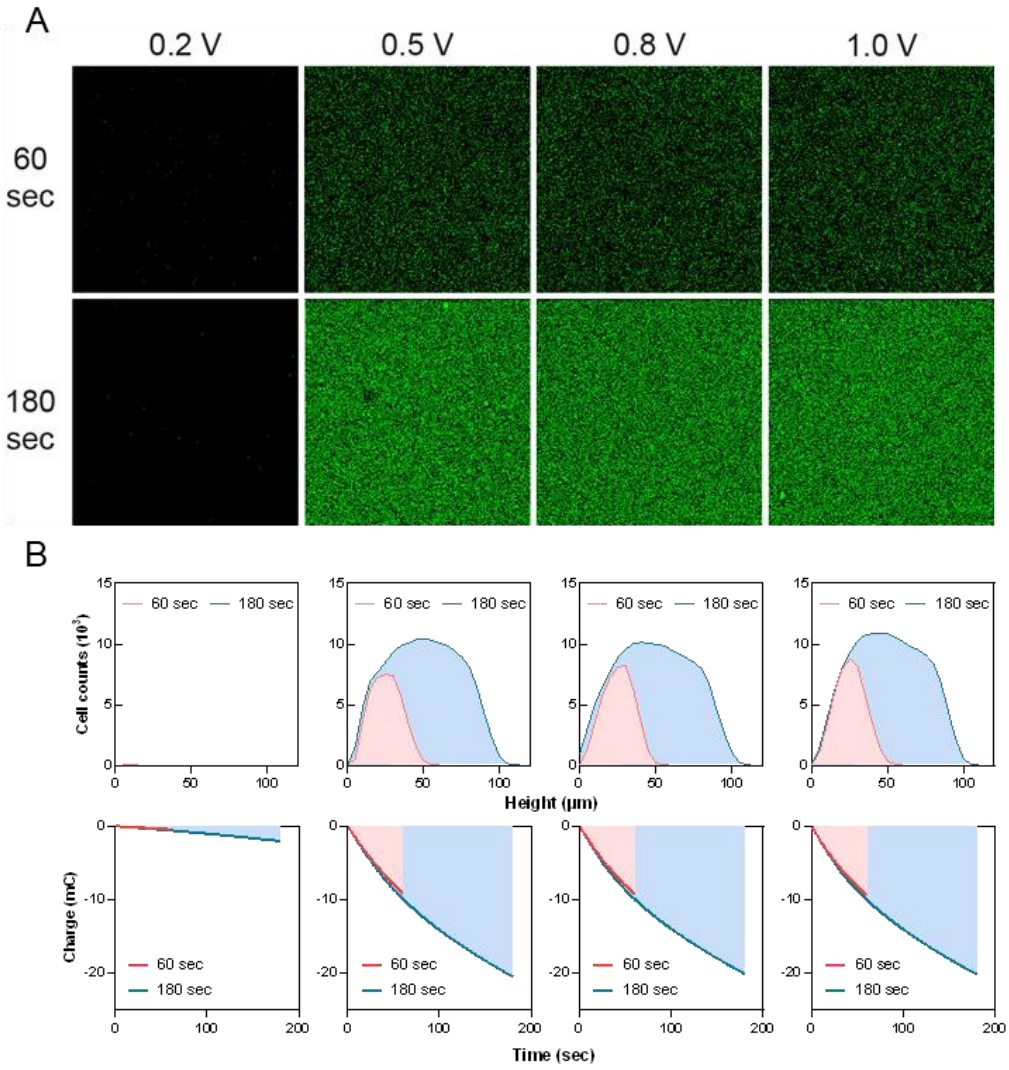

Figure 5.1 Mediated cell entrapment.

Fluorescence top-view images acquired by confocal microscopy enable visualization of entrapped cells in the gels. (A) Several oxidative potentials (0.2V, 0.5V, 0.8V, and 1.0V) were tested for cell entrapment. The results indicate that oxidative potentials above 0.5 volts provide similar cell entrapment capabilities. Fluorescence images show that cells immobilized in the PEG gel demonstrate comparable uniformity and density for all groups with potentials above 0.5 volts at different oxidative periods. (B) Cell counts per 5-micrometer slices acquired using confocal microscopy also reveal that the numbers and distributions of trapped cells in the PEG gel are highly correlated to the charge applied to the ITO electrodes. When the oxidative potential does not reach the

voltage that effectively facilitates mediator and thiol group oxidation, low charge and no cells can be observed due to the absence of a crosslinked network.

5.3.2 Cell distribution and its correlation with the controllable electrobiofabrication.

In our initial studies, we have conferred an optical signature to our assembled artificial biofilm by immobilizing fluorescent cells in the network using PEG-polymerization. Furthermore, we have investigated the correlation between charge, mediator transport, and cell distribution using confocal microscopy, owing to the remarkable optical accessibility from the ITO electrode. Specifically, 100 µL of the deposition solution containing DH5α-sfGFP cells (OD_{600} = 6), thiolated-PEG (50 mg/mL), and redox mediator Fc (5 mM) was added into an ITO device with 4 identical wells. Then we followed the previously established protocol and applied +0.8 V to the ITO electrode for a variety of time (10 to 180 seconds) to form the PEG gel. When imaging from the bottom of the device, we could compress the optical signals across the entire gel into one image which helped us to convert trapped cells information into optical signals (**Figure 5.2A**). Next, we quantified the fluorescence intensity using two methods: (i) fluorescence microscopy image processing, and (ii) plate reader measurement. Specifically, we utilized ImageJ to analyze the confocal images and quantify the "brightness" of the image as a representative fluorescence intensity of the hydrogel. In parallel, we placed the device on the docking station and used a plate reader to measure the fluorescence signals across 24 evenly distributed points on the hydrogel, averaging the fluorescence intensity for the gel. As illustrated in **Figure 5.2B**, we observed that the fluorescence intensities reported from both assessments demonstrated a strong linear correlation with the deposition durations, with R^2 values calculated for image

processing and plate reader measurement at 0.9732 and 0.9933, respectively. Additionally, we evaluated the correlation between the optical information acquired from the two different methods (left panel of **Figure 5.2C**). The reported intensities generally formed a positive linear correlation but could be broadly distinguished into two regions, separated at 45 seconds. The results indicated that confocal image processing could more effectively capture and quantify fluorescence signals when cell numbers were low, while the plate reader could capture overall optical signals from the gel when cell density reached a certain threshold. For convenience in measurement, we reported the fluorescence intensity recorded from the plate reader unless mentioned. The relative standard deviation (RSD) of cell fluorescence measured from the plate reader was calculated across all tested deposition durations (10, 20, 30, 45, 60, 120, and 180 seconds), yielding values of 2.97%, 16.51%, 11.16%, 5.66%, 11.94%, 2.39%, and 0.77%, respectively. The consistent fluorescence output was highly dependent on the charge applied to facilitate the hydrogel crosslinking process. As shown in the right panel of **Figure 5.2C**, the charge profiles across all 28 wells followed the same trend during deposition and reported an R^2 value of 0.9976 when fitted with a hyperbolic model. Together, our findings demonstrate a high degree of reproducibility of the artificial biofilm on the presented platform and setup, as evidenced by consistent charge, gel thickness, and fluorescence signal across all test groups.

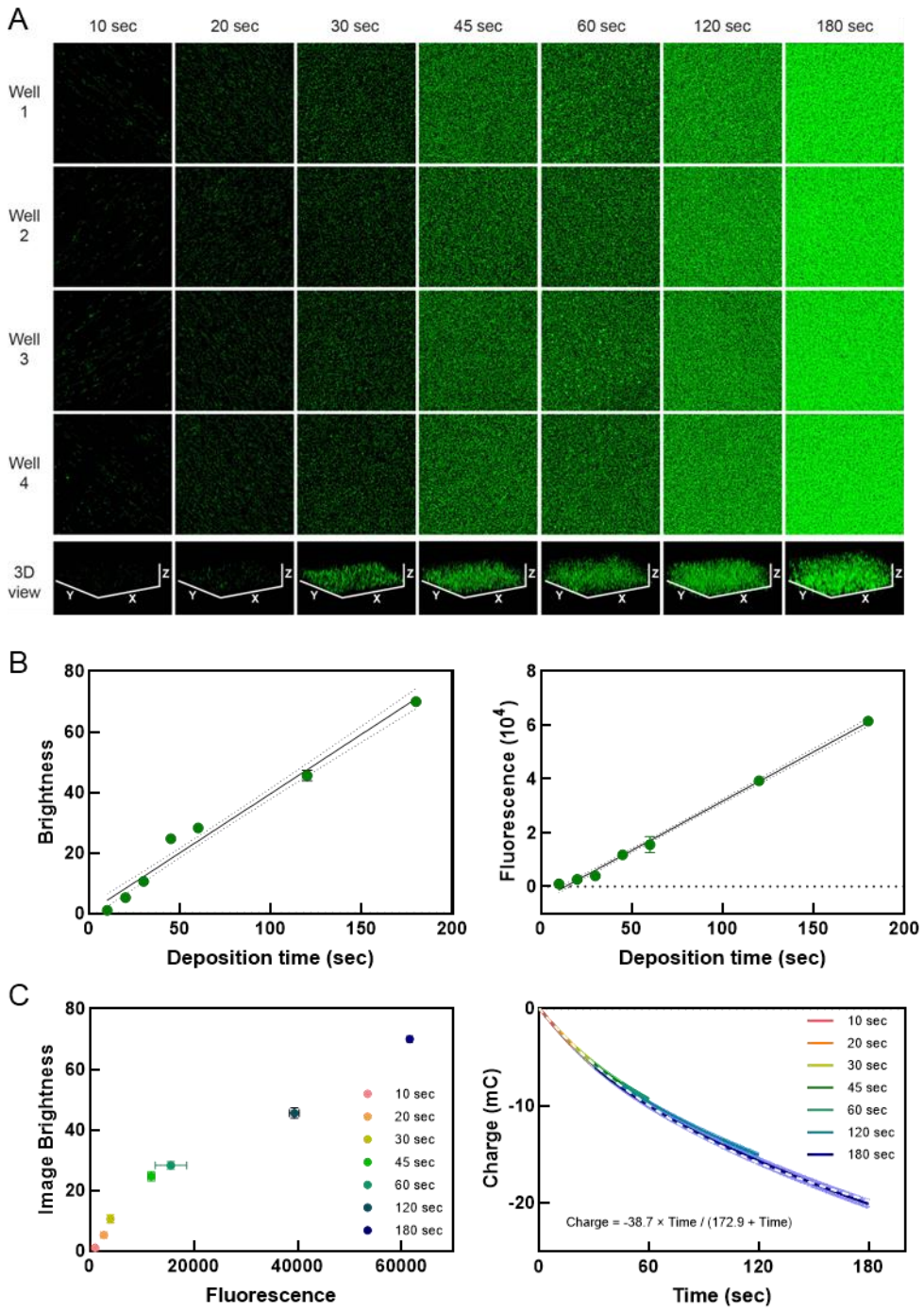

Figure 5.2 Cell uniformity in the PEG gel.

(A) All 4 wells on the device were tested using the same cell deposition solution (OD_{600} = 6, 5 mM Fc, and 50 mg/mL thiolated-PEG), and oxidative potential (0.8V) with different deposition periods (from 10 seconds to 180 seconds). The fluorescence increases are proportional to the total entrapped cells as a result of the increase of the

height/volume of the hydrogel. Showing convincing uniformities, the difference of PEG gel thickness, charge, and fluorescence reading across all wells are insignificant. Meanwhile, the cell distribution along the wells also shows high similarity. (B) Both results from fluorescence microscopy image processing and plate reader measurement demonstrate linear correlation with the fluorescence from entrapped cells. (C) The result demonstrates that fluorescence microscopy image processing offers better signal quantification when cell number is under certain level, while plate reader can better capture general signal when cell number is above. The charge profiles fit with a hyperbolic model and demonstrate good reproducibility. *(n = 4)

In **Figure 5.3**, we showed that the gel thickness significantly aligned with the deposition time and the charge delivered from the electrodes. However, an increase in gel thickness led to a decrease in gel thickness per unit charge, potentially owing to hindered mediator diffusion caused by gel formation. This, in turn, diminished the oxidation capability and gel crosslinking, as anticipated. Furthermore, the thickness of the gel exhibited a strong association with the entrapped cells and the resulting fluorescence. However, the fluorescence per unit charge appeared to be less influenced when a thicker gel was electrofabricated.

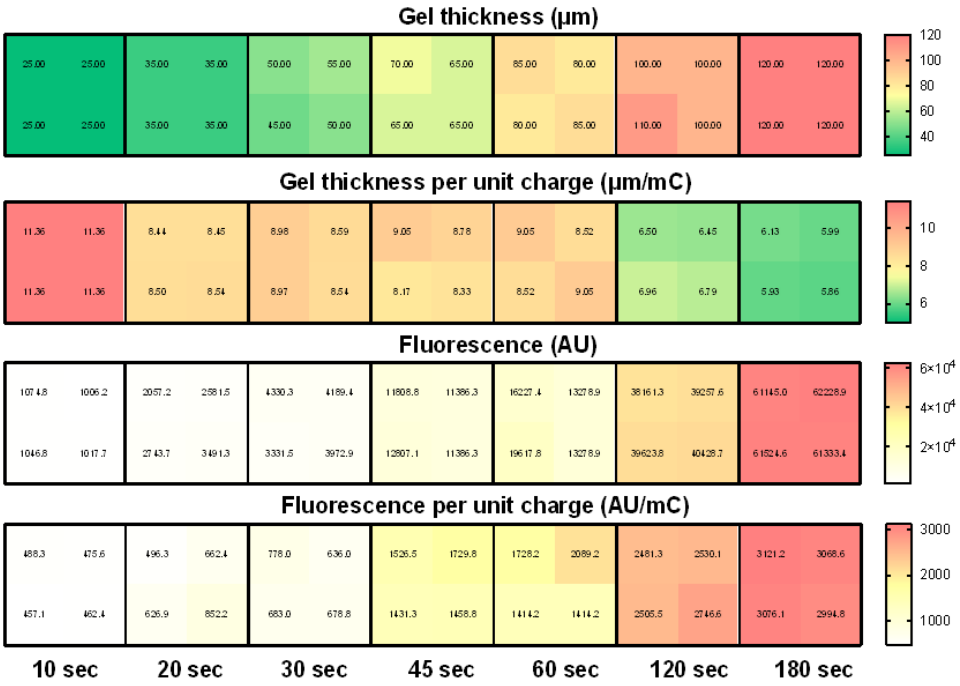

Figure 5.3 Time-dependent gel thickness and fluorescence change.

The gel thickness increase corresponds with the mediator-facilitated oxidation and its duration. It is also limited and controlled by the diffusion of Fc. A reduction in gel thickness growth rate indicates that the effective oxidative power carried by the mediator could be gradually attenuated during the transport.

By slicing the gel digitally using focal planes at a 5 μm interval, we investigated the cell distribution along the Z-stack (**Figure 5.4A**). In general, as reported in the previous session, the cells in the hydrogel exhibited a bell-like symmetric distribution along with the orthogonal axis. We found that the profile slopes at the region near the electrode were highly aligned across all tested durations. From the groups with short durations (30, 45, 60 seconds), we also noticed that more cells can be immobilized in those "unclosed" regions (where near the top of gels). Meanwhile, for the groups with the deposition time greater than 90 seconds, the cell density reached its plateau, and the

total cell number increase is directly proportional to the charge provided by the system. This phenomenon was observed because the theoretical cell density that could be provided from the deposition solution was reached. (8×10^9 cells /mL).

To confirm that the gel may be progressively "cured" by the redox reaction and the cell number is correlated to the gel density, we utilized cells that provided red fluorescence signals and green-fluorescent PEG gel to visualize the thiol oxidation and crosslinking. Specifically, we doped 50 µg/mL of FITC-labeled thiolated-PEG into the deposition solution and applied oxidative potential for 180 seconds. We also replaced the DH5α-sfGFP cells with DH5α-dTomato cells which constitutively express red fluorescent proteins for a better imaging quality. Again, confocal Z-stack images were taken to evaluate fluorescence signals and cell counts every 5 µm. Representative confocal images and plots are shown in **Figure 5.4B** and **Figure 5.4C**. As the green fluorescence increased, so did the cell count, as expected. The two factors demonstrated a high correlation across all heights measuring from the electrode surface locating at the bottom of the well. The FITC signal served as an indicator of the crosslinking level of the PEG matrix, since this fluorescent tag partially anticipated the crosslinking process and replaced some of the "nodes" between the monomers. Together, the results indicated that (i) the formation of PEG polymer is closely associated with its cell entrapping capability, (ii) the multiple oxidations may be necessary to fully "cure" this structure, and (iii) the "unclosed" regions with exposed reduced thiol terminals could potentially entrap more cells within the network.

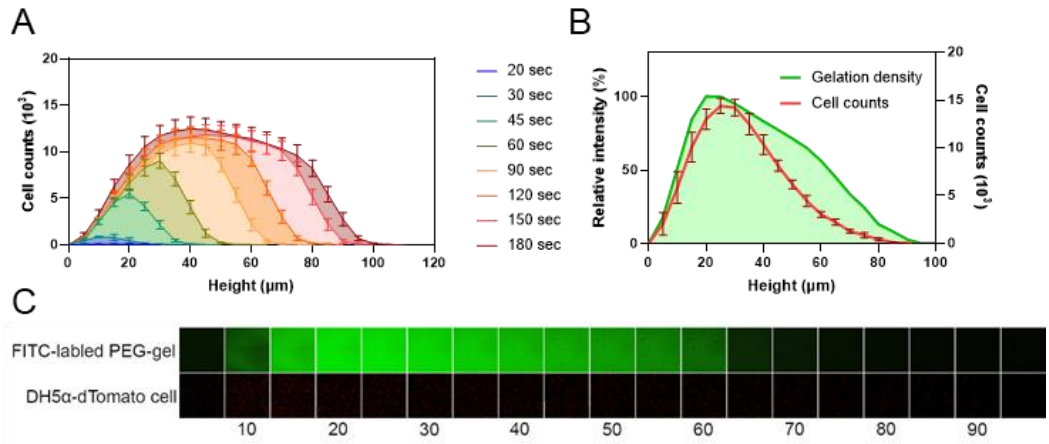

Figure 5.4 Cell distribution in artificial biofilm.

(A) Along with the increase of the oxidation and crosslinking process, the peak height (X-axis) and the peak of cell density (Y-axis) both shifts. For the group with short oxidation durations (20, 30, 45, 60 seconds) The cell number in the hydrogel is contributed by both the increase in gel thickness and the cell number per unit height. When the theoretical cell density is reached, the growth of the entrapped cells is mainly contributed by the increase in gel thickness. (B) The doped fluorescent thiolated-PEG monomers play as an indicator of the crosslinking process simply via its partial involvement to the reaction. The fluorescence profile quantified from confocal Z-stack images shows that the entrapped cell number per unit height can be correlated with the formation of disulfide bonds and the PEG network. (c) Imaged from the bottom of the ITO electrode, the crosslinking level and cell number can be visualized. The low fluorescence at the top region of the hydrogel indicates that the formation of a fully cured hydrogel may require multiple oxidations. *(n = 4)

5.3.3 The correlation between cell density, deposition duration, and mediator content.

The formation of the PEG-based artificial biofilm is directly related to the oxidation of the thiol terminals and the functional properties are dependent on the entrapped cells. However, the result of mediated electrodeposition could vary due to the change of several general factors (e.g., electrode conductivity, concentration of the mediators, the

crosslinking duration, initial cell density, etc.). In general, the factors that could change the redox state of the microenvironment may contribute to the artificial biofilm formation to varying degrees. Here, we verified the hypothesis that the mediator diffusion and the oxidation current density should be the main factors that direct the PEG-gel formation and its ability to immobilize cells. To assess, Fc with varying concentrations (0.5, 1, 2, 5 mM) was added to 50 mg/mL of PEG deposition solution containing DH5α-sfGFP cells with the following concentration: OD_{600} =1, 3, and 6. The solutions were then loaded into the wells of the ITO device and then followed by electrodeposition (0.8 V) for different durations (10, 30, 60, and 120 seconds). We then removed uncured deposition solutions and thoroughly rinsed the wells three times with 200 µL of PBS. Again, confocal microscopy was used to evaluate the gel thickness and cell content. The boundary of gel was defined by last slice in which cells can be clearly identified from Z-stack images, and the thickness was defined by the distance between the electrode and the boundary. We overlapped all the Z-stack images into one top-view image to illustrate the fluorescence level in each case (**Figure 5.5A**). We also quantified the fluorescence intensity of the artificial biofilms using plate reader coupled with the ITO device docking station. Representative charge, thickness, and fluorescence intensity plot are shown in **Figure 5.5B**.

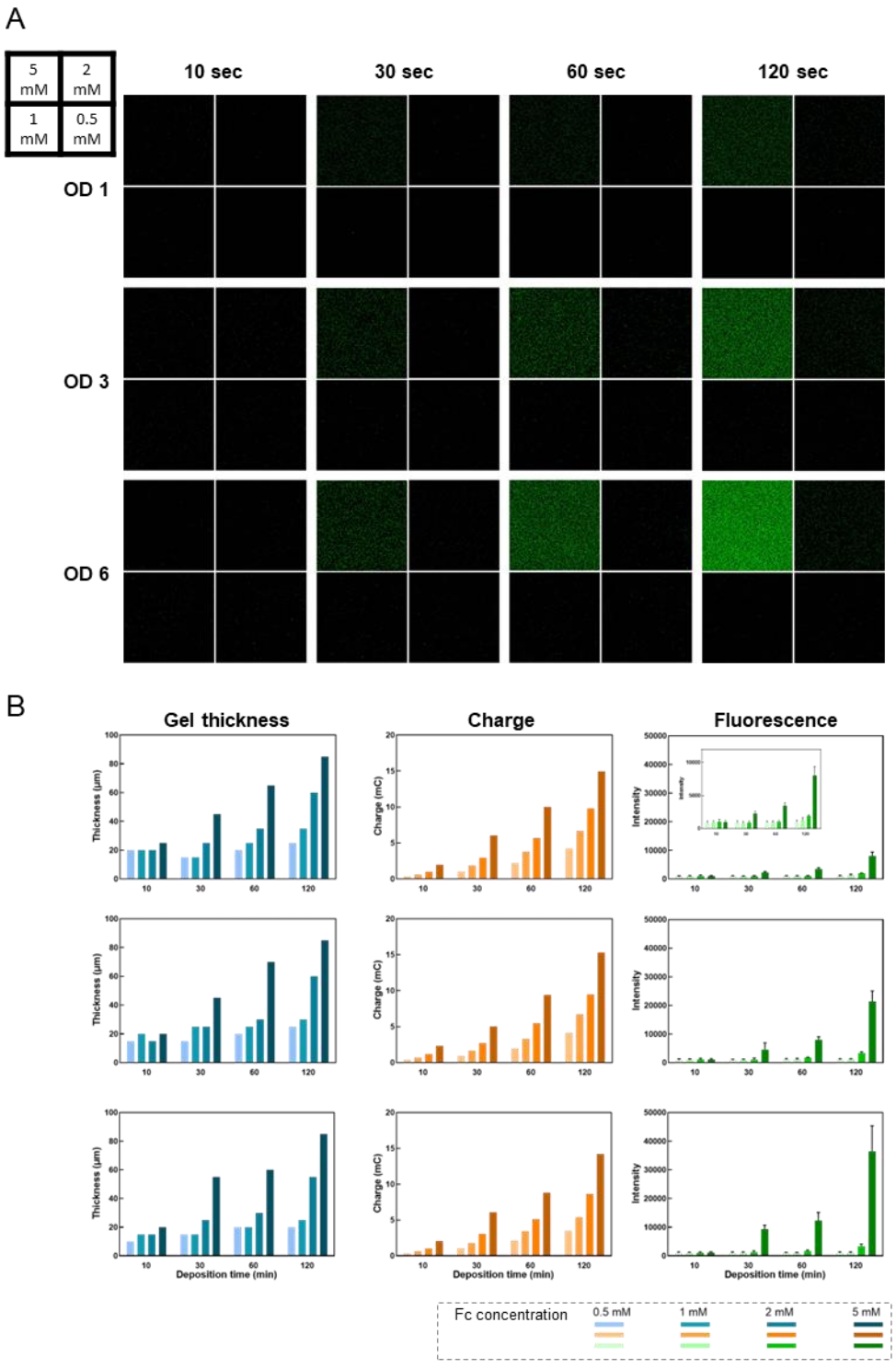

Figure 5.5 Mediator concentration and its cell entrapping capability.

Here, we investigate the cell immobilization capability of this system. (A) Various Fc concentrations (0.5 mM, 1 mM, 2 mM, and 5 mM), cell densities (OD_{600} =1, 3, and 6)

were tested with different gelation durations (10, 30, 60, and 120 seconds). Fluorescence top-view images acquired by confocal microscope enable the visualization of the entrapped cells in the gels. Strong fluorescence can be found in the group treated with 5 mM of Fc. Weak fluorescence can be observed in the group using 2 mM of Fc for a longer deposition duration. However, no obvious signal can be found in all groups with 10 seconds deposition. (B) The results showed that the gel thickness was highly correlated to the charge applied to the electrode across all groups. However, the correlation between entrapped cell numbers and the charge together with gel thickness seemed to be insignificant. With lower mediator concentration, long oxidation could bring better entrapment efficiency, while with high Fc concentration, the gel thickness, cell numbers, and the fluorescence expressed became significantly correlated in all initial cell densities and deposition times.

As the duration of deposition and the concentration of Fc increased, the accumulated charge was proportionally multiplied, as anticipated. Meanwhile, the correlation between charge and the PEG-gel thickness only seems to establish a strong association with Fc concentration over 2 mM. An example of this phenomenon can be observed in the fact that, despite three sets of conditions (specifically, 1 mM Fc for 120 seconds, 2 mM Fc for 60 seconds, and 5 mM Fc for 30 seconds) yielding comparable charge values (5.39 mC, 5.138 mC, and 6.08 mC, respectively), the efficiency in constructing the PEG gel varied significantly among these conditions (**Figure 5.6A**). This finding reinforces the idea that the effectiveness of the crosslinking process is strongly tied to the amount of oxidative energy delivered within a given timeframe.

It is noteworthy that the charge and gel thickness do not appear to confer reliable cell immobilization capabilities in cases where mediator content is low in the system. Our observations indicate that effective electrodeposition of cells was only possible at the

highest Fc concentration (5 mM), and fluorescence intensity only showed a linear correlation with the number of cells present in the biofilm when immobilization was successful. An illustration of this is the fact that although both sets of conditions (namely, 2 mM Fc for 120 seconds and 5 mM Fc for 60 seconds) resulted in comparable charge (8.649 mC and 8.832 mC, respectively) and near-identical gel thickness (60 μm), the level of effectiveness in immobilizing cells was significantly dissimilar (**Figure 5.6B**). During effective cell immobilization, the number of cells and fluorescence intensity in the artificial biofilm were found to be closely linked to the initial cell density in the deposition solution. This indicates that the duration of oxidation and initial conditions can be used to precisely control and define both the number of cells and overall cell response. Meanwhile, in this specific condition, the thickness was observed to have a positive correlation with the charge applied.

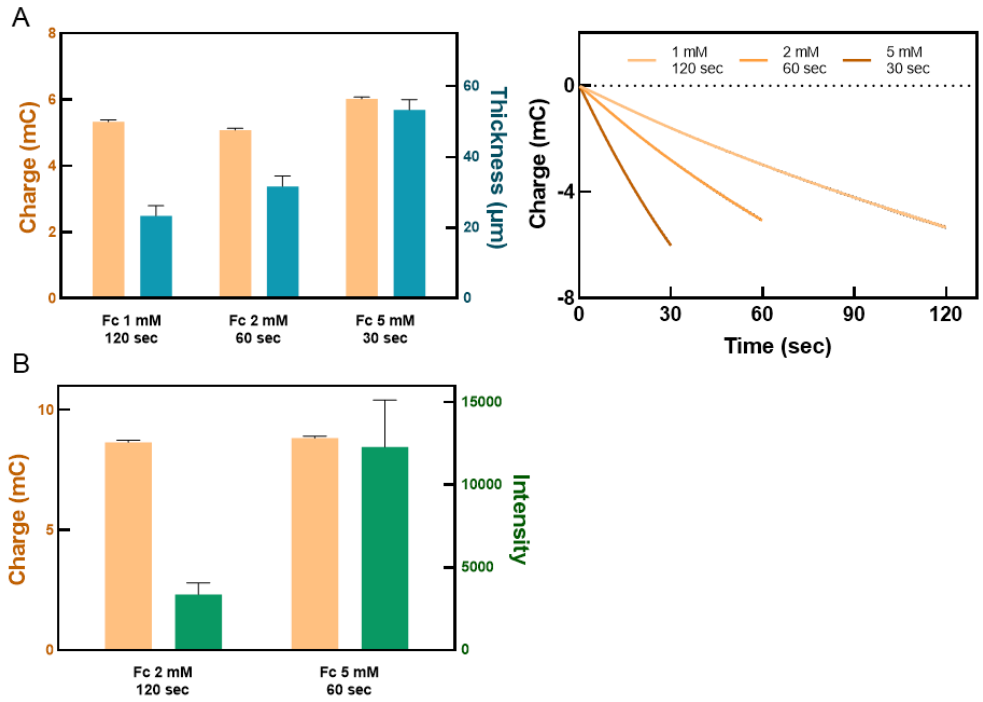

Figure 5.6 Charge and gel thickness and cell entrapment regulated by the mediator concentration.

(A) Three conditions resulted in comparable charge values (5.39 mC, 5.138 mC, and 6.08 mC, from left to right) but the thickness showed a significant increase when mediator concentration was higher than 2 mM. (B) The demonstrated conditions yielded comparable charges (8.649 mC and 8.832 mC, respectively) but providing a significant difference in fluorescence signal represents the cell number immobilized in the hydrogel. The data was adopted from Figure 5.4. *(n = 4)

5.3.4 Gravity-facilitated dynamic control on cell density in artificial biofilm.

In the previous sessions, we demonstrated that the initial cell density in the deposition is the primary factor that controls the final functional structure's cell density. Additionally, our results also indicated that the final cell density would be limited with short deposition durations. Here, we present a simple strategy that offers a rapid and tool-free methodology to dynamically control the cell distribution in artificial biofilms.

In the initial experiment, we examined two different settlement conditions in which cells were entrapped into a gel via PEG crosslinking either immediately after loading or 15 minutes post-settlement. We observed that, at a lower initial cell density (OD_{600} = 1), there was a tendency for more cells to accumulate at the bottom, with no significant change in cell density in the top region of the gel (**Figure 5.7A**). Further tests were conducted to determine the association between settlement and the cells distribution in the PEG network. The deposition solution with three different initial cell densities (OD_{600} = 1, 3, and 6) were tested. 100 µL of the samples were loaded into the device wells and settled on a flat surface at room temperature for various durations (5, 10, 20, and 30 minutes). When an oxidative voltage was applied for 60 seconds, the PEG hydrogel solidified and fixed the cell distribution within the matrix. Instant depositions were used as controls. As illustrated in **Figure 5.7B**, the fluorescence signal significantly increased due to the increase in entrapped cells within the same volume of gel. Similar results were observed across all tested conditions. This indicates that the natural settlement simply triggered by gravity can be used to control the dynamic distribution of cells. As shown in both bright-field and fluorescence images, we noticed that cell aggregation could be one of the factors that facilitate cell accumulation. The cells tended to move to their neighboring companions and form bigger clumps. With longer settling duration, the clumps further formed branch-like features and the phenomenon became more obvious when the initial density was high (OD_{600} = 6). To better correlate the optical signals and the cell distribution, we used a plate reader and confocal microscope to measure the overall fluorescence intensity and generate Z-stack images, respectively. As shown in **Figure 5.7C**, a 60 µm gel was generated across all

tested conditions (different OD_{600} and settling times). An obvious profile change exhibited after the settlement for over 10 minutes and a sustained growth on the peak height was also monitored. With 30 minutes of settlement, the group with low initial cell density (OD_{600} = 1) could entrap the same cell number as the group with high initial cell density (OD_{600} = 6) with instant deposition. Interestingly, it was noticeable that the settling of cells and the initial cell OD_{600} seemed to influence the charge output during the deposition process. For lower initial OD600, the system had a large charge output during the gel formation when the gel was instantaneously generated, which indicated that the cell density near the electrode may potentially involve the electron transfer or mediator diffusion. However, for test groups with settling process across all OD_{600}s with all durations, no significant charge shifting was monitored, and the value remained consistent. Importantly, this enables the tailoring of cell distribution in a well-defined artificial biofilm. Furthermore, the total cell number can be quantified using the area under curve (AUC) and we observed that the AUC formed a tight correlation with the fluorescence measured from the plate reader (Figure 5.8). After 30 minutes of settlement, the fluorescence signal increased by 175.31%, 716.86%, and 1132.45%, respectively across tested initial cell OD_{600} (1, 3, and 6)

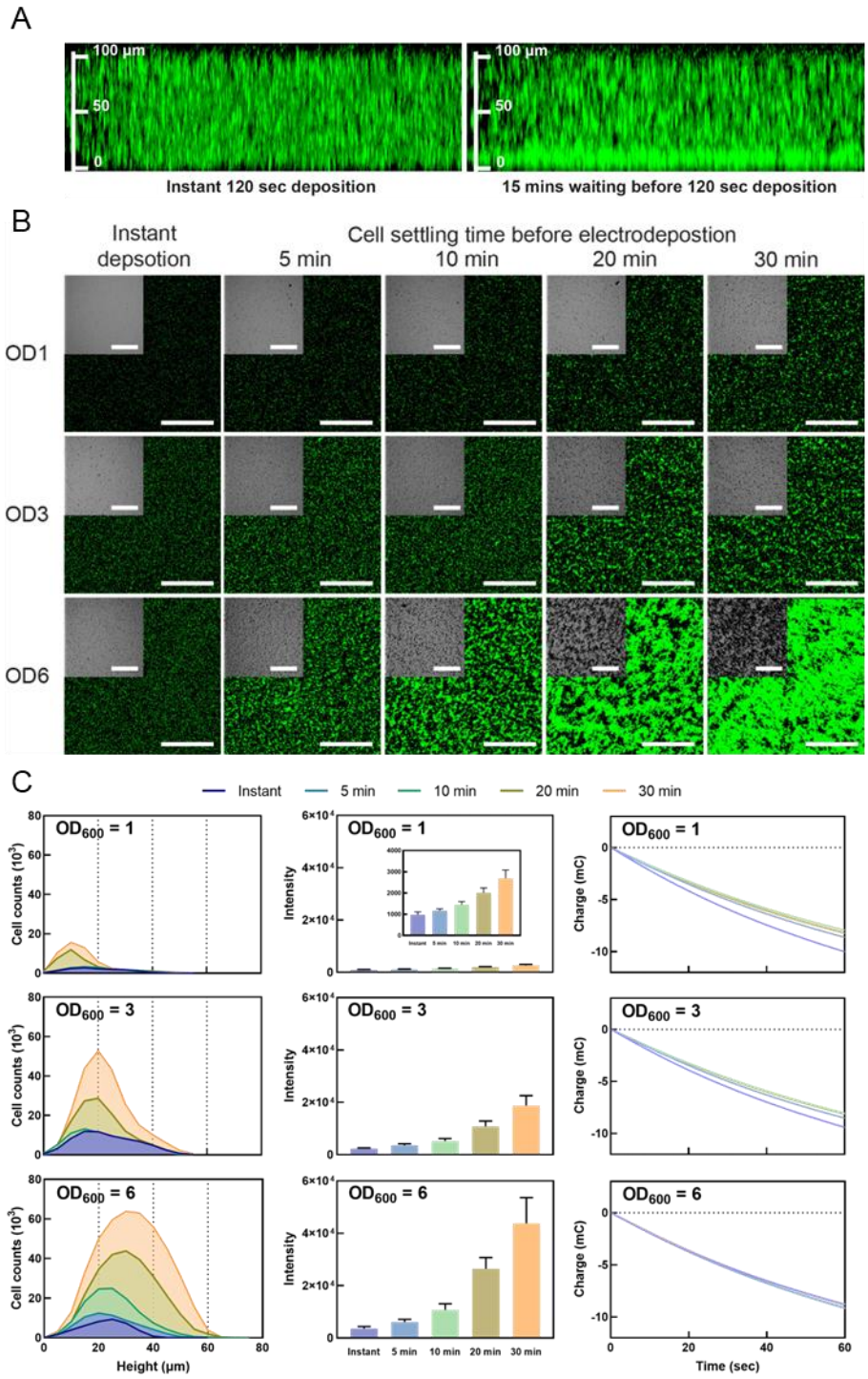

Figure 5.7 Dynamic manipulation of cell distribution in artificial biofilms via gravity. (A) Side-by-side comparison of confocal images for the two tested conditions. Left: instantaneous oxidative potential application for 120 seconds upon adding the

deposition solution to the well; Right: allowing settling for 15 minutes before applying the oxidative potential for a duration of 120 seconds. Both gels exhibited the same height, indicating that cell content did not participate in gel formation. However, a layer of cells with significantly higher density is visible in the image of the sample with a 15-minute settling period before deposition. (B) Bright field and fluorescence top-view images obtained by confocal microscopy show that the accumulation and aggregation of cells contribute to the increased cell content in the defined volume. The formation of small clumps or branch-like features by aggregated cells is dependent on initial cell density. (C) Cell distribution plotted from confocal Z-stack images reveals that cell accumulation is a time-dependent dynamic process. Cells tend to localize at the bottom when initial cell density is low, with the peak location remaining steady. In contrast, cells stack quickly and form a bell-like distribution with the peak shifting away from the electrode when the initial cell density is high. The overall fluorescence intensity quantified using a plate reader demonstrates that gravity-facilitated settling can significantly enhance the optical signal emitted from the entrapped cells due to increased cell density. *(n = 4)

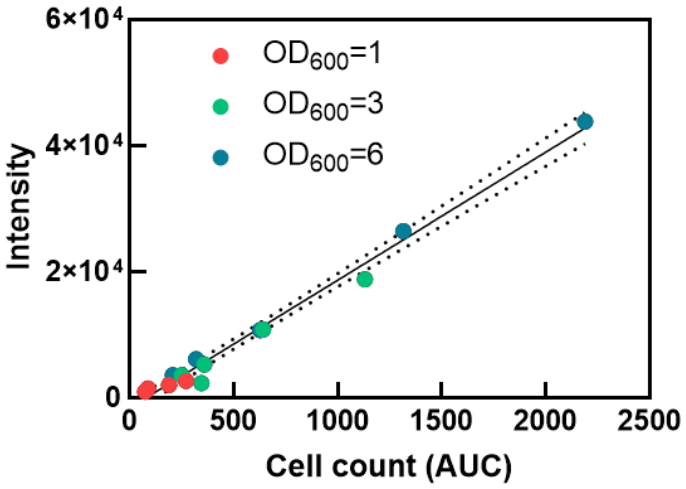

Figure 5.8 Correlations between fluorescence intensity measured from plate reader and cell counts in the artificial biofilm.

The intensity can also be correlated with the area under the curve (representing total entrapped cells). The plot illustrates a strong correlation between these two factors regardless of the initial cell density. The black line refers to the linear regression of all data points ($R^2 = 0.9864$).

5.3.5 Controllable artificial biofilm boundaries via redox manipulation of the active thiol terminals.

In this study, we aimed to test our hypothesis that the "unclosed" region (region with less crosslinking density) of the PEG artificial biofilm could potentially entrap more cells when a secondary deposition process is executed (**Figure 5.9A**). Specifically, we added 100 µL of the deposition solution containing constitutively red fluorescent DH5α-dTomato cells ($OD_{600} = 1$), thiolated-PEG (50 mg/mL), and redox mediator Fc (5 mM) into the wells of ITO devices. Following the previously established protocol, an oxidative potential of +0.8 V was applied to the ITO electrode to form the PEG gel. We constructed the first cell layer for 30 seconds and washed the wells to remove residue, filled the well with PBS, and applied the same oxidative potential for another 30 seconds. We then removed the liquid and refilled the well with 100 µL of the deposition solution containing constitutively green fluorescent DH5α-sfGFP cells ($OD_{600} = 1$), thiolated-PEG (50 mg/mL), and redox mediator Fc (5 mM) and generated the second cell layer using the same condition for 120 seconds. We repeated this step for a third cell layer with red fluorescent DH5α-dTomato cells for 60 seconds. Confocal images were taken after each wash step.

As illustrated in **Figure 5.9B**, we observed that the first deposition formed a solid layer of red fluorescent cells with a thickness (40 µm) and distribution profile consistent with previous reports. The second deposition successfully added green fluorescent cells on top of the first layer with red cells, creating an overlapping region between the two layers. The total thickness for both layers was recorded as 100 µm. Next, we observed that the third layer of red fluorescent cells formed a thin layer on top of the second layer but still managed to penetrate the top region of the second layer. This reinforces the earlier result that hydrogel formation is dominated by mediator diffusion, which limits the construction of the gel after reaching a certain distance threshold. The confocal results demonstrated the cell distribution across the three layers (**Figure 5.9C**). Three bell-like profiles were observed in the vertical direction from the bottom ITO electrode, with the second layer containing green fluorescent cells contributing the majority of the cell content. The starting point of the second layer lay at the peak of the first layer, confirming that cells can be entrapped in the "unclosed" region of the PEG artificial biofilm. The overlapping region is involved in both halves of the first and second layers. Meanwhile, the overall cell profile (all cells combined) exhibited a bell-like distribution, which again aligned with previous results.

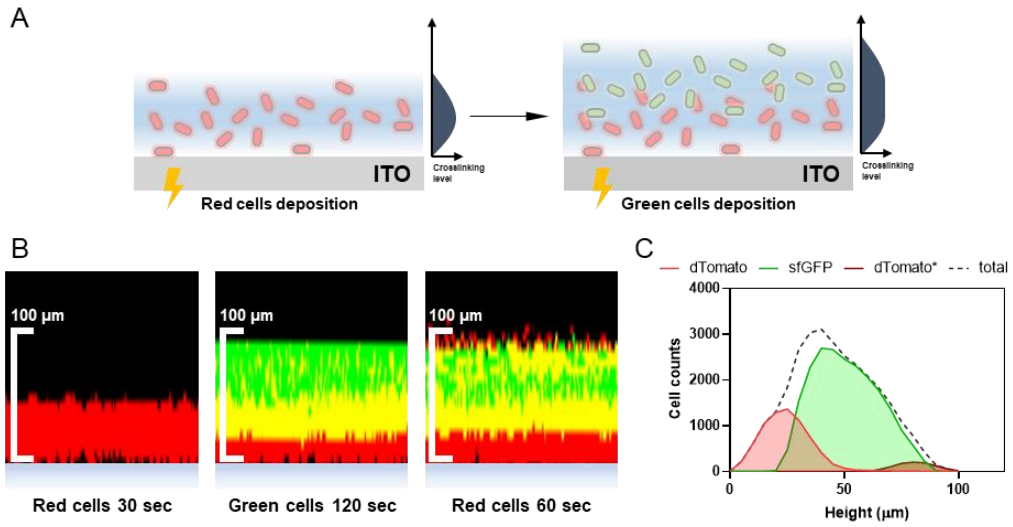

Figure 5.9 Electroassembly of multiple artificial biofilms.

(A) The second layer of cells overlaps with the first layer of cells, indicating that the remaining free thiolated terminals are capable of entrapping cells. The diffusion of the mediator limited the electroassembly of the third layer of cells. (B) Notably, the peak location of the cells suggests that the thiolated PEG monomers have fully crosslinked and cannot entrap additional cells.

Next, we assessed the "Deposit-Cure-Deposit" strategy for its ability to electrically modify the boundary formation between two artificial biofilms. Specifically, we followed the previous protocol to construct the first layer with red fluorescent cells (OD_{600} = 6) using various deposition durations (30, 45, and 60 seconds). However, we altered the wash step by replacing the PBS with PBS containing 5 mM of Fc (**Figure 5.10A**). Then, we immersed the gel in 5 mM Fc solution and electrochemically "cured" the first layer by applying oxidation for 30 seconds before depositing the second layer containing green fluorescent cells (OD_{600} = 6). As depicted in the left panel of **Figure 5.10B**, we observed significantly reduced overlap regions across all tested groups, with clear boundaries created due to the additional mediated oxidation between depositions.

We hypothesize that the curing process oxidized some of the remaining thiol groups in the PEG gel and crosslinked the monomers without entrapping cells, since cells were removed from the solution during the process. When the second deposition commenced, the green fluorescent cells were blocked and lost access to the top region of the first layer. Notably, the boundary location could be precisely controlled electrochemically by tuning the deposition time and its corresponding charges. As shown in the right panel of **Figure 5.10B**, the positions of the boundaries between the two cells across the tested groups (30, 45, and 60-second deposition for the first layer) were analyzed to be 48 μm, 52 μm, and 57 μm, respectively.

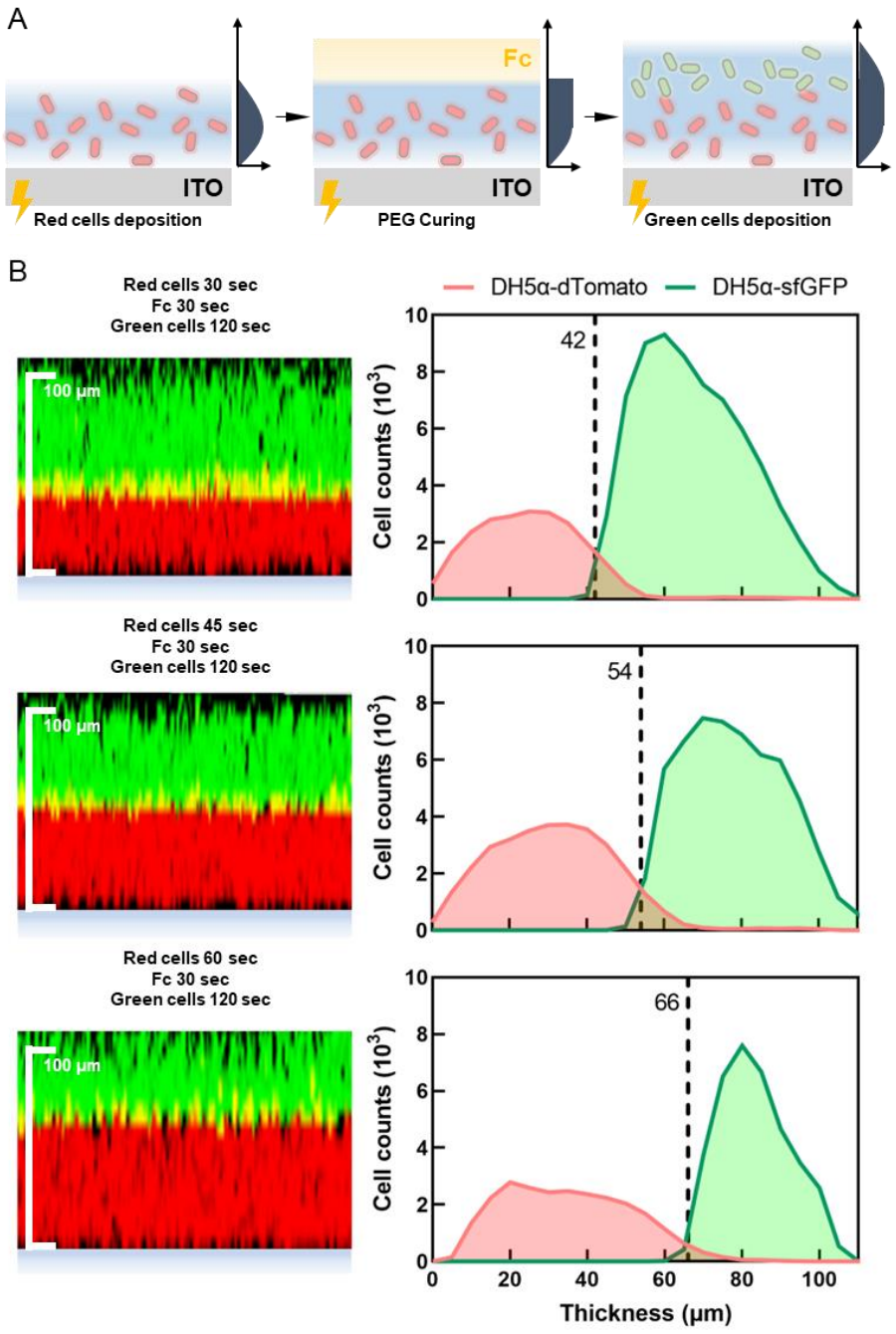

Figure 5.10 Controllable artificial biofilm boundaries.

Mediated with the Fc, an additional oxidative potential applied to the hydrogel between the deposition could electrochemically facilitated the crosslinking of free thiol groups and suppressed the capability of entrapping more cells during the second deposition process. The deposition time for the first layer determines the position of the boundary between two cells.

5.4 Conclusion

In this study, we have reported on the development of mediator-facilitated polymeric hydrogels that enable the generation and functionalization of artificial biofilms through engineered cells. We first investigated the mechanism of the crosslinking process via oxidation. Our results demonstrate that the formation of the PEG-based artificial biofilm is directly correlated with the mediator concentration and the chosen oxidative potential. This process can also be generally limited by the mediator diffusion which works as the messenger delivering the oxidative power from the bottom electrodes. In general, the charge delivered from the electrode represents the oxidative energy that triggers the crosslinking of the disulfide bonds. Nevertheless, the results illustrated that the oxidation density (oxidative power delivered per unit time) is the main factor that determines the successful cell entrapping. With an oxidation density overing the threshold, a significant positive correlation between cell number, optical signals, gel thickness, and the charge is generated. Additionally, evidence has shown that the final cell density may be limited with short deposition durations. Moreover, we have shown that the distribution of cells within the hydrogel is highly dependent on the crosslinking level of the hydrogel. The results confirmed that the gel formation requires multiple oxidations, which shows a dynamic range of capability for cell entrapment. In the "unclosed" regions containing active thiolated monomers, the potential for cell entrapment is determined by the amount of free thiol content left in the hydrogel.

We then demonstrated a straightforward, tool-free strategy that dynamically controls the cell distribution in artificial biofilms. The results indicate that cells have a tendency to form aggregation with the neighboring cells in the deposition solution. Meanwhile,

the natural settlement of the cell also creates a vertical gradient of cells from the bottom of the matrix. With low initial cell density, smaller aggregation forms. With high initial cell density, the small aggregation may further stack into a branch-like structure in the network. By utilizing the settlement, we are able to control the distribution and entrapment of the target cells which gives us more opportunities to better mimic the natural biofilm. These findings provide valuable insights into cell behavior within hydrogels and have significant implications for the design and optimization of biofabrication strategies.

Lastly, we employed the "Deposit-Cure-Deposit" strategies and successfully demonstrated the ability to spatially separate two cells in the artificial biofilm. Specifically, we showed that the boundary between two independent biofilms can be controlled by electronically disabling the free thiol terminals using mediated oxidation. This approach provides the opportunity to fine tune the buffering zone or overlapping region between the two cell types in the standardized *in vivo* models.

Overall, by advancing mediated electrofabrication that offers precise and controllable manipulation to defined microenvironment, we are in a better position to discover new insights on the complexities of the biofilm formation and intercellular communications. These will serve to better understand fundamental processes of communications between cells and molecular diffusion within the polymeric substances and at the same time, facilitate the development of new antimicrobials and therapeutic treatments.

Chapter 6

Summary and Future Directions

6.1 Summary

"This is only a foretaste of what is to come,

and only the shadow of what is going to be."

— Alan Mathison Turing (1912-1954)

If all biophysical and chemical interactions in nature could be described by numerous formulas, it would be highly probable for us to create a parallel virtual world. Similarly, if a synthetic model could accurately replicate every detail of the research target, ranging from human organs to individual proteins, we are very likely to discover solutions for the most challenging and complex diseases. However, similar to Internet of Things, before we can develop a representative model, we must enable the connections between compartments in varying length scales and facilitate communications in this network. Interfaces, meanwhile, become the key to establishing this network. It can be a common boundary of two bodies, spaces, or phases, such as cell-scaffold contact regions or the surface separating two artificial biofilms. It can also be a situation where two things meet and influence each other, such as redox information exchange between mediators and antibodies, or the conjugation of antibodies with capture elements. Of course, it's a connection between independent and often unrelated systems and communicate with each other. Examples include when excitations coming from potentiostat and the fluorescence microscopy meet at the electrofluorochromic materials, or when electrodes electrogenetic induce *E. coli* gene

expression. In this dissertation, we focused on aligning two emerging technologies — additive manufacturing and electrobiofabrication and demonstrate how these can initiate the formation of these meaningful interfaces and enable intercommunications.

In Chapter 1, we started by summarizing the progression of additive manufacturing and the working principle of two later elaborations of Stereolithography (SLA) known as "Direct Laser Writing (DLW)" and "Digital Light Processing (DLP)". 3D printing enables the creation of complex and intricate objects by depositing materials in a point-by-point, layer-by-layer manner. Prior to these advancements, a series of repeated steps involving material deposition, patterning, and subsequent removal from specific areas were frequently necessary to create the fundamental components required for the final assembly[143]. This transformation has substantially altered the manner in which 3D objects are created, as tasks previously restricted to specialists have broadened to encompass a more diverse group, including entrepreneurs, hobbyists, and potentially even children. In this dissertation, DLW was primarily used to depict the most delicate features on the villi scaffolds such as surface porosities and capillaries. DLP, on the other hand, was aimed to rapidly create desirable 3D functional structures such as villi sheet, multi-well spectroelectrochemical modules, and microfluidic systems. Next, we reviewed current approaches in electrobiofabrication.

Following the efforts that has been done in other gut-on-a-chip models, in Chapter 2, we evaluated the two main approaches in 3D printing — DLW and DLP and tested how they recapitulate the important features of human villi. Caco-2 cells were seeded on DLP 3D printed scaffolds, resulting in a viable cellular monolayer after 14 days.

This growth rate was comparable with that on cast PLGA 3D scaffolds. Importantly, the increase in surface area resulted in a higher overall cell number which potentially enabled a more realistic cell density in the space. That is, more cellular molecules can be generated and detected per base area. Next, by comparing the cell proliferation on bare and growth matrix coated scaffolds, we reported that the bare scaffold offered similar cell supporting efficiency to the coated setups. Targeting the ZO-1 tight junction protein, immunostaining exhibited that the epithelium tight junction was successfully formed after 21 days of culture. Next, a full-size intestinal villus was constructed using a two-photon DLW 3D printing system. Due to the size limit, segments were "stitched" together during the printing process and ultimately formed the final scaffold. With the capillary at the basolateral side of the scaffold, we enabled the fluidic transport across the crypt and tip region of the villus. This offers advantages in (i) sampling from a single villus while avoiding sample mixing commonly found in conventional 2D models; (ii) eliminating uneven diffusion patterns due to the thin fluid channels beneath the scaffold. The transparency of the printing material allowed for continuous visualization of cell growth. Similarly, we noticed that the cell covering the scaffold after two weeks, however, growth facilitating material may be suggested on this material (IP-S) to enhance the cell proliferation. Immunostaining, meanwhile, revealed that the epithelium tight junction was successfully formed 3 weeks after cell seeding. Finally, pressure-regulated cell assembly was also demonstrated, with negative pressure guiding cells to designated positions on porous 3D printed scaffolds. Overall, we demonstrated the feasibility of using 3D printing for the rapid development of

scaffolds comprising complex 3D geometries in organ-on-a-chip applications. As 3D printing technology evolves, we are eager to see it revolutionizing industries and enable

In Chapter 3, we detailed the development of a 3D-printed microfluidic device for rapid and high-throughput electrochemical interrogation of antibody titer and glycosylation. The 8-channel microfluidic device, featuring ITO electrodes and fluidic connectors, was fabricated using DLP 3D printing, enabling precise fluidic control and eliminating the need for manual processes. The device was capable of electroassembling thiolated PEG-based antibody detection interfaces, enabling the detection of a range of IgG concentrations. The system's matrix effect and interface regeneration were also evaluated, demonstrating potential for online operation and cost reduction. When coupled with the fluidic and electrical connectors, the device's "plug-and-play" modularity allowed for rapid replacement and module switching, offering potential solutions for multi-sample quality examination during biopharmaceutical production.

In Chapter 4, we focused on combining 3D printing and electrochemistry to develop a spectroelectrochemical modular interface enabling the connections with other advanced analytical assessments (e.g., electrochemistry analyzer, microscope, and plat reader). Multiple sample wells design enabled high-throughput interrogations, while the highly conductive and transparent ITO electrodes facilitated *in-situ* and *operando* electrochemical assessments and optical evaluations. To demonstrate the concept that this interface can offer the bidirectional information integration and facilitate the digitization of redox interactions, we explored three different applications, including (i) antibody structural integrity investigation, (ii) electrofluorochromic biomaterial

characterization, and (iii) artificial biofilm electrogenetic induction. We started by demonstrating the anti-biothiol fouling capabilities of ITO electrodes and their potential for use in biopharmaceutics and biomedical tests. The study revealed that ITO exhibits extraordinary resistance to biothiol binding, making it an excellent material for biomedical applications. As the result, we reported the electrical attenuation in the reductive region and amplification in the oxidative region are highly correlated to the free biothiol content in the sample. The device enabled rapid testing of reduced antibodies, providing quantitative and compatible readings in just 2 minutes. By avoiding complicated modifications and enabling rapid testing of reduced antibodies, we envision that this ITO interface with customizable 3D printed housing can enhance the development of protein-based therapeutics. Next, we exhibited the potential of a simple and inexpensive 3D printed device for *operando* monitoring of electrofluorochromic material characterization. The device enabled easy recording and visualization of the optical measurements of catechol-PEG hydrogel. The unique fluorescence excitation and emission spectra of the material were first reported, and its colorimetric absorption and fluorescence emission oscillation depending on the redox state were demonstrated. The ITO interface with high transparency significantly lowers the entry barrier of electrofluorochromic material characterization. Lastly, we investigated the integration of bioelectronic systems with an electrogenetic framework. By coupling redox mediators with a PEG-based artificial biofilm, functionalized engineered cells were immobilized in the crosslinked network. Importantly, we exhibited that the activation of electrical potential to the system does not promise the execution of electrogenetic induction. What is representative of the production of redox

active molecules is the output current and the accumulated charge. The study showcased the potential of the ITO device as an experimental platform for fundamental microbiology, bioelectronics, and biosensing applications.

Finally, we demonstrated that our spectroelectrochemical interface is capable of mimicking the densely packed micro-communities of bacteria biofilm in Chapter 5. Following the cell entrapment protocol, we hope electrobiofabrication can provide another option to set up a “standard” synthetic *in vitro* model of biofilm. Initially, we investigated the mechanism of the crosslinking process via oxidation and discovered that the formation of the PEG-based artificial biofilm is directly correlated with the mediator concentration and the chosen oxidative potential. Meanwhile, our results illustrated that oxidation density (oxidative power delivered per unit time) is the primary factor that determines successful cell entrapment. With an oxidation density above the threshold, a significant positive correlation between cell number, optical signals, gel thickness, and the charge is generated. Furthermore, we found that the distribution of cells within the hydrogel is highly dependent on the crosslinking level of the hydrogel. Next, the study also demonstrated a straightforward, tool-free strategy to dynamically control cell distribution in artificial biofilms by leveraging cell aggregation and gravity-facilitated settlement. Lastly, we employed the "Deposit-Cure-Deposit" strategies and successfully demonstrated the ability to spatially separate two cells in the artificial biofilm. This approach allows for fine-tuning the buffering zone or overlapping region between the two cell types in standardized *in vivo* models.

I personally really like what Dr. Shuler remarked, “These surrogate systems need not be perfect to have significant impact; just significantly better than animal studies and simple *in vitro* human studies.”[21] Analogously, inventions may not always closely resemble their natural inspirations. For example, while the concept of flight was inspired by birds and their ability to soar, modern airplanes have a starkly different appearance and functionality compared to their avian counterparts. The functional interfaces we have developed may not precisely replicate every detail; however, through the progressive achievements of interfaces at various levels, we envision that the efforts dedicated to advanced manufacturing and methodologies, which enable communication between humans, cells, molecules, and machines, will lead us to a better understanding of the complexities of unknown aspects of nature.

6.2 Future Directions

The systems presented in this dissertation hold significant potential for further applications that warrant exploration. In Chapter 2, we developed 3D printed scaffolds that facilitated the *in vitro* gut epithelium recapitulation. This work can be expanded through: (i) using new printing materials. Biocompatible materials such as PEG-DA, IP-PDMS, hyaluronic acid (HA), can be good candidates to establish the supporting structure for cells. (ii) printing scaffolds that mimic different organs or organelles. Good examples are Henle's loop in kidney, glomerulus in kidney, alveolus in lung, and lymph nodes. A common characteristic across these examples is that the tiny structure makes it difficult to reconstruct using conventional fabrication strategies. However, it becomes the opportunity for 3D printers such as Nanoscribe to faithfully reconstruct these delicate 3D morphologies *in vitro*. Together with the pressure-driven cell guiding

method, we should be able to build a protocol to anchor cells towards scaffolds with complex features. An interesting application or study that can be investigated using this technique will be cell migration and cell self-assembly in 3D environments. For example, different intestine cells have preference position to proliferate on the human villi. Enterocyte cells generally cover the entire villous surface but the crypt region; Paneth cells and intestinal stem cells significantly occupy the crypt region; Goblet cells, however, universally distribute across the entire vertical direction[144]. We may be able to generate a scaffold that has multiple internal channels that provide independent controls to specific regions at the scaffold (e.g., the tip, middle, and crypt regions). After selectively aligning chosen type of cells to the designed areas, we could then monitor if they have a tendency to initiate the re-orientation or migration to their favorable positions on the scaffold.

In Chapter 3, we showed a 3D printed microfluidic system coupled with electrochemical-based sensor interfaces for antibody detection. This work can be expanded by (i) optimizing the construction steps for the sensor interface formation. Parameters such as PEG deposition time, thickness, mediator concentration may be optimized to enhance the protein conjugation efficiency and signal/noise ratio; (ii) enabling optical detection. Owing to the transparency of ITO electrode, optical-based detection can be easily integrated to the system. Fluorescent targets such fluorescent proteins and fluorescent-labeled reporter molecules can serve as a secondary information source. Together with the electrochemical readings, we may promote the detection sensitivity and accuracy; (iii) developing upstream on-line cell separation system. Such microfluidic system with spiral microfluidic channels using inertial

sorting has demonstrated convincing CHO cell separation from the culture media[145]. By combining the upstream cell soring features, we envision the overall microfluidic sensing system holds significant potential for commercialization.

Next, we showcased three emerging topics in electrochemistry in Chapter 4 to demonstrate the capability of our multi-well spectroelectrochemical modular interface. Further study can start with expanding the available sample wells via an enlarged 3D printed housing and ITO electrode. The high-throughput and simultaneous detection can significantly amplify the information density which reduces the operation time and labor. Meanwhile, since samples can be instantly examined, this can eliminate potential environmental variations that can contribute to experimental errors. Depending on its optical accessibility, we may evaluate more electroluminochromic materials on this platform.

Lastly, in Chapter 5, we demonstrated a controllable process for artificial biofilm formation using electrobiofabrication. This work can be expanded through: (i) entrapping engineered cells that provide specific functions. For example, cells respond to superoxide or peroxide and promote auto inducers production. Quorum sensing (QS) can be used as an effective pathway for signaling transmission between cells. Via depositing two or multiple artificial biofilms containing different cells and probably tuning the boundaries, we may be able to provide more fundamental understanding about cellular signaling. Functional cells can also serve as “live sensors” that convert environmental information into processible redox and digital signatures.

Overall, we believe that our efforts focused on developing simple and practical interfaces may serve as a humble foundation for future endeavors on physiological, biochemical, and biomedical applications.

Bibliography

1. Kodama, H. Automatic method for fabricating a three-dimensional plastic model with photo-hardening polymer. *Review of Scientific Instruments* **52**, 1770 (1998).
2. Martinez, D. W., Espino, M., Cascolan, H. M., Crisostomo, J. L. & Dizon, J. R. A Comprehensive Review on the Application of 3D Printing in the Aerospace Industry. *Key Eng Mater* **913**, 27–34 (2022).
3. Srinivasan, D. *et al.* 3D Printing Manufacturing Techniques, Materials, and Applications: An Overview. *Advances in Materials Science and Engineering* **2021**, (2021).
4. Buswell, R. A., Leal de Silva, W. R., Jones, S. Z. & Dirrenberger, J. 3D printing using concrete extrusion: A roadmap for research. *Cem Concr Res* **112**, 37–49 (2018).
5. Piyush, Kumar, R. & Kumar, R. 3D printing of food materials: A state of art review and future applications. *Mater Today Proc* **33**, 1463–1467 (2020).
6. Kaye, R., Goldstein, T., Zeltsman, D., Grande, D. A. & Smith, L. P. Three dimensional printing: A review on the utility within medicine and otolaryngology. *Int J Pediatr Otorhinolaryngol* **89**, 145–148 (2016).
7. Bose, S., Vahabzadeh, S. & Bandyopadhyay, A. Bone tissue engineering using 3D printing. *Materials Today* **16**, 496–504 (2013).
8. Do, A. V., Khorsand, B., Geary, S. M. & Salem, A. K. 3D Printing of Scaffolds for Tissue Regeneration Applications. *Adv Healthc Mater* **4**, 1742–1762 (2015).
9. Gopinathan, J. & Noh, I. Recent trends in bioinks for 3D printing. *Biomaterials Research 2018 22:1* **22**, 1–15 (2018).
10. Sochol, R. D. *et al.* 3D printed microfluidics and microelectronics. *Microelectron Eng* **189**, 52–68 (2018).
11. Apparatus and method for creating three-dimensional objects. (1989).
12. Yi, H. G., Lee, H. & Cho, D. W. 3D Printing of Organs-On-Chips. *Bioengineering 2017, Vol. 4, Page 10* **4**, 10 (2017).
13. Jin, Z. *et al.* 3D Printing of Physical Organ Models: Recent Developments and Challenges. *Advanced Science* **8**, 2101394 (2021).
14. Wang, X. Advanced Polymers for Three-Dimensional (3D) Organ Bioprinting. *Micromachines 2019, Vol. 10, Page 814* **10**, 814 (2019).
15. Melchels, F. P. W., Feijen, J. & Grijpma, D. W. A review on stereolithography and its applications in biomedical engineering. *Biomaterials* **31**, 6121–6130 (2010).

16. Ho, C. M. B., Ng, S. H., Li, K. H. H. & Yoon, Y. J. 3D printed microfluidics for biological applications. *Lab Chip* **15**, 3627–3637 (2015).
17. Selimis, A., Mironov, V. & Farsari, M. Direct laser writing: Principles and materials for scaffold 3D printing. *Microelectron Eng* **132**, 83–89 (2015).
18. Raimondi, M. T. *et al.* Two-photon laser polymerization: From fundamentals to biomedical application in tissue engineering and regenerative medicine. *J Appl Biomater Funct Mater* **10**, 56–66 (2012).
19. Photonic Professional GT2: World's highest resolution 3D printer. https://www.nanoscribe.com/en/products/photonic-professional-gt2/#tab-17297.
20. 3D Printer For Microfluidics Applications - Cadworks3D. https://cadworks3d.com/m-series/.
21. Shuler, M. L. Organ-, body- and disease-on-a-chip systems. *Lab Chip* **17**, 2345–2346 (2017).
22. Sin, A. *et al.* The Design and Fabrication of Three-Chamber Microscale Cell Culture Analog Devices with Integrated Dissolved Oxygen Sensors. *Biotechnol Prog* **20**, 338–345 (2004).
23. Sung, J. H., Kam, C. & Shuler, M. L. A microfluidic device for a pharmacokinetic–pharmacodynamic (PK – PD) model on a chip. *Lab Chip* **10**, 446–455 (2010).
24. Baker, M. A living system on a chip. *Nature 2011 471:7340* **471**, 661–665 (2011).
25. Huh, D. *et al.* Reconstituting organ-level lung functions on a chip. *Science (1979)* **328**, 1662–1668 (2010).
26. Cheng, Y., Luo, X., Payne, G. F. & Rubloff, G. W. Biofabrication: programmable assembly of polysaccharide hydrogels in microfluidics as biocompatible scaffolds. *J Mater Chem* **22**, 7659–7666 (2012).
27. Zhao, Z. *et al.* Orthogonal redox and optical stimuli can induce independent responses for catechol-chitosan films. *Mater Chem Front* **6**, 1253–1260 (2022).
28. Kim, E. *et al.* Chitosan to Connect Biology to Electronics: Fabricating the Bio-Device Interface and Communicating Across This Interface. *Polymers (Basel)* **7**, 1–46 (2014).
29. Shang, W., Chen, C.-Y., Lo, K., Payne, G. F. & Bentley, W. E. Chip modularity enables molecular information access from organ-on-chip devices with quality control. *Sens Actuators B Chem* **295**, (2019).
30. Wu, S. *et al.* Catechol-Based Capacitor for Redox-Linked Bioelectronics. *ACS Appl Electron Mater* **1**, 1337–1347 (2019).

31. Wu, S. *et al.* Catechol-Based Molecular Memory Film for Redox Linked Bioelectronics. *Adv Electron Mater* **6**, 2000452 (2020).
32. Shi, X. W. *et al.* Electroaddressing of Cell Populations by Co-Deposition with Calcium Alginate Hydrogels. *Adv Funct Mater* **19**, 2074–2080 (2009).
33. Prendergast, M. E., Solorzano, R. D. & Cabrera, D. Bioinks for biofabrication: current state and future perspectives. *http://dx.doi.org/10.2217/3dp-2016-0002* **1**, 49–62 (2016).
34. Wu, H. C. *et al.* Conferring biological activity to native spider silk: A biofunctionalized protein-based microfiber. *Biotechnol Bioeng* **114**, 83–95 (2017).
35. Li, J. *et al.* Interactive Materials for Bidirectional Redox-Based Communication. *Advanced Materials* **33**, 2007758 (2021).
36. Li, J. *et al.* Mediated Electrochemistry to Mimic Biology's Oxidative Assembly of Functional Matrices. *Adv Funct Mater* **30**, 2001776 (2020).
37. Moroni, L. *et al.* Biofabrication strategies for 3D in vitro models and regenerative medicine. *Nature Reviews Materials 2018 3:5* **3**, 21–37 (2018).
38. Zhao, Z. *et al.* Mediated Electrochemical Probing: A Systems-Level Tool for Redox Biology. *ACS Chem Biol* **16**, 1099–1110 (2021).
39. Zhao, Z. *et al.* System-Level Network Analysis of a Catechol Component for Redox Bioelectronics. *ACS Appl Electron Mater* (2022) doi:10.1021/ACSAELM.2C00269/ASSET/IMAGES/LARGE/EL2C00269_0008.JPEG.
40. Li, J. *et al.* Network-based redox communication between abiotic interactive materials. *iScience* **25**, (2022).
41. Liu, Y., Kim, E., White, I. M., Bentley, W. E. & Payne, G. F. Information processing through a bio-based redox capacitor: Signatures for redox-cycling. *Bioelectrochemistry* **98**, 94–102 (2014).
42. Motabar, D. *et al.* Simple, rapidly electroassembled thiolated PEG-based sensor interfaces enable rapid interrogation of antibody titer and glycosylation. *Biotechnol Bioeng* **118**, 2744–2758 (2021).
43. Ochoa-Repáraz, J. & Kasper, L. H. The Second Brain: Is the Gut Microbiota a Link Between Obesity and Central Nervous System Disorders? *Curr Obes Rep* **5**, 51–64 (2016).
44. Wang, Y. I., Abaci, H. E. & Shuler, M. L. Microfluidic blood–brain barrier model provides in vivo-like barrier properties for drug permeability screening. *Biotechnol Bioeng* **114**, 184–194 (2017).
45. Miller, P. G., Chen, C., Wang, Y. I., Gao, E. & Shuler, M. L. Multiorgan microfluidic platform with breathable lung chamber for inhalation or

intravenous drug screening and development. *Biotechnol Bioeng* **117**, 486–497 (2020).

46. Bober, J. R., Beisel, C. L. & Nair, N. U. Synthetic Biology Approaches to Engineer Probiotics and Members of the Human Microbiota for Biomedical Applications. *Annu Rev Biomed Eng* **20**, 277–300 (2018).
47. Lim, Y. Y., Lee, Y. S. & Ooi, D. S. Q. Engineering the Gut Microbiome for Treatment of Obesity: A Review of Current Understanding and Progress. *Biotechnol J* **15**, 2000013 (2020).
48. Stephens, K. & Bentley, W. E. Synthetic Biology for Manipulating Quorum Sensing in Microbial Consortia. *Trends in Microbiology* vol. 28 633–643 Preprint at https://doi.org/10.1016/j.tim.2020.03.009 (2020).
49. Wang, S., Payne, G. F. & Bentley, W. E. Quorum Sensing Communication: Molecularly Connecting Cells, Their Neighbors, and Even Devices. *Annu Rev Chem Biomol Eng* **11**, 447–468 (2020).
50. Hwang, I. Y. *et al.* Engineered probiotic Escherichia coli can eliminate and prevent Pseudomonas aeruginosa gut infection in animal models. *Nat Commun* **8**, 1–11 (2017).
51. Kim, H. J. & Ingber, D. E. Gut-on-a-Chip microenvironment induces human intestinal cells to undergo villus differentiation. *Integrative Biology* **5**, 1130 (2013).
52. van der Helm, M. W. *et al.* Non-invasive sensing of transepithelial barrier function and tissue differentiation in organs-on-chips using impedance spectroscopy. *Lab Chip* **19**, 452–463 (2019).
53. Costello, C. M. *et al.* Microscale Bioreactors for in situ characterization of GI epithelial cell physiology. *Sci Rep* **7**, 1–10 (2017).
54. Costello, C. M. *et al.* 3-D Intestinal Scaffolds for Evaluating the Therapeutic Potential of Probiotics. *Mol Pharm* **11**, 2030–2039 (2014).
55. Daniel, H., Fett, C. & Kratz, A. Demonstration and modification of intervillous pH profiles in rat small intestine in vitro. *Am J Physiol Gastrointest Liver Physiol* **257**, (1989).
56. Donaldson, G. P., Lee, S. M. & Mazmanian, S. K. Gut biogeography of the bacterial microbiota. *Nature Reviews Microbiology* vol. 14 20–32 Preprint at https://doi.org/10.1038/nrmicro3552 (2015).
57. Campbell, E. L. & Colgan, S. P. Control and dysregulation of redox signalling in the gastrointestinal tract. *Nature Reviews Gastroenterology and Hepatology* vol. 16 106–120 Preprint at https://doi.org/10.1038/s41575-018-0079-5 (2019).

58. Thwaites, D. T., Basterfield, L., McCleave, P. M. J., Carter, S. M. & Simmons, N. L. Gamma-aminobutyric acid (GABA) transport across human intestinal epithelial (Caco-2) cell monolayers. *Br J Pharmacol* **129**, 457–464 (2000).
59. Nielsen, C. U., Carstensen, M. & Brodin, B. Carrier-mediated γ-aminobutyric acid transport across the basolateral membrane of human intestinal Caco-2 cell monolayers. *European Journal of Pharmaceutics and Biopharmaceutics* **81**, 458–462 (2012).
60. Bellmann, S. *et al.* Mammalian gastrointestinal tract parameters modulating the integrity, surface properties, and absorption of food-relevant nanomaterials. *Wiley Interdiscip Rev Nanomed Nanobiotechnol* **7**, 609–622 (2015).
61. Costello, C. M. *et al.* Synthetic small intestinal scaffolds for improved studies of intestinal differentiation. *Biotechnol Bioeng* **111**, 1222–1232 (2014).
62. Sung, J. H., Yu, J., Luo, D., Shuler, M. L. & March, J. C. Microscale 3-D hydrogel scaffold for biomimetic gastrointestinal (GI) tract model. *Lab Chip* **11**, 389–392 (2011).
63. Lamont, A. C., Alsharhan, A. T. & Sochol, R. D. Geometric Determinants of In-Situ Direct Laser Writing. *Sci Rep* **9**, 1–12 (2019).
64. Alsharhan, A. T., Acevedo, R., Warren, R. & Sochol, R. D. 3D microfluidics: Via cyclic olefin polymer-based in situ direct laser writing. *Lab Chip* **19**, 2799–2810 (2019).
65. Ramiah Rajasekaran, P. *et al.* 3D-Printed electrochemical sensor-integrated transwell systems. *Microsyst Nanoeng* **6**, (2020).
66. Kim, H. J., Huh, D., Hamilton, G. & Ingber, D. E. Human gut-on-a-chip inhabited by microbial flora that experiences intestinal peristalsis-like motions and flow. *Lab Chip* **12**, 2165 (2012).
67. Agrawal, C. M. & Ray, R. B. Biodegradable polymeric scaffolds for musculoskeletal tissue engineering. *J Biomed Mater Res* **55**, 141–150 (2001).
68. Gentile, P., Chiono, V., Carmagnola, I. & Hatton, P. An Overview of Poly(lactic-co-glycolic) Acid (PLGA)-Based Biomaterials for Bone Tissue Engineering. *Int J Mol Sci* **15**, 3640–3659 (2014).
69. Ladd, M. R. *et al.* Development of Intestinal Scaffolds that Mimic Native Mammalian Intestinal Tissue. *Tissue Eng Part A* **25**, 1225–1241 (2019).
70. Hinderliter, P. M. *et al.* ISDD: A computational model of particle sedimentation, diffusion and target cell dosimetry for in vitro toxicity studies. *Part Fibre Toxicol* **7**, 36 (2010).
71. Artursson, P. & Karlsson, J. Correlation between oral drug absorption in humans and apparent drug permeability coefficients in human intestinal epithelial (Caco-2) cells. *Biochem Biophys Res Commun* **175**, 880–885 (1991).

72. Nelson, A. L., Dhimolea, E. & Reichert, J. M. Development trends for human monoclonal antibody therapeutics. *Nature Reviews Drug Discovery 2010 9:10* **9**, 767–774 (2010).
73. Kaplon, H., Muralidharan, M., Schneider, Z. & Reichert, J. M. Antibodies to watch in 2020. *https://doi.org/10.1080/19420862.2019.1703531* **12**, (2019).
74. Ecker, D. M., Jones, S. D. & Levine, H. L. The therapeutic monoclonal antibody market. *https://doi-org.proxy-um.researchport.umd.edu/10.4161/19420862.2015.989042* **7**, 9–14 (2015).
75. Rodrigues, M. E., Costa, A. R., Henriques, M., Azeredo, J. & Oliveira, R. Technological progresses in monoclonal antibody production systems. *Biotechnol Prog* **26**, 332–351 (2010).
76. Shukla, A. A., Wolfe, L. S., Mostafa, S. S. & Norman, C. Evolving trends in mAb production processes. *Bioeng Transl Med* **2**, 58–69 (2017).
77. Steinmeyer, D. E. & McCormick, E. L. The art of antibody process development. *Drug Discov Today* **13**, 613–618 (2008).
78. Mullard, A. New drugs cost US$2.6 billion to develop. *Nat Rev Drug Discov* **13**, 877–877 (2014).
79. Langer, E. & Rader, R. Biopharmaceutical Manufacturing: Historical and Future Trends in Titers, Yields, and Efficiency in Commercial-Scale Bioprocessing. *BioProcessing Journal* **13**, 47–54 (2015).
80. Szmacinski, H. *et al.* A novel method for monitoring monoclonal antibody production during cell culture. *Biotechnol Bioeng* **100**, 448–457 (2008).
81. Majewska, N. I., Tejada, M. L., Betenbaugh, M. J. & Agarwal, N. N-Glycosylation of IgG and IgG-Like Recombinant Therapeutic Proteins: Why Is It Important and How Can We Control It? *https://doi-org.proxy-um.researchport.umd.edu/10.1146/annurev-chembioeng-102419-010001* **11**, 311–338 (2020).
82. Wang, Q., Chung, C. Y., Chough, S. & Betenbaugh, M. J. Antibody glycoengineering strategies in mammalian cells. *Biotechnol Bioeng* **115**, 1378–1393 (2018).
83. Liu, L. Antibody Glycosylation and Its Impact on the Pharmacokinetics and Pharmacodynamics of Monoclonal Antibodies and Fc-Fusion Proteins. *J Pharm Sci* **104**, 1866–1884 (2015).
84. Jefferis, R. Glycosylation as a strategy to improve antibody-based therapeutics. *Nature Reviews Drug Discovery 2009 8:3* **8**, 226–234 (2009).
85. Bunkenborg, J., Pilch, B. J., Podtelejnikov, A. V. & Wiśniewski, J. R. Screening for N-glycosylated proteins by liquid chromatography mass spectrometry. *Proteomics* **4**, 454–465 (2004).

86. Mahan, A. E. *et al.* A method for high-throughput, sensitive analysis of IgG Fc and Fab glycosylation by capillary electrophoresis. *J Immunol Methods* **417**, 34–44 (2015).
87. Chiadò, A. *et al.* A modular 3D printed lab-on-a-chip for early cancer detection. *Lab Chip* **20**, 665–674 (2020).
88. Shallan, A. I., Smejkal, P., Corban, M., Guijt, R. M. & Breadmore, M. C. Cost-effective three-dimensional printing of visibly transparent microchips within minutes. *Anal Chem* **86**, 3124–3130 (2014).
89. Chen, Q. *et al.* Combining 3D Printing and Microfluidic Techniques: A Powerful Synergy for Nanomedicine. *Pharmaceuticals 2023, Vol. 16, Page 69* **16**, 69 (2023).
90. Nguyen, K. T. T. *et al.* Formulation of a 3D Printed Biopharmaceutical: The Development of an Alkaline Phosphatase Containing Tablet with Ileo-Colonic Release Profile to Treat Ulcerative Colitis. *Pharmaceutics 2022, Vol. 14, Page 2179* **14**, 2179 (2022).
91. Uddin, M. J. *et al.* 3D printed microneedles for anticancer therapy of skin tumours. *Materials Science and Engineering: C* **107**, 110248 (2020).
92. Chames, P., Van Regenmortel, M., Weiss, E. & Baty, D. Therapeutic antibodies: successes, limitations and hopes for the future. *Br J Pharmacol* **157**, 220–233 (2009).
93. Lund, L. N. *et al.* Exploring variation in binding of Protein A and Protein G to immunoglobulin type G by isothermal titration calorimetry. *Journal of Molecular Recognition* **24**, 945–952 (2011).
94. Itakura, Y. *et al.* Systematic Comparison of Oligosaccharide Specificity of Ricinus communis Agglutinin I and Erythrina Lectins: a Search by Frontal Affinity Chromatography. *The Journal of Biochemistry* **142**, 459–469 (2007).
95. Wu, A. M. *et al.* Recognition factors of Ricinus communis agglutinin 1 (RCA1). *Mol Immunol* **43**, 1700–1715 (2006).
96. Wang, S. *et al.* A Redox-Based Autoinduction Strategy to Facilitate Expression of 5xCys-Tagged Proteins for Electrobiofabrication. *Front Microbiol* **12**, 1473 (2021).
97. Latour, R. A. The langmuir isotherm: A commonly applied but misleading approach for the analysis of protein adsorption behavior. *J Biomed Mater Res A* **103**, 949–958 (2015).
98. Poole, L. B. The basics of thiols and cysteines in redox biology and chemistry. *Free Radic Biol Med* **80**, 148–157 (2015).
99. Paulsen, C. E. & Carroll, K. S. Cysteine-mediated redox signaling: Chemistry, biology, and tools for discovery. *Chem Rev* **113**, 4633–4679 (2013).

100. Corrente, G. A., Beneduci, A., Corrente, G. A. & Beneduci, A. Overview on the Recent Progress on Electrofluorochromic Materials and Devices: A Critical Synopsis. *Adv Opt Mater* **8**, 2000887 (2020).
101. Al-Kutubi, H., Zafarani, H. R., Rassaei, L. & Mathwig, K. Electrofluorochromic systems: Molecules and materials exhibiting redox-switchable fluorescence. *Eur Polym J* **83**, 478–498 (2016).
102. Rauh, R. D. Electrochromic windows: an overview. *Electrochim Acta* **44**, 3165–3176 (1999).
103. Cai, G., Wang, J. & Lee, P. S. Next-Generation Multifunctional Electrochromic Devices. *Acc Chem Res* **49**, 1469–1476 (2016).
104. Li, Y., Young, D. J. & Loh, X. J. Fluorescent gels: a review of synthesis, properties, applications and challenges. *Mater Chem Front* **3**, 1489–1502 (2019).
105. Yen, H. J. & Liou, G. S. Design and preparation of triphenylamine-based polymeric materials towards emergent optoelectronic applications. *Prog Polym Sci* **89**, 250–287 (2019).
106. de Souza, J. C. P. *et al.* In Situ and Operando Techniques for Investigating Electron Transfer in Biological Systems. *ChemElectroChem* **8**, 431–446 (2021).
107. Wu, R., Matta, M., Paulsen, B. D. & Rivnay, J. Operando Characterization of Organic Mixed Ionic/Electronic Conducting Materials. *Chem Rev* **122**, 4493–4551 (2022).
108. Silah, H., Erkmen, C., Demir, E. & Uslu, B. Modified indium tin oxide electrodes: Electrochemical applications in pharmaceutical, biological, environmental and food analysis. *TrAC Trends in Analytical Chemistry* **141**, 116289 (2021).
109. Aydın, E. B. & Sezgintürk, M. K. Indium tin oxide (ITO): A promising material in biosensing technology. *TrAC Trends in Analytical Chemistry* **97**, 309–315 (2017).
110. Akanda, Md. R., Osman, A. M., Nazal, M. K. & Aziz, Md. A. Review—Recent Advancements in the Utilization of Indium Tin Oxide (ITO) in Electroanalysis without Surface Modification. *J Electrochem Soc* **167**, 037534 (2020).
111. Zhao, Z., Kim, E., Motabar, D., Bentley, W. E. & Payne, G. F. Spectroelectrochemical Network Measurements for Redox Bioelectronics. *Chemistry of Materials* (2022) doi:10.1021/ACS.CHEMMATER.2C02707/ASSET/IMAGES/LARGE/CM2C02707_0007.JPEG.

112. Xu, X. *et al.* The New Era of High-Throughput Nanoelectrochemistry. *Anal Chem* **95**, 319–356 (2023).
113. Shachar, S., Voss, T. C., Pegoraro, G., Sciascia, N. & Misteli, T. Identification of Gene Positioning Factors Using High-Throughput Imaging Mapping. *Cell* **162**, 911–923 (2015).
114. Griffith, J. E. *et al.* Quantitative high-throughput measurement of bulk mechanical properties using commonly available equipment. *Mater Horiz* **10**, 97–106 (2023).
115. VanArsdale, E. *et al.* Electrogenetic Signal Transmission and Propagation in Coculture to Guide Production of a Small Molecule, Tyrosine. *ACS Synth Biol* **11**, 877–887 (2022).
116. Christer Ericson, †, Johan Holm, ‡, Thomas Ericson, ‡ and & Stellan Hjertén*, †. Electroosmosis- and Pressure-Driven Chromatography in Chips Using Continuous Beds. (1999) doi:10.1021/AC990802G.
117. Mansouri, M. & Fussenegger, M. Electrogenetics: Bridging synthetic biology and electronics to remotely control the behavior of mammalian designer cells. *Curr Opin Chem Biol* **68**, 102151 (2022).
118. Tschirhart, T. *et al.* Electronic control of gene expression and cell behaviour in Escherichia coli through redox signalling. *Nature Communications 2017 8:1* **8**, 1–11 (2017).
119. Terrell, J. L. *et al.* Bioelectronic control of a microbial community using surface-assembled electrogenetic cells to route signals. *Nature Nanotechnology 2021 16:6* **16**, 688–697 (2021).
120. Frasconi, M., Mazzei, F. & Ferri, T. Protein immobilization at gold–thiol surfaces and potential for biosensing. *Analytical and Bioanalytical Chemistry 2010 398:4* **398**, 1545–1564 (2010).
121. Lazanas, A. C. & Prodromidis, M. I. Electrochemical Impedance Spectroscopy─A Tutorial. *ACS Measurement Science Au* (2022) doi:10.1021/ACSMEASURESCIAU.2C00070/ASSET/IMAGES/LARGE/TG2C00070_0032.JPEG.
122. Motabar, D., Li, J., Payne, G. F. & Bentley, W. E. Mediated electrochemistry for redox-based biological targeting: entangling sensing and actuation for maximizing information transfer. *Curr Opin Biotechnol* **71**, 137–144 (2021).
123. Liu, Y. *et al.* Connecting Biology to Electronics: Molecular Communication via Redox Modality. *Adv Healthc Mater* **6**, 1700789 (2017).
124. Kizek, R., Vacek, J., Trnková, L. & Jelen, F. Cyclic voltammetric study of the redox system of glutathione using the disulfide bond reductant tris(2-carboxyethyl)phosphine. *Bioelectrochemistry* **63**, 19–24 (2004).

125. D'souza, A. A. & Shegokar, R. Polyethylene glycol (PEG): a versatile polymer for pharmaceutical applications. *http://dx.doi.org.proxy-um.researchport.umd.edu/10.1080/17425247.2016.1182485* **13**, 1257–1275 (2016).
126. Hutmacher, D. W., Sittinger, M. & Risbud, M. V. Scaffold-based tissue engineering: rationale for computer-aided design and solid free-form fabrication systems. *Trends Biotechnol* **22**, 354–362 (2004).
127. Chen, J., Spear, S. K., Huddleston, J. G. & Rogers, R. D. Polyethylene glycol and solutions of polyethylene glycol as green reaction media. *Green Chemistry* **7**, 64–82 (2005).
128. Murray, C. J. *et al.* Global burden of bacterial antimicrobial resistance in 2019: a systematic analysis. *The Lancet* **399**, 629–655 (2022).
129. Birk, S. E., Boisen, A. & Nielsen, L. H. Polymeric nano- and microparticulate drug delivery systems for treatment of biofilms. *Adv Drug Deliv Rev* **174**, 30–52 (2021).
130. Cos, P., Tote, K., Horemans, T. & Maes, L. Biofilms: An Extra Hurdle for Effective Antimicrobial Therapy. *Curr Pharm Des* **16**, 2279–2295 (2010).
131. Percival, S. L. *et al.* Surfactants: Role in biofilm management and cellular behaviour. *Int Wound J* **16**, 753–760 (2019).
132. Little, B. & Ray, R. A Perspective on Corrosion Inhibition by Biofilms. *Corrosion* **58**, 424–428 (2002).
133. Orazi, G. & O'Toole, G. A. 'It takes a village': Mechanisms underlying antimicrobial recalcitrance of polymicrobial biofilms. *J Bacteriol* **202**, (2020).
134. Rijavec, T. *et al.* Natural Microbial Communities Can Be Manipulated by Artificially Constructed Biofilms. *Advanced Science* **6**, 1901408 (2019).
135. Dunne, W. M. Bacterial adhesion: Seen any good biofilms lately? *Clin Microbiol Rev* **15**, 155–166 (2002).
136. Stewart, E. J., Ganesan, M., Younger, J. G. & Solomon, M. J. Artificial biofilms establish the role of matrix interactions in staphylococcal biofilm assembly and disassembly. *Scientific Reports 2015 5:1* **5**, 1–14 (2015).
137. Reinhardt, T., Moelzner, J., Neu, T. R. & Fink, P. Biofilm pads—an easy method to manufacture artificial biofilms embedded in an alginate polymer matrix. *Limnol Oceanogr Methods* **18**, 1–7 (2020).
138. Vajravel, S., Sirin, S., Kosourov, S. & Allahverdiyeva, Y. Towards sustainable ethylene production with cyanobacterial artificial biofilms. *Green Chemistry* **22**, 6404–6414 (2020).

139. Qi, X. *et al.* Artificial electrochemically active biofilm for improved sensing performance and quickly devising of water quality early warning biosensors. *Water Res* **198**, 117164 (2021).
140. Song, Y. E. *et al.* Biofilm matrix and artificial mediator for efficient electron transport in CO2 microbial electrosynthesis. *Chemical Engineering Journal* **427**, 131885 (2022).
141. Koley, D. Electrochemical sensors for oral biofilm–biomaterials interface characterization: A review. *Mol Oral Microbiol* **37**, 292–298 (2022).
142. Li, J. *et al.* Electrobiofabrication: electrically-based fabrication with biologically-derived materials. *Biofabrication* **11**, 032002 (2019).
143. Azizipour, N., Avazpour, R., Rosenzweig, D. H., Sawan, M. & Ajji, A. Evolution of Biochip Technology: A Review from Lab-on-a-Chip to Organ-on-a-Chip. *Micromachines 2020, Vol. 11, Page 599* **11**, 599 (2020).
144. Antfolk, M. & Jensen, K. B. A bioengineering perspective on modelling the intestinal epithelial physiology in vitro. *Nature Communications 2020 11:1* **11**, 1–11 (2020).
145. Kwon, T. *et al.* Microfluidic Cell Retention Device for Perfusion of Mammalian Suspension Culture. *Scientific Reports 2017 7:1* **7**, 1–11 (2017).